HETEROATOM ALKYLATION REACTIONS OF AROMATIC COMPOUNDS OVER METAL OXIDES

A THESIS SUBMITTED TO THE
UNIVERSITY OF PUNE
FOR THE DEGREE OF
DOCTOR OF PHILOSOPHY
IN
CHEMISTRY

BY

M. VIJAYARAJ

CATALYSIS DIVISION
NATIONAL CHEMICAL LABORATORY
PUNE 411 008
INDIA

JUNE 2006

DECLARATION

I hereby declare that the thesis **"Heteroatom alkylation reactions of aromatic compounds over metal oxides"** submitted for the degree of Doctor of Philosophy to the University of Pune has not been submitted by me for a degree to any other University.

M.VIJAYARAJ

CERTIFICATE

This is to certify that the work incorporated in the thesis, **“Heteroatom alkylation reactions of aromatic compounds over metal oxides”** submitted by **Mr. M. Vijayaraj,** for the Degree of **Doctor of Philosophy,** was carried out by the candidate under my supervision in the Catalysis Division, National Chemical Laboratory, Pune – 411 008, India. Such material as has been obtained from other sources has been duly acknowledged in the thesis.

Dr. C. S. Gopinath

(Research Supervisor)

Acknowledgement

I express my deep sense of gratitude to my research supervisor, Dr. C. S. Gopinath for helping me throughout my research career and for his kind attention and meticulous review on the final draft of my thesis.

I would like to thank the present and past heads of the division, Dr. Rajivkumar and Drs. A. V. Ramaswamy and S. Sivasanker, for providing me all the divisional facilities required for my research work.

I also thank Dr. Veda Ramaswamy, for helping me with a furnished lab and GC facilities and thanks are due to all the scientific and non-scientific staffs in the division for their direct and indirect help in various occasions.

Many thanks go to the present and past directors, National Chemical Laboratory, for allowing me to carry out the research work in a prestigious and well-equipped laboratory.

With much appreciation, I would like to admire all of my friends in NCL and outside; for their kind support during my difficult times and it is not just possible to acknowledge all of them in few words for their timely and invaluable help throughout my life.

Special thanks to all my family members for supporting me continuously and it really helped me to pursue my life as a research fellow.

CSIR, New Delhi is acknowledged for research fellowship.

Vijayaraj.

Contents

Chapter 1: Introduction

Chapter 2: Preparation and characterization of catalysts

Chapter 3: N-methylation of aniline and aniline substrates on $Cu_{1-x}Zn_xFe_2O_4$

Chapter 4: Aniline N-methylation on $Cu_{1-x}Zn_xFe_2O_4$

Chapter 5: Photoemission studies on $Cu_{1-x}Zn_xFe_2O_4$

Chapter 6: O-methylation of DHB on MgO: Selective production of MP

Chapter 7: Mechanism of MgO and promoted MgO catalysts deactivation

Chapter 1: Introduction

1.1 Catalysis

Catalysis is the word used to describe the action of a catalyst, which enhances the rate at which a chemical reaction attains equilibrium. Catalyst can increase the rate of only thermodynamically feasible processes and it cannot initiate reactions, which are not thermodynamically feasible. In other words, an increase in the rate constant of the forward reaction brought by catalyst is accompanied by a corresponding increase in the rate constant of the reverse reaction or simply catalyst facilitates the approach to equilibrium of a chemical reaction [1].

Presently, more than 90% of the industrial chemical processes in use throughout the world are catalyst aided and the research interest on catalyst and/or catalysis is increasing continuously. Catalysis is classified into homogeneous and heterogeneous catalysis. Catalytic processes that take place in a uniform gas or liquid phase are classified as homogenous catalysis. Generally, homogenous catalysts are well-defined compounds or coordination complexes, which are molecularly dispersed with the reactants in the reaction medium. Heterogeneous catalysis takes place between several different phases, normally, catalyst is a solid and the reactants are gases or liquids.

1.2 Heterogeneous catalysis

Heterogeneous catalysis is gaining increasing importance in the production of fine chemicals and pharmaceuticals due to its definite technical advantages, like production process, competitiveness, and economy. The main advantage of a heterogeneous catalyst is that it can be operated in a fixed bed reactor by which reactants flow continuously without interruption, since the catalyst is present in a phase different from that of the reactants as well as products and it can be separated very easily from the reaction mass.

The successful exploitation of a material as a catalyst gives value added products with better yields. heterogeneous catalysis can be employed to various reactions and for the present thesis work catalytic heteroatom alkylation of aromatic compounds on metal oxides is dealt with detail.

1.3 Alkylation of aromatic compounds

The alkylation of aromatic compounds is widely used in the large-scale synthesis of fine chemicals and valuable synthetic intermediates [2]. The reaction is essentially replacing a hydrogen atom of an aromatic compound by an alkyl group derived from an alkylating agent. The substitution for hydrogen by an alkyl group can be on the aromatic ring and/or on the side chain of aromatic compounds or on the heteroatom present in the aromatic compounds like anilines, phenols, etc. Nevertheless, various experimental factors decide the center for substitution of hydrogen by alkyl group. Thus the nature of the alkylated product formed depends on the catalysts employed and the reaction conditions applied. However, the former influences the products formation to a larger extent than the latter. In general, acidic catalyst favors aromatic ring alkylation whereas basic catalyst favors side chain or heteroatom alkylation [3]. An overwhelming majority of alkylation reactions are acid catalyzed. The base-catalyzed alkylation of aromatic compounds has received much less attention than that catalyzed by acids.

1.4 Heteroatom alkylation of aromatic compounds

Heteroatom alkylation of aromatic compounds is equally an important reaction in the class of alkylation reactions. Indeed, O-alkylated products of phenols and N-alkylated products of anilines are used as starting materials in the production of fine chemicals, agrochemicals, pharmaceuticals, dyes, antioxidants, plastics and herbicides [4,5]. Demand for heteroatom alkylation has increased since the selective alkylation at heteroatom center is difficult because of the competing ring alkylation. For instance, Kapsi *et al.* [6] studied the methylation of phenol and the rearrangement of anisole over Nafion-H and concluded that O-methylation forming anisole is followed by intermolecular O→C methyl transfer leading to formation of cresols. In the case of aniline, N-methylation on ZSM-5 [7], the product consisted of both C-alkylates (toluidines) and N-alkylates (N-methylaniline and N, N-dimethylaniline). Hence it is necessarily important to control the selectivity of heteroatom alkylated products over C-alkylated products. As mentioned before, the products selectivity depends mainly on the catalysts employed and the reaction parameters.

1.4.1 N-methylation of aniline

Aniline N-methylation always yields poor product selectivity due to the presence of chemically equivalent protons attached to the nitrogen atom. The high nucleophilicity of the amine nitrogen results in the formation of mixture of N-methyl and N, N-dimethylated products [8]. Ko *et al.* [9] reported the methylation of aniline with methanol at 698 K over alumina and formed both N-methylaniline (NMA) and N,N-dimethylaniline (DMA) and the corresponding activation energies are 62.7±2.1 and 48.3±2.9 $\mathrm{KJmol^{-1}}$, respectively. It is obvious that NMA reacts faster than aniline and undergoes consecutive methylation to DMA that leads to poor product selectivity or highly selective DMA formation. Hence it is difficult to synthesize N-methylaniline (NMA) selectively over N, N-dimethylaniline (DMA). However, by varying the reaction parameters it is possible to control the formation of DMA. N-methylaniline is a useful synthetic intermediate for the synthesis of several organic molecules [2,5].

1.4.2 O-methylation of dihydroxybenzenes

O-methylation of dihydroxybenzenes (catechol, resorcinol and hydroquinone) is also an important reaction. Selective O-methylation of one of the -OH groups in catechol gives guaiacol (2-methoxyphenol), which is an intermediate for vanillin synthesis. 3-methoxyphenol and 4-methoxyphenol derived from the selective methylation of resorcinol and hydroquinone, respectively, are also useful as synthetic intermediates and UV inhibitors [4]. Selective production of methoxyphenols cannot be easily achieved since the formation of dimethoxybenzenes is always encountered in the process. This is because of the greater reactivity of methoxyphenols than the dihydroxybenzenes, which is due to the differences in the mesomeric effects of $-OCH_3$ and $-OH$ groups [8].

1.5 Catalyst systems

Anhydrous metal halides, also known as Friedel-Craft's catalysts have been used extensively for alkylation of aromatic compounds. Since they are very active the reaction can be carried out at low temperature in homogeneous liquid phase [10]. Many reactions are carried out in batch processes using $AlCl_{3,}$ as a soluble catalyst, which is inexpensive and very reactive. Although these homogeneous catalysts are efficient, their corrosive and toxic nature leads to potential environmental hazards and associated operational problems, including downstream processes such as difficulty in separation, recovery, and reutilization that result in higher capital costs. The use of safe solid catalysts (acidic and basic) in place of these traditional catalysts is being attempted under vapor phase conditions for the last few decades. Several alkylation reactions of aromatic compounds have been examined over oxides, mixed oxides, supported oxides, zeolites and mesoporous materials. These solid catalysts are highly desirable due to its non-polluting reasons such as non-corrosive and offer additional advantages in controlling the product selectivity via acid-base properties in the case of oxides [11] (mixed and supported) and shape selective properties in the case of zeolites [12].

1.5.1 Aniline N- methylation catalysts

Several types of solid catalysts based on oxides and supported oxides [12-17], zeolites [18-25], clays [26, 27] and microporous aluminophospates [28-31] have been tested for aniline methylation. The main factors influencing the activity and the selectivity of N- and/or C-methylation are acid-base properties and shape selectivity by pores in the catalysts and the reaction conditions (temperature, feed composition and feed rate). Rao *et al.* [31] reported the mechanism of aniline methylation with methanol as methylating agent over microporous aluminophospates molecular sieve. They observed that in aniline methylation, NMA formation appears to be favored at low reaction temperature (below 598 K), which is subsequently methylated to DMA and then isomerizes to N-methyltoluidine (NMT). When the temperature was increased above 598 K, isomerization occurs in large extent by the carbocation mechanism, as demonstrated by studying the reaction of DMA. Ono *et al.* [32, 33] reported aniline methylation with methanol and dimethylcarbonate (DMC) as methylating agent over X- and Y- faujasite. They showed that faujasite was a better catalyst than ZSM-5 and Na-mordenite with regard to activity and selectivity. However, 93% NMA selectivity was achieved and the other side product was mainly DMA.

Barthomeuf *et al.* [34, 35] studied the selectivity to mono or dimethylation in the reaction of aniline with DMC on alkaline faujasite, EMT and beta zeolites. They concluded that K-EMT was as selective as KY for the formation of NMA from aniline and DMC. Alkaline X-zeolites favored the formation of DMA over NMA. The experimental conditions like space velocity and reactant ratio were optimized to improve the selectivity of NMA over DMA. Park *et al.* [20] reported the selective methylation of aniline with methanol over metallosilicates. The selectivity for DMA is higher when metallosilicates possess larger amount of medium acid sites. Su *et al.* [22, 23] reported aniline methylation with methanol on faujasite and concluded that methylation of aniline involved the participation of acid-base sites. N-methylated products (NMA and mainly DMA) were produced over basic zeolites (K, Rb and Cs), whereas C-methylated products were formed over relatively less basic cations, Li and Na.

Selva *et al.* [36] reported the monomethylation of primary amines by DMC over X and Y type zeolites; the unusual mono N-methylation selectivity observed was likely to be due to synergistic effects between the double reactivity of DMC (acting both as a methylating and as a reversible methoxy carboxylating agent) and the dual acid-base properties of zeolites along with the steric demand by their cavities. Besides, the high NMA selectivity, the reaction also has remarkable environmentally benign features.

Bautista *et al.* [28-30] reported the N-methylation of aniline with methanol over $CrPO_4$ and $CrPO_4$-$AlPO_4$ catalysts. 90% selectivity for N-methylated products was achieved at temperatures between 573 and 673 K. Varying the feed flow rates indicated that low contact time and low temperature promote the NMA formation. On the other hand, the addition of $AlPO_4$ to $CrPO_4$ did not cause any significant change in the selectivity pattern exhibited by the $CrPO_4$ catalyst. This indicates that similar adsorbed active sites are formed on $CrPO_4$ and $CrPO_4$-$AlPO_4$ catalysts. It has been suggested that NMA and DMA formed by the separate stepwise methylation and follows first order kinetics. The effect of surface acidity on aniline methylation was analyzed by adsorption of pyridine and 2,6-dimethylpyridine on catalysts and concluded that strong acid sites were not required for the N-methylation of aniline, whereas weak to moderate acid sites seem to be responsible for the reaction.

Elangovan *et al.* [37] reported aniline methylation over AFI and AEL type molecular sieves at 623-673 K and formed NMA, DMA and N-methyltoluidines (NMT). The products formation were influenced by reaction temperature, space velocity and feed molar ratio. Sreekumar *et al.* [38-41] studied N-methylation of aniline over ternary ferrospinels ($A_{1-x}A'_xFe_2O_4$; A = Zn and A' = Co, Ni) type catalysts. They compared the role of DMC and methanol as methylating agent and found that methanol was better alkylating agent than DMC over these catalysts.

1.5.2 Dihydroxybenzenes O-methylation catalysts

Several reports have been found for O-methylation of phenol on oxides, sulfates and phosphates [42-47]. It has generally been concluded that the high selectivity for O-methylated product involves the participation of basic sites in the methylation process. Ono *et al*. reported the selective O-methylation of catechol over alumina [48], alkali hydroxide loaded alumina [49] and potassium nitrate loaded alumina [50]. Over alumina, DMC was more efficient methylating agent than methanol in the methylation of catechol. The main product was guaiacol obtained with 70% selectivity. Addition of water to the feed considerably increases the catalytic activity over time on stream (TOS) studies. LiOH loaded alumina was found to be a selective catalyst for the guaiacol formation (84%) with a catechol conversion nearly 100% at 583 K [49]. Over alumina loaded with potassium nitrate a very high catalytic activity with veratrole yield of 97% was obtained at 583 K for feed with DMC to catechol molar ratio of 4 [50]. On Cs loaded alumina [51], catechol methylation yielded guaiacol and catechol carbonate that further reacted with DMC resulted in the veratrole formation.

Cavani *et al.* [52-54] found boron phosphates as efficient catalysts for the O-methylation of catechol aimed at the production of guaiacol. Catalyst having B/P=1, made of BPO_4 displayed best results in terms of catechol conversion, guaiacol selectivity and steady performance with TOS. The optimum surface acidity reduced the undesired tar formation and ring methylation reactions. However, supporting BPO_4 catalyst on alumina resulted in loss of actual activity.

Vishwanathan *et al.* [55] reported the vapor phase methylation of catechol over solid base catalysts, like Cs loaded TiO_2, Al_2O_3 and SiO_2. High selectivity for guaiacol was achieved and CO_2 temperature programmed desorption studies indicated the presence of weak basic sites and their participation in O-methylation process. Rao *et al.* [56, 57] found Mg-Al hydrotalcite as potential catalyst for the synthesis of guaiacol. A maximum guaiacol yield of 80% was obtained at 573 K under optimized reaction conditions. A concerted mechanism involving acid-base pair sites in which nucleophilic attack at the methyl carbon atom of DMC by the phenolic oxygen or phenolate anion was proposed.

Renken *et al.* [58, 59] studied the regulation to control the selectivity in vapor phase methylation of catechol to guaiacol over modified alumina. A 20-fold change in the O/C-methylation ratio was achieved by varying the catalyst acid-base properties. Catalytic activity and selectivity towards guaiacol formation was found to increase with surface acidity. Sivasanker *et al.* [60, 61] reported O-methylation of dihydroxybenzenes on alkali metal ions loaded silica. Activity of the catalysts and selectivity for dimethoxybenzenes increases with metal loading and basicity of the metal ions. The order of reactivity of the three dihydroxybenzenes is catechol< hydroquinone< resorcinol. Assuming the methylation process as pseudo-first-order kinetics, the ratio of rate constants of second methylation to first methylation (K_2/K_1) was found to predict the ratio of dimethoxybenzene to total methoxy products [61].

Very recently Zhu et al. [62] reported guaiacol production from Ti containing aluminium phosphate catalyst. 65 to 100% guaiacol selectivity with nearly 600 h TOS stability of the catalysts was achieved. Fu *et al.* [63] explored $ZnCl_2$ modified alumina catalysts for O-methylation of catechol with methanol. High selectivity for guaiacol (82%) was due to weak coordination of catechol with Zn^{2+} sites. $ZnCl_2$ leaching and surface coking during reaction was the main cause for catalyst deactivation.

1.6 Metal oxides as catalysts

In metal oxides the cations and the anions are surrounded by each other leading to an ordered long range bulk structure, which is largely determined by the stoichiometry. Metal oxides also represent one of the most important and widely employed categories of solid catalysts, either as active phases or supports. They are utilized, both for their acid-base and redox properties and constitute the largest family of catalysts in heterogeneous catalysis. They also exhibit a wide range of activities and selectivities for a variety of chemical reactions, partly due to the rich variety of surface sites and the ability of their surface cations to assume different valence states [64]. Hence, they stand as the seminal solid catalysts for industrially important processes involving hydrogenation/dehydrogenation, oxidation, ammoxidation, polymerization etc [65-68]. They also gained importance as alkylation catalysts due to their acid-base properties. Alumina, silica, transition metal oxides, magnesium oxide and silica–alumina in their various modified forms have been evaluated for alkylation reactions [69-74]. Their use as catalysts still holds promise though catalytic materials like zeolites and mesoporous materials found some selective applications in recent years [75].

1.6.1 Alkali and alkaline earth metal oxides

The catalytic properties of alkali metal oxides (Li_2O, Na_2O, K_2O, Rb_2O, Cs_2O) have not been studied immensely as bulk catalysts. However, many studies have been carried out with alkali metals doped on oxide supports, exchanged with zeolites and intercalated in clays or layered materials [76]. They are recognized as base catalysts due to their catalytic features and they are very active and selective for many reactions like isomerizations, dehydrogenations, aldol condensations, Knoevenagal reactions, additions, alkylations, acylations and cyclizations [77-79]. The reactions catalyzed by them are very interesting, though the state of alkali metal ions on supports are not well understood.

Alkaline earth metal oxides (MgO, CaO, SrO and BaO) are not emerged well as catalytic materials. Presently they are known as very active base catalysts for a few reactions, like, isomerisation of alkenes and aldol condensations [77]. High temperature pretreatment makes them very active materials for such reactions. Owing to their toxicity and radioactivity, usage of BeO and RaO as catalyst is hardly found in the literature. MgO, CaO, SrO and BaO are positioned as solid base catalysts, among them MgO is being employed for many reactions as a single component catalyst or as a part of mixed oxide catalysts or as a support catalyst [79]. In particular, MgO forms a layered hydroxycarbonate known as hydrotalcite ($Mg_6Al_2(OH)_{16}CO_3.4H_2O$) occurring naturally in foliated forms and can be prepared synthetically. This hydrotalcite compounds have found several practical applications and have been used as such or after calcination. High temperature calcination of hydrotalcite gives high surface area oxides having basic properties more than that of pure MgO [80].

1.6.2 Alkali metal ions promoted MgO

The oxides of alkali metals are basic in nature. The oxides of rubidium and cesium have been reported as super bases, possessing base strength with a Hammett basicity function ($H\_$) exceeding +26 [81]. Therefore, it is expected that supported oxides of these alkali metals also exhibit strong basicity. This triggered researchers attention to develop heterogeneous base catalysts for industrial applications [11]. Matsuda *et al.* [82] found that the basicity of MgO increases when doped with alkali metal ions and the enhancement in the basicity was attributed to the perturbation of the charge distribution on MgO. Super basic catalysts have been synthesized by supporting one or more alkali metal elements on MgO and the systems were found very active for oxidative coupling reaction of methane [83]. Further, the same catalysts were found active for oxidative methylation of toluene with methane to give styrene and ethyl benzene in good yield [84].

Several reports were found on alkali metals doped MgO and their activity for transesterification reaction.

1.6.3 Transition metal oxides

Transition metal oxides are used widely for large number of chemical reactions such as oxidation, oxidative/non-oxidative dehydrogenation, reduction, ammoxidation, metathesis (production of long chain alkenes), esterifications and water gas shift reaction. The cations in transition metal oxides often exist in more than one oxidation state that makes them especially active for reactions of the oxidation-reduction class [11]. It was demonstrated that a mixture of metal oxides brings out combined effect or a synergistic behavior, which was well known among the transition metal oxides that enhance the catalytic activity [85, 86] for several reactions.

1.7 Mixed metal oxides

Oxides containing two or more different kinds of metal cations are known as mixed metal oxides. Oxides can be binary, ternary and quaternary and so on with respect to the presence of number of different metal cations. They can be further classified, based on whether they are crystalline or amorphous. If the oxides are crystalline the crystal structure can determine the oxide composition. For instances, perovskites have the general formula ABO_3, scheelites are ABO_4, spinels are AB_2O_4 and palmeirites are $A_3B_2O_8$ [87]. The different metal cations (M_I and M_{II}) are present as M_I^{n+} -O_x and M_{II}^{n+} -O_x polyhedra, which is connected in various possible ways, such as corner or edge sharing, forming chains M_I-O-M_{II}-O, M_I-O-M_I-O or M_{II}-O-M_{II}-O. The arrangement of cation of a given element differs by the coordination and the nature of the neighboring cation and this governs the type of bonding between the cations. Different environment of cation that constitutes an active center would give rise to different reactivity towards an approaching molecule.

It is often not clear, which of the constituent metal cation plays a role of active centers in mixed metal oxides. Although the industrial catalysts are usually multiphase systems, the presence of some particular phase appears to be critical to render the activity of the system for a given reaction. One of the most important results of the monophasic systems study is the demonstration of different catalytic properties of different crystallographic faces in an oxide that provided an experimental proof for structure sensitivity phenomenon in the oxide systems.

1.7.1 Spinels

Among the mixed metal oxides, spinel-type oxides remain prominent not only due to its application in catalysis, but also as magnetic materials in number of device applications. The spinel oxides have the general formula of AB_2O_4 for a simple binary spinel. Interestingly ternary spinel system is also known, which can be represented as $(A'A'')B_2O_4$ or $A(B'B'')O_4$. In the above formula A and B are the divalent tetrahedral (T_d) and trivalent octahedral (O_h) cations, respectively. If A type cations occupy T_d and B types cations occupy O_h sites then it is a normal spinel. If half of the B cations occupy T_d sites and A cations along with other half of B occupy O_h sites then it is called a fully inverse spinel. There are other types of spinels called as random spinels where cations distribution will be in between the normal spinel and fully inverse spinel arrangement. Spinel contains Fe^{3+} in them as B site cation is termed as “ferrospinel”. The unit cell of an ideal spinel contains 8 formula units represented as $8[AB_2O_4]$, which forms a face centered cubic (*fcc)* arrangement with 32 O^{2-} ions, while metal cations occupy interstitial sites. Close packing arrangement of 32 O^{2-} ions form 64 T_d and 32 O_h interstices out of which 8 T_d and 16 O_h sites are occupied by cations [88].

1.8 Spinels as catalysts

Spinels show interesting catalytic properties, in which the properties are controlled by the nature of ions, their charge and site distribution between T_d and O_h sites. Bautiles and Barboax [89] investigated the surface composition of normal spinel oxides using differential neutron diffraction (DND) techniques. This method suggested that the surface of normal spinel consists of mixture of (110) and (111) planes. But, in the case of distorted spinels like γ-alumina, 80% of the exposed faces have the (110) direction. They observed that such planes contain only octahedral cation and oxygen anion. Probing the surface layer of the materials has become more accurate after introducing low energy ion scattering (LEIS) technique in surface science. The most characteristic feature of the LEIS is that the peaks in the spectra result from the scattering by top-most atomic layer. Jacobs et al. [90] applied this technique to evaluate spinel surface composition. Their work revealed that O_h sites are exposed almost exclusively at the surface of the spinel oxide and the catalytic activity of many such systems is mainly due to O_h cations. Several other workers also believed that T_d site ions are either inactive or contributing only a little to the catalytic properties [91]. Another possible reason for the lower activity of T_d cations comes from the fact that, due to lower coordination number, the metal oxygen bonds will be stronger and hence such cations are not easily accessible to the reactants. Nonetheless, results reported by Thomas *et al.* [92,93] shows the dominance of T_d ions on the surface through XPS analysis of $Cu_{1-x}Co_xFe_2O_4$ employed for phenol alkylation.

Catalytic activities of different spinel compounds have been well established for various reactions. Among the spinel compounds ferrospinels have been used as effective catalysts because of the ease with which iron can exchange its oxidation state between 2 and 3. Another important feature attributed with these materials, from the commercial standpoint, is that spinel structure provides high stability so that these materials can withstand reducing conditions to a reasonable extent. Even if reduction of Fe^{3+} to Fe^{2+} occurs, spinel structure remains unaltered and upon reoxidation the original state can be retained [94].

1.9 Preparation of catalysts

Any catalyst should be cost effective, must amplify process efficiency without affecting the existing processes and conditions. A number of fundamental studies concerning the influence of preparation procedures on the catalyst performances have been published [95, 96]. In all the cases, it was stated that the activity and stability of the catalysts were also dependent on the preparation parameters, in particular thermal activation, thereby suggesting that catalyst preparation is a critical factor. The most common methods used to prepare metal oxides are co-precipitation [97, 98], sol-gel method [99, 100], combustion method [101, 102] and ceramic method [103].

1.10 Catalytic properties of metal oxides

In general, cations on the surface possess Lewis acidity, i.e. they behave as electron acceptors. The oxygen ions behave as proton acceptors and are thus Bronsted bases. According to the Bronsted acid concept, an acid is a hydrogen-containing species able to release a proton and a base is any species capable of combining with a proton. Lewis concept is that an acid accepts an electron pair; conversely a base is any species that can donate an electron pair [104]. Thus the surface acid-base properties of metal oxides can influence the substrate and/or reactant adsorption followed by reaction. Metal oxides have unique catalytic properties towards alkylation reactions that are mainly influenced by their acid-base properties. The acid-base properties of the metal oxides can be tuned by choosing the different metal cations and also by varying their compositions. Also from the electronic structure point of view, the mixing of two or more different metal oxides influences the overlap between metals orbital to different extents. The catalytic conversion, desired product selectivity or yield depends upon the above factors.

1.11 Characterization techniques

Understanding how activity and selectivity change with catalyst structural and electronic properties is one of the major goals in catalysis research. Therefore, a number of physicochemical and spectroscopic characterization methods have been used for the past few decades. This enables to derive catalyst structure-activity relationship for any reaction. This knowledge helps to understand the catalyst better, so that catalyst can be improved or designed as required [105]. The most common techniques used in catalyst characterization are XRD, adsorption studies (BET), temperature programmed studies (TPR, TPD and TPO), FT-IR, UV-VIS and Raman spectroscopy. These techniques offer to investigate the nature of an active catalyst.

Heterogeneous catalysis involves interaction between catalyst surface and reactant(s) followed by reaction towards possible product(s). Hence technique, which can provide very detailed idea about the catalyst surface structure, chemical composition and electronic properties of the surfaces are demanded for modern catalyst characterization. AFM, AES, EELS, LEED, LEIS, SIMS, UPS and XPS are the powerful surface characterization techniques. Among them XPS and AES are mostly applied to probe the surface [104] to identify the electronic structure of the catalyst in detail. They yield information on catalyst surface composition, oxidation state and dispersion of the metal present on the surface.

The advances in instrumentation and experimental techniques have made it possible to study the chemistry of the interface between the catalyst and substrates in greater detail than ever before. Especially, *in situ* techniques (under working conditions) for catalyst characterization enable the researcher to achieve quite distinctly the above said objective. Hence a number of *in situ* spectroscopic techniques are being applied that can probe the catalytic reactions in progress as well as the changes on the working catalyst [107-109].

1.12 Objective of the present work

A survey of the literature reports for the past few decades reveals that solid catalysts such as zeolites, metal oxides, clays, microporous aluminophospates are interesting catalytic materials, especially to catalyze alkylation reaction of aromatic compounds at C-, O-, and N- centers. Selective synthesis of NMA from aniline has been attempted at vapor phase conditions; however, secondary products like DMA and C-methylated anilines were also produced in sizeable amount under certain conditions, which considerably affects the NMA selectivity. Hence it has been decided to investigate aniline mono-N-methylation reaction, the reaction parameters are optimized to control the secondary products formation and the reaction mechanism through *in situ* FT-IR studies.

Except O-methylation of catechol other dihydroxybenzenes (resorcinol and hydroquinone) have not been investigated in detail. Since the acidity of these three substrates varies, their reactivity and the product selectivity are expected to change accordingly. Hence it is interesting to study the methylation of all the three substrates at comparable reaction conditions. This enables to derive a correlation between the reactivity and substrate acidity.

Though much research was done on methylation of aromatic compounds, there is a lack of understanding on reaction mechanism and the actual role of catalysts or active sites. Again correlations between electronic structure of the catalysts and catalytic activities have not been clearly established in many of the studies reported so far. A systematic stepwise approach to explore the above problems are listed below:

- Preparation of series of ferrospinels (AA'Fe_2O_4 where A = Fe, Cu and Zn and A' = Fe, Co, Ni, Cu and Zn) and evaluate them for selective NMA formation from aniline N-methylation using methanol as the alkylating agent and finalize a series for detailed study.
- Preparation of a highly NMA selective ferrospinels, containing Cu and Zn, having general formula of $Cu_{1-x}Zn_xFe_2O_4$ where x = 0.05, 0.25, 0.5, 0.75 and 1 by co-precipitation method.
- Characterization of $Cu_{1-x}Zn_xFe_2O_4$ by physicochemical and spectroscopic methods such as XRD, ICPS, Surface area (by N_2 sorption) FT-IR and electron microscopy.
- Most important was the evaluation of the catalytic activity of the systems for aniline N-methylation using methanol and to optimize the process parameters to achieve the synthetically more valuable NMA production in better yield.
- Detailed analysis of the fresh and the spent catalysts to understand the changes in electronic and structural changes that occur during aniline methylation. XRD and TPR, photoemission studies have been employed for the above purpose.
- Surface acidity of the catalysts was measured by *in situ* DRIFTS (Diffuse Reflectance Infrared Fourier Transform Spectroscopy) techniques using pyridine as an acidity probe. Evaluation of acidity by ammonia TPD was also carried out.
- Adsorption behavior of both reactants (aniline, methanol and aniline + methanol) and products of aniline methylation (NMA, DMA and o-toluidine) on the surface of the selected compositions of $Cu_{1-x}Zn_xFe_2O_4$ catalyst were studied by *in situ* DRIFTS technique.

- Alkali metal ions (Li, K and Cs) promoted commercial MgO was prepared by incipient wet impregnation method. Catalysts were characterized using XRD, Surface area measurement and electron microscopy.
- Dihydroxybenzenes O-methylation were carried out over alkali metal ions promoted MgO using DMC as methylating agent and reaction parameters were optimized to selectively synthesize the more valuable methoxyphenols.
- Characterization of spent catalysts after O-methylation of dihydroxybenzenes were carried out using XRD, XPS, TG-DTA and ^{13}C NMR.

1.13 Outline of the thesis

This thesis contains two different types of reactions on two different catalysts; (1) selective mono-N-methylation of aniline on $Cu_{1-x}Zn_xFe_2O_4$ and (2) is an attempt on the selective production of methoxyphenols from O-methylation of dihydroxybenzenes on alkali metal ions promoted MgO. The following are the chapter wise outline of the present thesis work.

Chapter 1 briefly describes the importance of heterogeneous catalysis and the need to carry out the alkylation of aromatic compounds, particularly heteroatom alkylation over ring alkylation. The advantages of using solid catalysts over conventional Friedel-Craft's catalysts, generally used for alkylation, were also discussed. In addition, reported results on methylation of aniline, phenol and catechol and the different types of catalysts attempted until now for these reactions were discussed. The main issues or drawbacks like undesired product formation, catalysts deactivation during reaction run was presented. Finally, the objective of the work undertaken and the need to carry out the same was mentioned.

Chapter 2 mainly deals with the experimental methods involved in the preparation of $Cu_{1-x}Zn_xFe_2O_4$ catalyst and the alkali metal ions promoted commercial MgO. The physico-chemical characterizations like XRD, Surface area (by N_2 sorption), electron microscopy, FT-IR and TPD results are presented and discussed.

Chapter 3 describes the catalytic reaction results from aniline N-methylation with methanol as methylating agent on $Cu_{1-x}Zn_xFe_2O_4$. Catalytic activity dependence on various reaction parameters such as temperature, feed ratio, space velocity and catalyst compositions are given and discussed. N-methylation of substituted anilines was also carried out at optimized reaction conditions and the results are discussed.

Chapter 4 describes the *in situ* DRIFTS studies on reactants and possible products of aniline methylation reaction adsorbed on the surface the $Cu_{1-x}Zn_xFe_2O_4$. A possible aniline methylation mechanism was proposed and demonstrated from the above studies.

Chapter 5 shows the photoemission studies on fresh and spent $Cu_{1-x}Zn_xFe_2O_4$ catalysts. XPS and XAES results from core levels and valence band levels are given and discussed in detail. The actual role of Zn, which enhances the catalyst stability during reaction condition, is established.

Chapter 6 describes the catalytic methylation results of dihydroxybenzenes over MgO and alkali metal ions promoted MgO using dimethylcarbonate as methylating agent. Catalytic activity dependence on various reaction parameters such as temperature, feed compositions, particle size and contact time are given. A correlation between the substrates acidity and their reactivity was derived.

Chapter 7 demonstrates the characterization of spent catalysts from dihydroxybenzene O-methylation using XRD, XPS, TG-DTA and ^{13}C NMR. The results were discussed and the possible reason for the catalysts deactivation during reaction was revealed.

Chapter 8 deals with the over all summary and conclusions derived from the present work. Promising ferrospinel $Cu_{1-x}Zn_xFe_2O_4$ catalyst for selective mono-N-methylation of aniline in which x = 0.5 composition shows stable catalytic activity. On the other hand, selective production of methoxyphenols from dihydroxybenzenes methylation was accomplished by employing K^+ ions promoted MgO.

1.14 References

1. G. Ertl, H. Knozinger, J. Weitkamp, Handbook of Heterogeneous Catalysis, Vol. 1 Wiley- VCH,Weinheim, 1997.
2. Industrial Organic Chemicals, Ullmann’s Encyclopedia, Wiley- VCH, 1 (1999).
3. G. Ertl, H. Knozinger, J. Weitkamp, Handbook of Heterogeneous Catalysis, Vol. 5 Wiley- VCH, Weinheim, 1997.
4. Phenol derivatives, Ullmann’s Encyclopedia of Industrial Chemistry, Wiley-VCH, A19 (1991).
5. Encyclopedia of Chemical Technology, Wiley, New York, 3rd edn. 2 (1978).
6. J. Kapsi, G. A. Olah, J. Org. Chem., 43 (1978) 3142.
7. P. Y. Chen, M. C. Chen, H. Y. Chu, N. S. Chang, T. K. Chuang, Proc. 7th Intern. Zeolite Conf., Kodansha, Tokyo and Elsevier, Amsterdam. (1986) 739.
8. J. March, Advanced Organic Chemistry, Wiley, New York, 4th edn. (1991).
9. A. K. Ko, C. L. Young, W. D. Zhu, H. E. Lin, Appl. Catal. A 134 (1996) 53.
10. Friedel-Crafts and Related Reaction, Interscience Publishers, New York, 1 (1963) 205.
11. K. Tanabe, M. Misono, Y. Ono, H. Hattori, Stud. Surf. Sci. Catal. 51 (1989).
12. B. Viswanathan, Bull. Catal. Soc. India. 1 (2000) 10.
13. L. K. Doraiswamy, G. R. V. Krishnan, S. P. Mukherjee, Chem. Eng. 88 (1981) 78.
14. V. V. Rao, V. Durgakumari, S. Narayanan, Appl. Catal. 49 (1989) 165.
15. H. Matsuhashi, K. Arata, Bull. Chem. Soc. Jpn. 64 (1991) 2605.
16. S. Narayanan, B. P. Prasad, J. Chem. Soc. Chem. Commun. (1992) 1204.
17. F. Valot, F. Fache, R. Jacquot, M. Spagnol, M. Lemaire, Tetrahedron Lett. 40 (1999) 3689.
18. M. Onaka, K. Ishikawa, Y. Izumi, Chem. Lett. (1982) 1783.

19. P. Y. Chen, M. C. Chen, H. Y. Chu, N. S. Chang, T. K. Chaung, Stud. Surf. Sci. Catal. 28 (1986) 739.
20. Y. K. Park, K. Y. Park, S. I. Woo, Catal. Lett. 26 (1994) 169.
21. S. Narayanan, V. Durgakumari, A. S. Rao, Appl. Catal. 111 (1994) 133.
22. B. L. Su, D. Barthomeuf, Appl. Catal. A: Gen. 124 (1995) 73.
23. B. L. Su, D. Barthomeuf, Appl. Catal. A: Gen. 124 (1995) 81.
24. P. S. Singh, R. Bandhopadhya, Appl. Catal. A: Gen. 136 (1996) 177.
25. L. J. Graces, V. D. Makwana, B. Hincapie, A. Sacco, S. L. Suib, J. Catal. 217 (2003) 107.
26. J. Santhalakshmi, T. Raja, Appl. Catal. A: Gen. 147 (1996) 69.
27. T. M. Jyothi, T. Raja, M. B. Talawar, K. Sreekumar, S. Sugunan, B. S. Rao, Syn. Commun. 30 (2000) 3929.
28. F. M. Baustista, J. M. Campelo, G. D. Luna, J. M. Marinas, A. A. Romero, M. R. Urbano, J. Catal. 172 (1997) 103.
29. F. M. Baustista, J. M. Campelo, G. D. Luna, J. M. Marinas, A. A. Romero, Stud. Surf. Sci. Catal. 108 (1997) 123.
30. F. M. Baustista, J. M. Campelo, G. D. Luna, J. M. Marinas, A. A. Romero, Appl. Catal. A: Gen. 166 (1998) 39.
31. S. Prasad. B. S. Rao, J. Mol. Catal. 62 (1990) L17.
32. Z. H. Fu, Y. Ono, Catal. Lett. 18 (1993) 59.
33. Z. H. Fu, Y. Ono, Catal. Lett. 22 (1993) 277.
34. P. R. Hariprasad, P. Missiani, D. Barthomeuf, Catal. Lett. 31 (1995) 115.
35. P. R. Hariprasad, P. Missiani, D. Barthomeuf, Stud. Surf. Sci. Catal. 84 (1994) 1449.
36. M. Selva, A. Bomben, P. Tuldo, J. Chem. Soc. Perkin. Trans. 1 (1997) 1042; ; M. Selva, P. Tundo, A. Perosa, J. Org. Chem. 66 (2001) 677; M. Selva, P. Tundo, A.

Perosa, J. Org. Chem. 67 (2002) 9238; M. Selva, P. Tundo, A. Perosa, J. Org. Chem. 68 (2003) 7374.

37. S. P. Elangovan, C. Kannan, B. Arabindo, V. Murugesan, Appl. Catal. A:Gen. 174 (1998) 213.
38. K. Sreekumar, T. M. Jyothi, T. Mathew, M. B. Talawar, S. Sugunan, B. S. Rao, J. Mol. Catal. A: Chem. 159 (2000) 327.
39. K. Sreekumar, T. Mathew, S. P. Mirajkar, S. Sugunan, B. S. Rao, Appl. Catal. A: Gen. 201 (2000) L1.
40. K. Sreekumar, T. M. Jyothi, T. Mathew, M. B. Talawar, S. Sugunan, B. S. Rao, J. Mol. Catal. A: Chem. 152 (2000) 225.
41. K. Sreekumar, T.Raja, B. P. Kiran, S. Sugunan, B. S. Rao, Appl. Catal. A: Gen. 182 (1999) 327.
42. R. Bal, S. Sivasanker, Appl. Catal. A: Gen. 246 (2003) 373.
43. R. Bal, S. Sivasanker, Green Chem. 2 (2000) 106.
44. R. Pierantozzi, A. F. Nordquist, Appl. Catal. 21 (1986) 263.
45. M. C. Samolada, E. Grigoriadou, Z. Kiparissides, I. A. Vasalos, J. Catal. 152 (1995) 52.
46. G. Sarala Devi, D. Giridhar, B. M. Reddy, J. Mol. Catal. A: Chem. 181 (2002) 173.
47. S. Balsama, P. Beltrame, P. L. Beltrame, P. Carniti, L. Forni, G. Zurelti, Appl. Catal. 13 (1984) 161.
48. Y. Fu, T. Baba, Y. Ono, Appl. Catal. A: Gen. 166 (1998) 419.
49. Y. Fu, T. Baba, Y. Ono, Appl. Catal. A: Gen. 166 (1998) 425.
50. Y. Fu, T. Baba, Y. Ono, Appl. Catal. A: Gen. 176 (1998) 201.
51. Y. Fu, T. Baba, Y. Ono, Appl. Catal. A: Gen. 178 (1999) 219.
52. L. Calzolari, F. Cavani, T. Monti, Solid State Chem. Catal. 3 (2000) 533.

53. F. Cavani, T. Monti, Catalysis of Organic reactions 82 (2001) 123.
54. F. Cavani, T. Monti, D. Paoli, Stud. Surf. Sci. Catal. 130 (2000) 2633.
55. V. Vishwanathan, S. Ndou, L. Sikhwivhilu, N. Plint, K. Vijayaraghavan, N. J. Coville, Chem. Commun. (2001) 893.
56. M. B. Talawar, T. M. Jyothi, P. D. Sawant, T. Raja, B. S. Rao, Green Chem. 2 (2000) 266.
57. T. M. Jyothi, T. Raja, M. B. Talawar, B. S. Rao, Appl. Catal. A: Gen. 211 (2001) 41.
58. L. Kiwi-Minsker, S. Porchet, R. Doepper, A. Renken, Stud. Surf. Sci. Catal. 108 (1999) 149.
59. L. Kiwi-Minsker, G. Jenzer, L. Pliasova, A. Renken, Stud. Surf. Sci. Catal. 121 (1999) 159.
60. R. Bal, B. B. Tope, S. Sivasanker, J. Mol. Catal. A: Chem. 181 (2002) 161.
61. R. Bal, S. Mayadevi, S. Sivasanker, Organic Process Res. Development 7 (2003) 17.
62. X. Zhu, X. Li, M. Jia, G. Liu, W. Zhang, D. Jiang, Appl. Catal. A: Gen. 282 (2005) 155.
63. Z. Fu, Y. Y. D. Yin, Y. Xu, H. Liu, H. Liao, Q. Xu, F. Tan, J. Wang, J. Mol. Catal. A: Chem. 232 (2005) 69.
64. V. E. Henrich, Rep. Prog. Phys. 48 (1985) 1481.
65. M. A. Barteau, Chem. Rev. 96 (1996) 1413.
66. A. Zecchina, D. Scarano, S. Bordiga, G. Spoto, C. Lamberti, Adv. Catal. 46 (2001) 265.
67. H. L. Emerson, Cata. Rev. 8 (1973) 285.
68. A. Clark, Cata. Rev. 3 (1969) 145.
69. T. Kotanigawa, M. Yamamoto, K. Shimokawa, Y. Yoshida, Bull. Chem. Soc. Jpn. 44 (1971) 1961.

70. T. Kotanigawa, K. Shimokawa, Bull. Chem. Soc. Jpn. 47 (1974) 1555.
71. T. Kotanigawa, Bull. Chem. Soc. Jpn. 47 (1974) 950.
72. T. H. Evan, A. N. Bourns, Can. J. Tech. 29 (1951) 1.
73. A. G. Hill, J. H. Shipp, A. J. Hill, Ind. Eng. Chem. 43 (1981) 1579.
74. J. M. Parera, A. Gonzalez, M. M. Barral, Ind. Eng. Chem. Prod. Res. Dev. 7 (1968) 259.
75. B. M. Reddy, A. Khan, Cata. Rev. 47 (2005) 257.
76. Y. Ono, T. Baba, Catal. Today, 38 (1997) 327.
77. H. Hattori, Chem. Rev, 95 (1995) 537.
78. H. Hattori, Stud. Surf. Sci. Catal. 78 (1993) 35.
79. B. M. Choudary, V. Bhaskar, M. L. Kantam, K. Koteswara Rao, K. V. Raghavan, Green Chem. 2 (2000) 67.
80. F. Cavani, F. Trifiro, A. Vaccario, Catal. Today, 11 (1991) 173.
81. S. Tsuchiya, S. Takase, H. Imamura, Chem. Lett. (1994) 661.
82. T. Matsuda, Z. Minami, Y. Shibata, S. Nagano, H. Miura, K. Sugiyama, J. Chem. Soc. Faraday Trans. 82 (1986) 1357.
83. E. Ruckenstien, A. Z. Khan, J. Catal. 141 (1993) 628.
84. A. Z. Khan, E. Ruckenstien, Appl. Catal. A: Gen. 102 (1993) 233.
85. G. M. Schwab, E. Roth, C. H. Grinzoz, N. Mavrakis, Structure and Properties of Solid surfaces, Univ. Chicago Press, Chicago (1953).
86. J. P. Suchet, Chemical Physics of Semiconductors, Van Nostrand, London. Chap.5 (1965) 82.
87. W. R. Moser, J. Happel, Catalytic Chemistry of Solid-state Inorganics, Acad. Sci. 272 (1976) 1.
88. G. Blasse, Phillips Research Rep. Supplement, 3 (1964) 40.

89. J. P. Bautiles, Y. Barboax, J. Appl. Cryst. 15 (1982) 665.
90. J. P. Jacobs, A. Maltha, J. G. H. Reintjes, J. Drimal, V. Ponec, H. H. Brongersma, J. Catal. 147 (1994) 294.
91. J. Ziolkowski, Y. Barbaun, J. Mol. Catal. 67 (1991) 199.
92. T. Mathew, N. R. Shiju, K. Sreekumar, B. S. Rao, C. S. Gopinath, J. Catal. 210 (2002) 405.
93. T. Mathew, B. S. Rao, C. S. Gopinath, J. Catal. 222 (2004) 107.
94. C. S. Narashimhan, C. S. Swamy, Appl. Catal. 2 (1982) 315.
95. A. J. Marchi, J. I. Dicosimo, C. R. Apesteguia, "Proceedings, 4th International Symposium on Scientific Bases for the preparation of Heterogeneous catalysts", Louvainla Neuve, Paper H-7 (1986).
96. A. J. Marchi, J. I. Dicosimo, C. R. Apesteguia, "Proceedings, 4th International Congress on Catalysis" (J. M. Philips and M. Ternan, Eds), Vol. 2 (1988) 529.
97. P. Courty, C. Marcilly, Stud. Surf. Sci. Catal. 1 (1976) 119.
98. J. A. Scwarz, C. Contescu, A. Contescu, Chem. Rev. 95 (1995) 484.
99. L. Hench, J. K. West, Chem. Rev. 90 (1990) 33.
100. M. Schneider, A. Baiker, Catal. Rev. Sci. & Eng. 37 (1995) 515.
101. R. Gopichandran, K. C. Patil, Mater. Lett. 12 (1992) 437.
102. S. S. Manoharan, K. C. Patil, J. Amer. Ceram. Soc. 75 (1992) 1012.
103. A. K. Cheetand, P. Day, Solid State Chemistry Techniques, Oxford University Press (1987).
104. F. A. Cotton, G. Wilkinson, Advanced Inorganic Chemistry, Wiley, NY, 4th edn. (1980).
105. G. Ertl, H. Knozinger, J. Weitkamp, Handbook of Heterogeneous Catalysis, Vol. 2 Wiley- VCH,Weinheim, 1997.

106. C. J. Powell, D. M. Hercules, A. W, Czanderna, Ion Spectroscopy for Surface Analysis, New York (1991) 417.
107. B. M. Weckhuysen, In situ spectroscopy of catalysts, American scientific publishers, California, 2004.
108. J. F. Haw, In situ spectroscopy in heterogeneous catalysis, Wiley-VCH, Weinheim 2002.
109. J. F. Watts, J. Wolstenholme, Introduction to surface analysis by XPS and AES, Wiley, Chichester, 2003.

Chapter 2: Preparation and characterization of catalysts

2. 1 Catalysts preparation

2.1.1 $Cu_{1-x}Zn_xFe_2O_4$ (x = 0.05, 0.25, 0.5, 0.75 and 1) synthesis

Ferrospinel catalysts containing Cu and Zn were prepared by co-precipitation technique as described in the literature [1]. AR grade chemicals procured from Merck chemicals were used as supplied, without any further purification. Stoichiometric amounts of premixed metal nitrates, ($Cu(NO_3)_2.3H_2O$, $Zn(NO_3)_2.6H_2O$ and $Fe(NO_3)_2.9H_2O$) solutions were rapidly added to the 5.4M sodium hydroxide solution at room temperature under constant and vigorous stirring. Final pH of the resulting precipitate in the solution was adjusted between 9 and 9.5 followed by aging for 12 hours. The precipitate was washed well for more than 25 times with distilled water till the filtrate is free from Na^+ and NO_3^- ions. The precipitate was filtered and dried at 353 K in an air oven for about 36 hours. The dried material was powdered and calcined at 773 K for 8 h.

2.1.2 Alkali metals loaded MgO synthesis

Commercial magnesium oxide (Merck, India) was procured and used as a catalyst. Pure magnesium oxide was promoted with alkali metal ions (Li, K and Cs) and the amount of alkali metal ions loaded was 5mMol per gram of MgO. The alkali metal ions were loaded on MgO by incipient wet impregnation method using aqueous solution of $LiOH.H_2O$, KNO_3, and $CsNO_3$ at 353 K [2]. The as-synthesized catalysts were dried at 383 K for 12h.

2.2 Physicochemical characterization

2.2.1 Introduction

Physicochemical characterization is an important area to understand any material including catalyst. Spectroscopy, microscopy, diffraction and methods based on adsorption and desorption or bulk reactions (reduction or oxidation) are the routine catalyst characterization techniques. All the characterization tools offer to get information about crystallinity, surface structures, nature of the active sites, electronic structures, particle size and morphology, acid-base properties and other characteristic features like catalyst bulk compositions and surface compositions. With such information it helps to understand the catalyst better and correlate the structure and composition of the catalyst with its performance, so that improvement of the catalyst and its performance are possible. The performance of the catalyst is normally estimated in terms of its activity and stability and how much it is selective towards a desired product.

The fresh catalyst samples were characterized by various characterization techniques such as XRD, *in situ* DRIFTS (Diffuse reflectance infra red Fourier transform spectroscopy), surface area and pore volume measurements, SEM, TG-DTA, TPR, TPD, XPS and ^{13}C NMR. The present chapter briefly describes the theory and principle of various characterization techniques used for the present study. The procedure for each experimental technique is given in this chapter. Results and discussions from XPS studies on fresh and spent catalysts, *in situ* DRIFTS study on reactants and products of aniline N-methylation, TPR of $Cu_{1-x}Zn_xFe_2O_4$, TG-DTA and ^{13}C NMR analysis of spent catalysts are extensively used for comparing with catalytic reaction results. Hence they are presented and discussed in the forthcoming chapters.

2.2.2 Theory and experimental procedures

2.2.2.1 X-ray diffraction (XRD)

XRD is one of the oldest and most frequently exploited techniques in catalyst characterization. It is used to identify crystalline phase(s) of the catalyst by means of lattice structural parameters and to obtain an indication of crystallite size and crystallinity.

X-ray diffraction occurs in the elastic scattering of X-ray photons by atoms from the periodic lattice. The scattered monochromatic X-rays that are *'in-phase'* give constructive interference. If the distance between two periodic lattice planes is 'd' and the angle between the incoming X-rays and the normal to the reflecting lattice plane is 'θ' then the well-known Bragg's equation [3] is

$$n\lambda = 2d\ sin\theta\ ;\ n = 1, 2, 3, \ldots \tag{1}$$

where λ is the wavelength of the X-rays and n is an integer called the order of the reflection. By measuring the angle, 2θ, under which constructively interfering X-rays leave the crystal, the Bragg's equation (1) gives the corresponding lattice spacings, which are characteristic for a particular compound.

Width of the diffraction peaks signifies the dimension of the reflecting planes. Diffraction lines from the perfect crystals are very narrow. For crystals with size below 5 nm, peak broadening occurs due to incomplete and somewhat destructive interference in scattering directions where the X-rays are *'out of phase'*. The Scherer formula [4] relates crystal size to line width:

$$\langle L \rangle = \frac{K\lambda}{\beta\ cos\theta} \tag{2}$$

where < L > is a measure of the dimension of the crystal in the direction perpendicular to the reflecting plane, λ is the X-ray wavelength, β is the peak full width at half maximum (FWHM), θ is the angle between the beam and the normal to the reflecting plane and K is a constant (often taken as 1). Powder X-ray diffraction patterns of all the catalysts reported in this work were recorded using a Rigaku Giegerflex instrument equipped with Cu Kα radiation (λ = 1.5406 Å) with a Ni-filter.

2.2.2.2 Surface area determination by BET Method

The BET (Brunauer-Emmett-Teller) method is the most widely employed procedure to determine the surface area of the solid materials. By using the BET equation (3):

$$\frac{P}{V_a(P_0 - P)} = \frac{1}{V_0\chi} + \frac{(\chi - 1)}{\chi V_0}\frac{P}{P_0} \equiv \eta + \alpha\frac{P}{P_0} \tag{3}$$

where P = adsorption equilibrium pressure, P_0 = standard vapor pressure of the adsorbate, V_a = volume at STP occupied by molecules adsorbed at pressure P, V_0 = volume of adsorbate required for a monolayer coverage, χ = constant related to heat of adsorption.

Plotting $P/\left[V_a(P-P_0)\right]$ versus P/P_0 yields a straight line with a slope $\alpha = (\chi - 1)/\chi V_0$, crossing the y-axis at $\eta = 1/\chi V_0$. The volume adsorbed in the first monolayer is found as $V_0 = 1/(\alpha + \eta)$. The volume V_0 can be converted into the number of molecules adsorbed by $N_0 = PV_0/RT$ and if we know how big an area occupies by each molecule (A_0) then the total area, $A = N_0A_0$, can be found. For N_2 molecule $A_0 = 0.16\mathrm{nm}^2$.

To differentiate the adsorption mechanism between micropore and to that in meso and macropores, the t-plot analysis was developed by Lippens and de Boer and the same was applied [5]. The method consists of plotting the adsorption isotherm in terms of the volume of the adsorbate versus the statistical film thickness, t. The pore size distribution is obtained from the analysis of the desorption isotherms by applying the BJH model [6] which involves the area of the pore walls and uses the Kelvin equation to correlate the partial pressure of nitrogen in equilibrium with the porous solid to the size of the pores where the capillary condensation takes place.

The BET surface area and pore volume of the catalysts were determined by N_2 adsorption-desorption method at liquid N_2 temperature (77 K) using Quantachrome Nova 1200 adsorption unit. About 200 mg of sample was degassed at 473 K for about 2 hours till the residual pressure was < 10^{-3} Torr. The isotherms were analyzed in a conventional manner that includes the BET surface area in the region of the relative pressure P/P_0 = 0.05 to 1 with the assumption for the nitrogen molecular area in an adsorbed monolayer is 0.16 nm^2. The total pore volume of each samples were taken at P/P_0 = 0.95.

2.2.2.3 Diffuse reflectance infrared Fourier transform spectroscopy (DRIFTS)

Infrared techniques have got remarkable importance in the field of heterogeneous catalysis. The most common application is to identify adsorbed species and to study the way in which these species are chemisorbed on the surface of the catalyst. Hence in the field of surface chemistry and catalysis over metal oxides catalyst, highly useful information are acquired by employing FT-IR techniques. A variety of FT-IR techniques have been used in order to get information on the surface chemistry of different solid catalysts. With respect to the characterization of metal oxide catalysts two techniques largely predominate, namely, the transmission/absorption and the diffuse reflectance techniques.

In recent years, the use of FT-IR spectroscopy in the diffuse reflectance mode is grown strongly since the sampling does not require any particular efforts. In diffuse reflectance mode, a major advantage is that the sample can be used as loose powders and the tedious preparation of wafers can be avoided. Diffuse reflectance is also the indicated technique for strongly scattering materials employed in heterogeneous catalysis. Kubelka and Munk [7] developed the theory of diffuse reflectance spectra and extended by Kortum et al. [8]. According to this theory:

$$f(R_\infty) = \frac{(1 - R_\infty)^2}{2R_\infty} = K/S \tag{4}$$

where R_∞ is the reflectivity of a sample of infinite thickness, measured as function of frequency ν, K is the absorption coefficient, a function of ν and S is the scattering coefficient. If the scattering coefficient does not depend on the infrared frequency, the Kubelka-Munk function transforms the measured spectrum R_∞ into the absorption spectrum (K). A great advantage of infrared spectroscopy is that the technique can be used to study catalysts under working conditions in the real world or conditions close to that. Several cells for *in situ* investigations have been described in the literature [9, 10]. *In situ* cells for the DRIFTS studies of catalyst have been described [11] and are commercially available. FT-IR spectra were recorded on Shimadzu (SSU8300) spectrometer equipped with MCT-A detector. The samples were scanned through DRIFT mode in the range between 400 and 4000 cm^{-1}. *In situ* FT-IR spectra of the samples with various adsorbed molecules were also recorded through DRIFT technique. The calcined samples were placed in a Spectra-tech made DRIFTS cell with Zn-Se window (Model 0030-067) and heated *in situ* to 673 K for 3 h at a heating rate of 5 K/min in 99.99% pure N_2 stream and then the hydroxyl region of the spectra was measured. The sample was then cooled to 333 K and 10 μL of any compound or reaction mixture was introduced separately for 10 min in the N_2 flow. The temperature was increased under N_2 flow and the spectra were recorded at different temperatures between 333 and 623 K. 4 cm^{-1} resolution was attained after averaging over 500 scans. All the spectra presented here as the difference spectra between molecule(s) adsorbed on catalyst and activated fresh catalyst.

2.2.2.4 Temperature programmed techniques

Temperature programmed methods forms a class of techniques in which a chemical reaction is monitored while the temperature increases linearly with time [12, 13]. Several forms of temperature programmed techniques are in use; they are reduction (TPR), oxidation (TPO), sulfidation (TPS) desorption (TPD), reaction spectroscopy (TPRS) and thermal desorption spectroscopy (TDS). All these techniques are applicable to real catalyst and have the advantage that they are experimentally simple in comparison to many other spectroscopy techniques. Interpretation on a quantitative basis is rather straightforward. However, obtaining reaction parameters such as activation energies or preexponential factors from temperature programmed methods is complicated. The basis set up for TPR, TPO, and TPD consists of a reactor and a thermal conductivity detector to measure the effluent gas content during the measurements.

In TPR technique the catalyst material is normally subjected to a linear temperature program, while a reducing gas mixture is flowing over it (usually H_2 diluted in some inert gas like Ar). The reduction rate or H_2 disappearance is continuously measured by monitoring the change in composition of the gas mixture after passing through the reactor. The decrease in H_2 concentration in the effluent gas with respect to the initial percentage monitors the reaction progress.

TPD is a technique for studying the kinetics of desorption of adsorbate(s) from solid surface. The data collected under well-controlled UHV conditions provides kinetic parameters as a function of adsorbate surface coverage. The sample temperature is heated (by variety of means) in a controlled fashion. The mass spectrometer is tuned to monitor one or more mass fragments simultaneously as a function of time and in coherence with temperature measurements. The desorption temperature, the shape of the desorption peak and how all these changes with initial surface coverage and heating rate are all analyzed to provide information about the binding character of the adsorbate/substrate.

TPR and TPD on catalysts were performed by a Micromeritics Autochem 2910 catalyst characterization system equipped with thermal conductivity detector. TPR measurements were carried out by taking about 20 mg of calcined catalysts activated at 773 K for 1 h in Ar flow in a conventional flow through a quartz reactor. After cooling to ambient temperature, the argon flow was replaced with 5% H_2/Ar mixture. The catalysts were heated to 1073 K at a heating rate of 5 K/min. A flow rate of 30 ml/min was maintained throughout the experiments for all the catalysts.

TPD measurements were carried out by taking about 250 mg of catalyst sample was activated in a stream of UHP grade He (20 mL/min) at 773 K for 1h. The activated sample was cooled to 323 K and equilibrated with 5% NH_3 balanced in He for 30 min. Physisorbed NH_3 was removed by evacuation at 373 K for 30 min. TPD profile was recorded while the sample was ramped up to 973 K at a rate of 5 K/min in a He stream (20 mL/min). Both in TPR and TPD the effluent gas was passed through a cooled trap before it entered the thermal conductivity detector. The detector signal was recorded and the data was processed using a computer.

2.2.2.5 Scanning electron microscopy (SEM)

Electron microscopy is a straightforward technique to determine the size and shape of the materials. Electrons have characteristic wavelengths less than an Ångstrom amount to seeing atomic detail. Primarily electron beam of energy between 100 and 400 KeV is used. The interaction between the electron beam and the sample in an electron microscope leads to a number of detectable signals. SEM detects the yield of either secondary or backscattered electrons by particles as a function of the position of the primary electron beam. The secondary electrons have mostly low energies (≈ 5 – 50 eV) and originate from the surface region of the sample. Dark field images are caused with respect to the sample orientation: parts of the surface facing the detector appear brighter than parts of the surface with their surface normal pointing away from the detector. The size and morphology of all the catalysts were examined using a JEOL JSM-840A scanning electron microscope.

2.2.2.6 Thermal analysis (TG and DTA)

Thermal analysis includes a group of methods by which the physical and chemical properties of a substance, a mixture and/or reaction mixture are determined as a function of temperature (or time), while the sample is subjected to a controlled linear temperature program. In thermogravimetry (TG), the weight loss of the sample is monitored as a function of temperature (or time) during controlled temperature program. The percentage weight loss with respect to temperature (or time), generally as a function of temperature is acquired. However, the exact temperature at which the weight loss occurs can be determined by taking the derivative signal of the thermogravimetry and is known as differential thermogravimetry (DTG). Differential thermal analysis (DTA) measures the difference in temperature between a sample and a thermally inert reference material as the temperature is raised. A plot of this differential provides information on exothermic and endothermic reactions taking place in the sample, which include phase transitions, dehydration, decomposition, redox, or solid-state reactions.

Thermogravimetry and differential thermal analysis measurements were performed with a Mettler Toledo system equipped with a controller and a data acquisition system. About 10 - 25 mg catalysts were subjected to linear heating in air at a rate of 10 K/min up to a maximum of 1473 K or as required.

2.2.2.7 Photoelectron spectroscopy

The photoelectron spectroscopy [14-16] is based on the photoelectric effect that involves the interaction of sample surface with UV or X-rays and the measurement of the concomitant photoemitted electrons energy. The photoemitted electrons have discrete kinetic energies that are characteristic of the emitting atoms and their bonding states. The kinetic energy, E_k, of these photoelectrons is determined from the energy of the incident X-ray radiation (hν) and the electron binding energy (E_b) is given as

$$E_K = h\nu - E_b \qquad (5)$$

The experimentally measured energies of the photoelectrons are given as

$$E_K = h\nu - E_b - E_w \qquad (6)$$

where E_w is the work function of the spectrometer.

The XPS technique is highly surface sensitive due to the short-range mean free path of the photoelectrons that are excited from the solid. The binding energy of the peaks is characteristic of each element. The peak area can be used (with appropriate sensitivity factors) to determine the surface compositions of the material. The shape and the binding energy of the peak vary due to different chemical state of the emitting ion and its surroundings. Hence XPS can provide chemical bonding information as well. XPS and the related X-ray induced Auger electron spectroscopy (XAES) can provide surface elemental analysis essentially for all the elements in the entire periodic table except H and He. The electrons arise from a depth of not greater than about 5 nm are analyzed, the technique is surface sensitive.

X-ray photoelectron spectra were acquired on a VG Microtech Multilab ESCA 3000 spectrometer using a non-monochromatized MgK_α X-ray source (hν = 1253.6 eV) on *in situ* scraped fresh sample pellets and powder samples of spent catalysts at room temperature. Selected spectra were recorded with Al K_α X-ray source (hν = 1486.6 eV) also to eliminate the overlap between different Auger and core levels. Base pressure in the analysis chamber was maintained at $3 – 6 \times 10^{-10}$ Torr range. The energy resolution of the spectrometer was determined from the full width at half maximum (FWHM) of metallic gold and the value obtained is better that 0.8 eV for MgK_α radiation and 1.1 eV for Al K_α radiation, at a pass energy of 20 eV. The error in the BE values found is ± 0.1 eV.

2.2.2.8 Solid state ^{13}C NMR

Modern NMR spectrometers record the decay of the magnetic induction of nuclear spin produced by irradiation with radio frequency pulse. After Fourier transformation of above induction decay produces, the spectrum of resonance signals of nuclear spins as function of frequency. The most important parameter of solid-state NMR spectroscopy is the chemical shift, $\delta = 10^6(\gamma - \gamma_{\text{ref}})/\gamma_0$, where γ and γ_{ref} are the resonance frequencies of the sample under observation and of the reference material, respectively, and γ_0 is the spectrometer operating frequency. Chemical shift is caused by the shielding effect of the electron shell and it gives information on the chemical nature of the atoms under study. The broad signal arises due to anisotropic properties of solids rendered the spectra analysis very difficult or even impossible, until the entry of magic angle spinning (MAS) technique. The line broadening due to chemical shift anisotropy contains the angular term $3\cos\theta - 1$, which becomes zero at magic angle ($\theta = 54.7^\circ$) [17].

In addition, cross polarization (CP) technique is employed to improve the sensitivity (the signal to noise ratio) of the spectra of nuclei with low natural abundance (for instance ^{13}C, ^{29}Si) [17]. Solid-state ^{13}C NMR generally hinges upon these MAS and CP techniques and producing high quality resolved spectra. High-resolution solid state ^{13}C NMR is a powerful tool for the investigation of carbonaceous deposits responsible for the catalyst deactivation [18,19]. The results reported in this thesis on ^{13}C CPMAS (cross polarization magic angle spinning) NMR measurements were carried out with MSL Bruker spectrometer operating at 75.15 MHz on solid spent catalysts.

2.2.3 Results and discussion

2.2.3.1 Physicochemical characterization of $Cu_{1-x}Zn_xFe_2O_4$

Table 2.1: Chemical Analysis, XRD parameter and textural properties of $Cu_{1-x}Zn_xFe_2O_4$.

X	Metal Concentration (wt%)			Crystallite Size (nm)	Lattice Constant 'a' (Å)	S_{BET} (m^2/g)	Pore Volume (cm^3/g) 10^{-2}
	Cu	Zn	Fe				
0.05	22.94	1.19	57.65	10.0	8.3459	23.0	9.5
0.25	21.65	5.51	54.43	15.9	8.4090	45.2	7.3
0.5	15.02	10.40	50.70	10.7	8.4052	49.3	13.6
0.75	6.82	16.70	50.04	11.7	8.4150	42.0	12.3
1	-	24.22	49.56	13.0	8.4180	35.0	12.5

Table 2.1 shows the chemical compositions (determined from ICPS), structural and textural properties measured from $Cu_{1-x}Zn_xFe_2O_4$ spinel catalysts prepared for aniline N-methylation in the present study. ICPS (Inductively coupled plasma spectroscopy) results show the bulk metal ion concentration in weight percent, which is in line with starting

composition of the catalyst. Figure 2.1a shows the XRD reflection patterns from fresh calcined catalysts. It can be seen that all the fresh samples exhibit diffraction reflections attributed to the spinel phase. However, impurities like CuO, Fe_2O_3 phases are also identified as reported in JCPDS files.

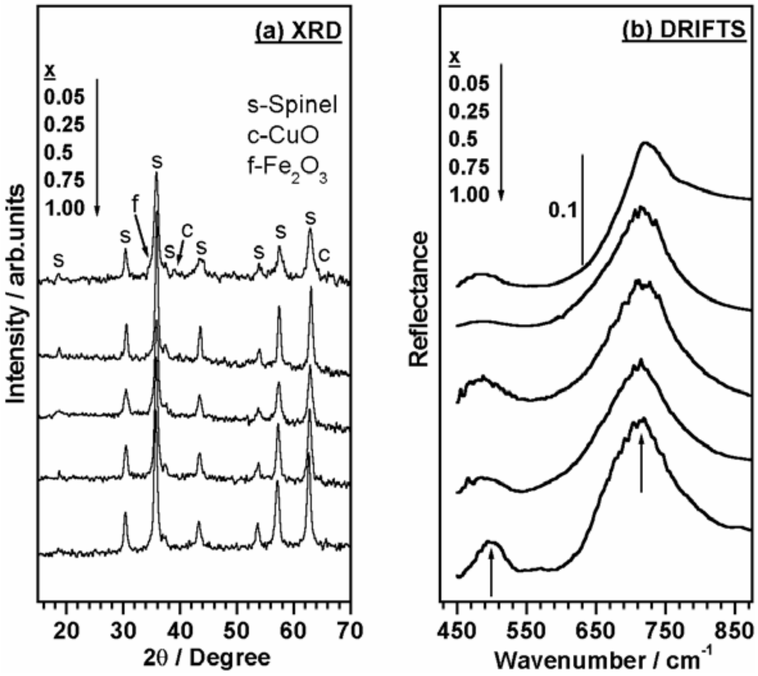

Figure 2.1: (a) XRD patterns and (b) DRIFTS of $Cu_{1-x}Zn_xFe_2O_4$ samples recorded at room temperature after calcination at 773 K. Arrows indicate ν_{M-O} of T_d (715 cm^{-1}) and O_h (495 cm^{-1}) coordinated cations.

It is clear that the spinel phase formation was not complete, especially for copper rich system (x = 0) even at 773 K [20]. Hence x = 0.05 was chosen to have a Cu rich system, in which small amount of Zn was added mainly to suppress all the impurity phases as much as possible and to have a Cu rich system. A comparison between earlier reported XRD pattern of $CuFe_2O_4$ [20] and the present one on x = 0.05 shows, indeed the impurities disappeared to a large extent, but not completely, and a corresponding increase in spinel phase was observed. The fine particle size of the spinels is evident from the crystallite size of the samples calculated using the Debye-Scherer equation (Table 2.1).

Figure 2.1b shows DRIFTS of $Cu_{1-x}Zn_xFe_2O_4$ samples recorded at room temperature after calcination at 773 K. The spectra show the metal ions distribution in two different environments at 715 cm^{-1} (ν_1) and 495 cm^{-1} (ν_2) and they are attributed to tetrahedral (T_d) and octahedral (O_h) coordinated metal-oxygen bands, respectively [21].

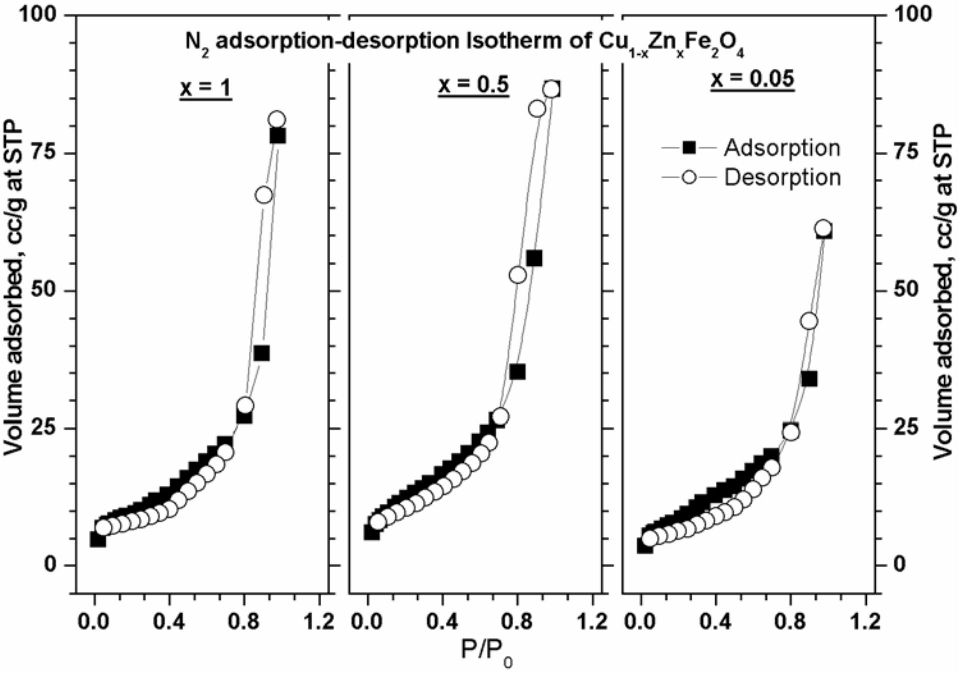

Figure 2.2: N_2 adsorption-desorption isotherms obtained from the surface area analysis of $Cu_{1-x}Zn_xFe_2O_4$ at 77 K.

The results obtained from the surface area analysis of $Cu_{1-x}Zn_xFe_2O_4$ are summarized in Table 2.1. N_2 adsorption-desorption isotherms were shown in Figure 2.2 for selected compositions. All the compositions show the isotherm with a combination of type II and type IV nature. At lower values of $P/P_0 < 0.8$ the isotherm is similar to type II, typical for nonporous materials. However, a rapid increase in volume of N_2 adsorbed was observed at higher $P/P_0 > 0.8$ shows type IV isotherm involved in the samples. The type IV isotherm indicates the presence of small amount of mesoporosity in the samples. The largest volume of N_2 adsorbed on x = 0.5 sample compared to other two compositions is well reflected by the adsorption isotherm. The average pore diameter is 10 Å for all the samples.

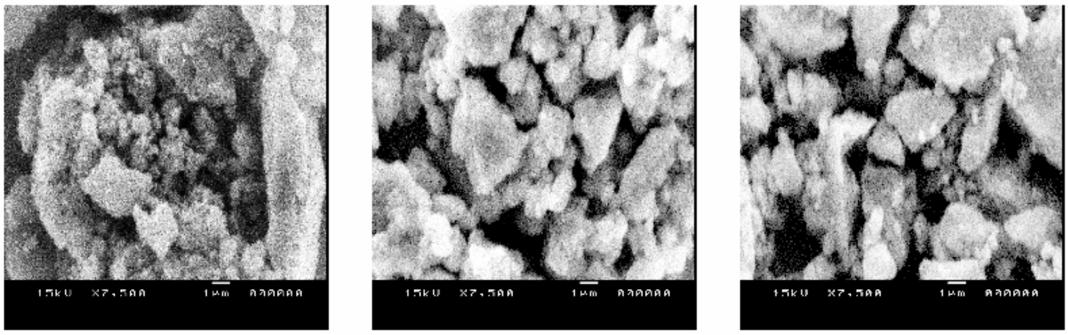

(a) x = 0.05 **(b) x = 0.5** **(c) x = 1**

Figure 2.3: Scanning electron micrographs (SEM) of calcined $Cu_{1-x}Zn_xFe_2O_4$ systems. Only representative samples were given.

Figure 2.3 shows the scanning electron micrographs of $Cu_{1-x}Zn_xFe_2O_4$ for selected compositions (x = 0.05, 0.5 and 1), which were calcined at 773 K for 8 h. The crystalline nature of the catalysts is revealed and the crystalline aggregates containing particles with size ranges between 1-10 μm was observed. Thus the SEM results well support and reflects the crystalline nature of the samples found from X-ray diffraction analysis.

2.2.3.2 FT-IR of pyridine adsorbed on $Cu_{1-x}Zn_xFe_2O_4$

2.2.3.2a Introduction

Pyridine adsorption followed by temperature dependent FT-IR study is a powerful probe to identify the presence and the nature of Lewis and Bronsted acid sites, which play an important role in the performance of oxide catalyst [22-26]. The vibration modes of pyridine are affected due to its interaction with the catalyst surface. The most affected vibrations of pyridine molecule are the ring-stretching vibration modes 19b and 8a at 1438 and 1580 cm^{-1}, respectively [27]. The above two modes, 19b and 8a are observed at 1440-1450 and 1580-1630 cm^{-1}, respectively for pyridine molecule interacting with the catalyst. Hydrogen-bonded pyridine observed at 1440-1447 cm^{-1} (ν_{19b}) and 1580-1600 cm^{-1} (ν_{8a}) and pyridinium ion (PyH^+) due to Bronsted acidity at 1485-1500 cm^{-1} and 1540 or 1640 cm^{-1} is observed. However, the hydrogen-bonded pyridine is only observed at low evacuation temperatures (below 473 K) [28]. Pyridine coordinatively bonded to Lewis acid sites (PyL) are observed at 1438-1455 (ν_{19b}) and 1600-1632 cm^{-1} (ν_{8a}). The observation of the possible formation of pyridinium ion (PyH^{+}) helps significantly to differentiate the Lewis and Bronsted acid sites. The obvious way to do this would be to observe the band for the N^{+}-H stretching vibration. However, this band is considerably smeared and its frequency lowered by hydrogen bonding [29]; in solid pyridinium chloride, this vibration results in a very broad band at approximately 2450 cm^{-1} [30]. Hence it has been found that studying the changes in the ‘ring’ vibrations of pyridine and other bands in the region of 1700 cm^{-1} to 1400 cm^{-1} reveals adequate information about the acidity of various solids [22].

2.2.3.2b Pyridine adsorption and IR measurements

FT-IR measurements of adsorbed pyridine features on the catalysts were recorded *in situ* in DRIFT mode. The fresh catalysts were activated at 673 K for 3h in a flowing stream of 99.99% UHP N_2 (40 mL/min). The catalysts were then kept at 373 K and 10 µL of pyridine was introduced into the N_2 flow for 10 min. The temperature was ramped under N_2 flow and the spectra were recorded at different temperature up to 673 K. A resolution of 4 cm^{-1} was attained after averaging over 500 scans. The spectra shown in Figure 2.4 were taken as the difference spectra between pyridine adsorbed on the catalyst surface and the activated fresh catalyst.

2.2.3.2c Lewis and Bronsted acidity

The IR spectra of pyridine adsorbed on $Cu_{1-x}Zn_xFe_2O_4$ were recorded between 373 and 673 K. The results from selected compositions, x = 0.05, 0.5 and 1 were given in Figure 2.4. Important pyridine ring modes were observed at 373 K on all the compositions, namely, ν_{8a} (1606) and ν_{19b} (1445 cm^{-1}). In addition, auxiliary bands at 1580 and 1476 cm^{-1} are also observed that appeared to be strong only on x = 0.5 system, whereas on x = 0.05 these bands were very weak. On increasing the temperature from 373 to 473 K, the band at 1478 cm^{-1}

(1580 cm^{-1}) became very strong (vanished) for all the compositions. Another band (which is present only for x = 0.05 at 373 K) at 1550 cm^{-1} appeared on x = 0.5. This band became intense and broad on x = 0.05 and 0.5 with increasing temperature to 573 K, whereas very weak on x = 1. The peak intensity of the main stretching modes ν_{8a} and ν_{19b} remain hardly affected with increasing the temperature. However, slight red shift in ν_{19b} band position is observed for all the compositions. This red shift in band position are 10, 10 and 5 cm^{-1}, respectively for x = 0.05, 0.5 and 1. A red shift for ν_{8a} band, which coupled with 1550 cm^{-1} band, is observed at 573 K only on Cu containing samples, that too significantly on x = 0.5.

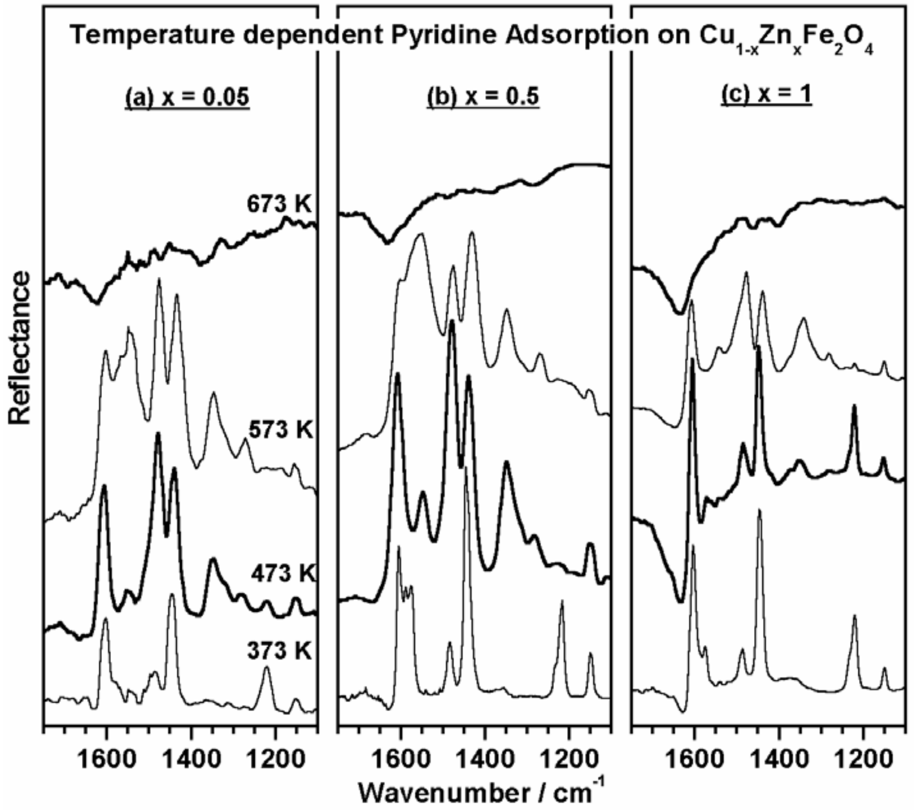

Figure 2.4: Temperature dependent DRIFT spectra of pyridine adsorbed on three selected compositions from $Cu_{1-x}Zn_xFe_2O_4$ (x = 0.05, 0.5 and 1) between 373K and 673K.

Further a new band developed (disappeared) at 1340 cm^{-1} (1220 cm^{-1}) on all the compositions with increasing temperature. No distinct spectral features observed at 673 K indicate pyridine desorbed completely from the catalysts surface between 573 and 673 K. The pyridine molecule interacts on the catalyst surface in the following three modes [31]; (1)

interaction of the N lone pair electron and the H atom of the OH group, (2) transfer of a proton from surface OH group to the pyridine forming a pyridinium ion (Bronsted acidity), and (3) pyridine coordination to an electron deficient metal atom (Lewis acidity). Predominant IR bands, ν_{8a} and ν_{19b}, confirm that the major contribution of acidity is due to Lewis acid sites on all the compositions. Between these two modes of vibrations, ν_{8a} is very sensitive with respect to the oxidation state, coordination symmetry and cationic environment [31]. A broad feature for ν_{8a} band on Cu containing compositions indicates a high extent of disorder on these systems, whereas relatively sharp feature was observed for normal spinel $ZnFe_2O_4$. Upon pyridine adsorption there is electron transfer from pyridine to the spinel surface resulting in the reduction of Cu^{2+} and the extent of reduction increases with temperature [32]. Consequently charge density around Fe^{3+} is also modified and hence the interaction of pyridine on the surface decreases and reflected by the broadening of ν_{8a} band. It is evident from the band at 1550 cm^{-1} that pyridinium ion is formed on all samples due to the proton transfer from the surface -OH groups. This band became very strong and intense at 573 K on Cu containing samples (significantly visible on $x = 0.5$) due to ν_{8a} band broadening. The stretching modes at 1580 and 1475 cm^{-1} are found to be very labile and their stability on the surface is temperature dependent. Further, α-pyridone [33] formation is evident from the observation of 1350 cm^{-1}, and other minor spectral features at high temperature are due to bipyridyl species [34,35] formation due to semiconducting nature of Fe^{3+}.

2.2.3.3 TPD of NH_3 adsorbed on $Cu_{1-x}Zn_xFe_2O_4$

Adsorbed gaseous base (such as NH_3) on strong acid site is strongly chemisorbed and is more difficult to desorb than on a weak acid site. As elevated temperatures stimulate evacuation of the adsorbed bases from acid sites, those at weaker sites will be desorbed preferentially. Thus the proportion of adsorbed base evacuated at various temperatures can give a measure of acid strength [36,37]. Temperature programmed desorption (TPD) of basic molecules such as ammonia, pyridine, n-butylamine, etc. is frequently used to characterize the acid strength as well as the acid amount on a solid surface.

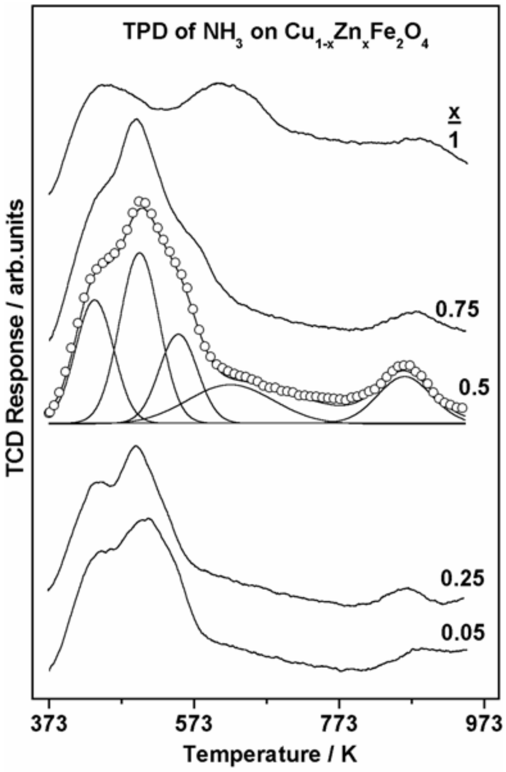

Figure 2.5: Temperature Programmed Desorption profile of NH_3 on $Cu_{1-x}Zn_xFe_2O_4$. Deconvolution was done for data from x = 0.5 composition.

Figure 2.5 shows NH_3 TPD profile from $Cu_{1-x}Zn_xFe_2O_4$, which indicate a broad distribution of binding strength of NH_3 and hence of acid strength of the catalysts. Deconvolution of the profile from x = 0.5 indicates the distribution was divided into five distinct acid sites on Cu containing samples. However, only three distinct sites are observed on $ZnFe_2O_4$.

Among the acid sites found, the one at 436 K (862 K) is weak (strong) whereas other three at 497, 550, and 630 K are moderate strength acid sites on Cu containing samples. This weak site is observed at 444 K with only one moderate acid site at 630 K on $ZnFe_2O_4$. The nature of this acidity is attributed to Lewis type on all the samples as revealed from the results of FT-IR spectroscopy of adsorbed pyridine [38,39]. However, contribution from Bronsted type acidity cannot be ruled out. It is evident from pyridine adsorption FT-IR study that $ZnFe_2O_4$ has very negligible Bronsted type acidity compared to Cu containing samples. NH_3 TPD results have shown two moderate acid sites at 497 and 550 K, present on Cu samples that are absent on $ZnFe_2O_4$. Hence these two moderate acid sites can be ascribed to Bronsted type acidity.

2.2.3.4 XRD, surface area and SEM of alkali promoted MgO

XRD pattern from MgO and alkali metal ions promoted MgO, which were calcined at 673 K for 2h, is shown in Figure 2.6. It is evident that the single phase of MgO periclase (JCPDS files) remains unaffected with alkali metal ions loading. However, the formation of new phases observed that are attributed to alkali metal oxides (Li_2O, K_2O and Cs_2O).The crystallite sizes calculated using Debye-Scherer equation for these samples are given in Table 2.2.

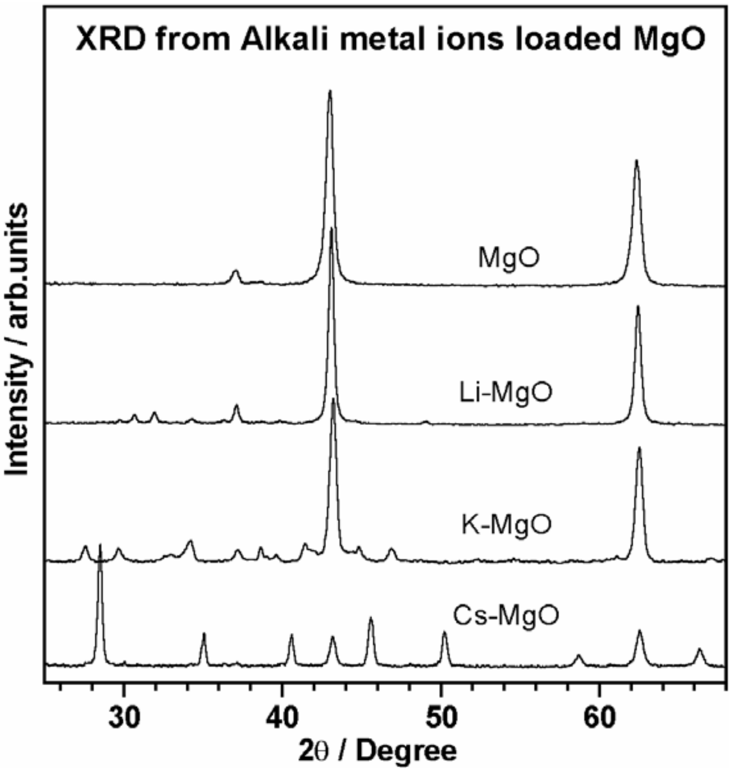

Figure 2.6: XRD pattern from MgO and alkali metal ions promoted MgO and calcined samples at 673 K for 2h.

The fine particle size of MgO is evident from the crystallite size of 10.8 nm that increases with alkali metal ions loading and indicating the fusion of MgO particles with alkali oxides particles. This is more visible with Cs ion loaded MgO, whose XRD pattern is dominated by Cs_2O phase and showing very high crystallite size.

Table 2.2: Crystallites size and surface area of alkali loaded MgO.

Samples	Crystallite Size (nm)	S_{BET} (m^2/g)	Pore Volume (10^{-2}) cc/g
MgO	10.8	60	13
Li-MgO	12.6	49	11
K-MgO	12	28	3
Cs-MgO	19.3	16	1

Table 2.2 shows the surface area and pore volume of MgO and alkali metal ions promoted MgO calculated from N_2 sorption isotherms using BET method. The surface area decreases gradually for alkali metals promoted MgO with increasing size of the alkali metal. This decrease in surface area is attributed to the dissolution of surface MgO by alkali metal oxides during impregnation process. Further, the micropore volume observed for pure MgO also decreases with loading indicates the pore filling with alkali metal oxides.

N_2 adsorption-desorption isotherms are shown in Figure 2.7 for MgO and K-MgO (K loaded MgO). Pure MgO shows a combination of type II and type IV isotherm as evident from the Figure 2.7a. At low values of $P/P_0 < 0.6$ the isotherm is similar to type II for nonporous materials. However, a rapid increase in volume of adsorbed N_2 was observed at higher $P/P_0 > 0.6$ indicating the presence of a type IV isotherm in the sample. This type IV isotherm indicates the presence of small amount of mesoporosity in the pure MgO samples. In contrast, only type II isotherm is observed for K-MgO because of the pore filling by K_2O. There is very small sign or negligible amount of type IV isotherm for K-MgO at $P/P_0 > 0.7$ which is insignificant.

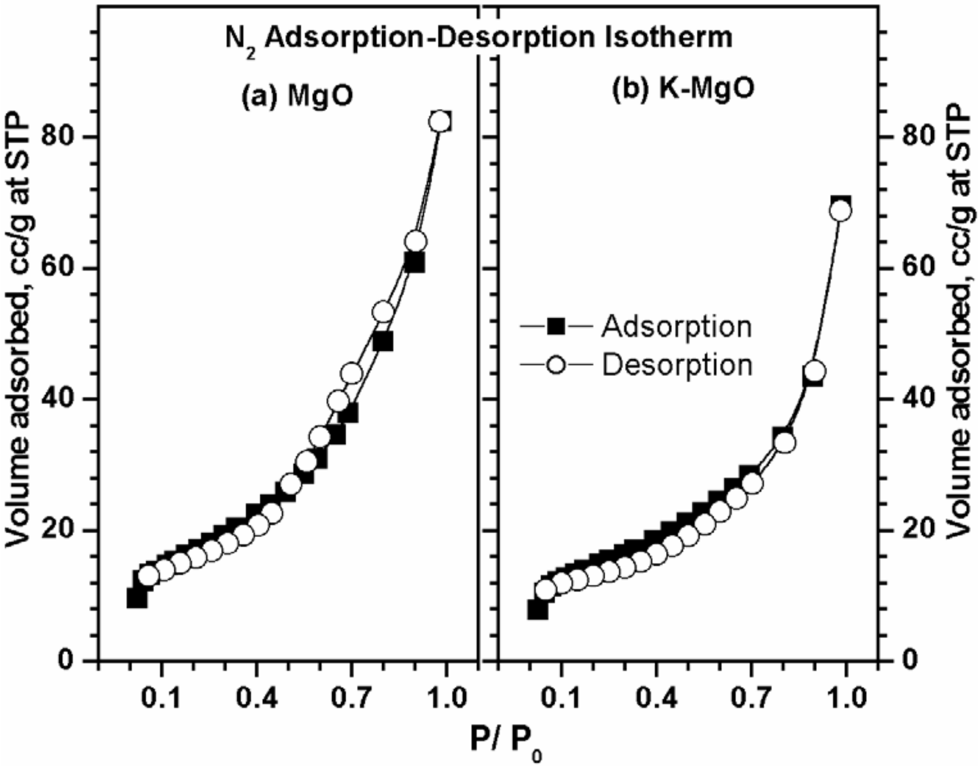

Figure 2.7: N_2 adsorption-desorption isotherm curve obtained from the surface area analysis of MgO and K-MgO at 77 K.

Scanning electron micrographs of MgO and potassium promoted MgO are shown in Figure 2.8, which shows very fine particle size ranging below 100 nm. No significant change in the particle size and the morphology are noted with potassium loading MgO compared to pure MgO. This indicates the size and the morphology of the pure MgO are retained even after potassium loading followed by calcination at 673 K.

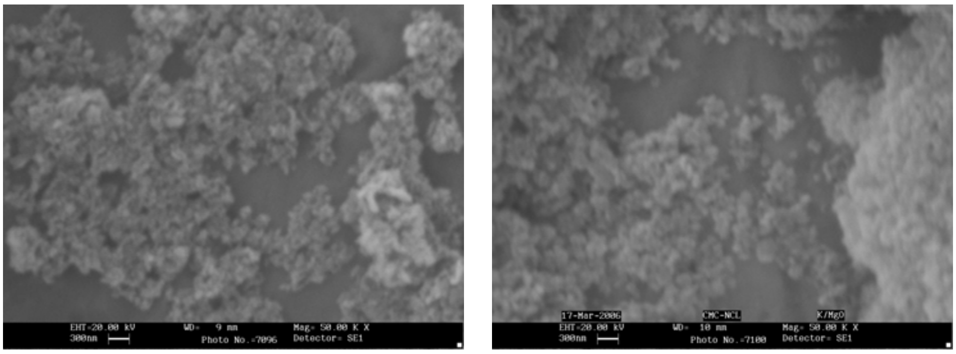

(a) **(b)**

Figure 2.8: Scanning electron micrographs of (a) MgO and (b) K-MgO.

2.3 Conclusions

Two different catalyst systems were prepared and subjected to intense physicochemical characterizations; XRD, Surface area measurements, electron microscopy, FT-IR, and temperature programmed studies were carried out to explore the nature of the materials. Aniline N-methylation catalyst, $Cu_{1-x}Zn_xFe_2O_4$ was prepared by coprecipitation technique followed by calcination at 773 K, resulted in the spinel phase formation that is confirmed from XRD. The metal ion distribution in tetrahedral and octahedral environment is evident from the metal-oxygen bond stretching vibration bands observed in DRIFTS. The fine particle size of these spinels is evident from the scanning electron micrographs. Surface area measurements including BET adsorption-desorption results show they are nonporous materials; however, a small amount of mesoporosity is observed as evident from the type IV isotherm. Lewis acidity dominance on the surface of these ferrospinel catalysts is evident from the temperature dependent pyridine adsorption FT-IR studies. Further, NH_3 TPD studies revealed that the Lewis acidic sites found by pyridine FT-IR is weak to moderate in nature.

Dihydroxybenzene O-methylation catalyst MgO and alkali metal ions promoted MgO were prepared by incipient wet impregnation method and followed by calcination at 673 K. XRD shows that the MgO periclase phase remains unaffected with alkali metal ions loading. An increase in the crystallite size observed for alkali metal ions loaded MgO are due to MgO particles fusion during impregnation process. The decrease in surface area for promoted MgO is due to the alkali metal oxides dissolution on the surface of the MgO. This is well reflected in the N_2 adsorption-desorption isotherm as the alkali metal oxides filled the pores that lead to decrease in the micropore volume compared to pure MgO. The fine particle size of pure and promoted MgO ranging between 50-100 nm is evident from the scanning electron micrographs.

2.4 References

1. P. S. Anilkumar, J. J. Shrotri, S. D. Kulkarni, C. E. Deshpande, S. K. Date, Mater. Lett. 27 (1996) 293.
2. R. Bal. S. Sivasanker, Appl. Catal. A: Gen. 246 (2003) 373.
3. B. D. Cullity, S. R. Stock, Elements of X-ray Diffraction, Prentice Hall, Upper Saddle River, NJ 07458, 3rd ed. 2001.
4. N. F. M. Henry, J. Lipsons, W. A. Wooster, The interpretation of X-ray diffration photographs, Macmillan and Co. Ltd. London, 1951.
5. B. C. Lippens, J. H. de Boer, J. Catal. 4 (1965) 319.
6. E. P. Barret, L. G. Joyner, P. H. Halenda, J. Amer. Chem. Soc. 73 (1951) 373.
7. P. Kubelka, F. Munk, Z. Tech. Phys. 12 (1931) 593.
8. P. Kortum, W. Braun, C. Harzog, Angew. Chem. Int. Ed. Engl. 2 (1963) 333.
9. M. L. Hair, Infrared Spectroscopy in Surface Chemistry, Dekker, New York, 1967.
10. L. H. Little, Infrared Spectroscopy of Adsorbed Species, Academic Press, New York, 1966.
11. W. N. Delgass, D. L. Haller, R. Kellerman, J. H. Lunsford, Spectroscopy in Heterogeneous Catal. Academic Press, New York, 1979.
12. N. W. Hurst, S. J. Gentry, A. Jonese, B. D. McNicol, Catal. Rev. Sci. Eng. 24 (1982) 233.
13. J. L. Falconer, J. A. Schwarz, Catal. Rev. Sci. Eng. 25 (1983) 141.
14. A. Carlson, X-ray Photoelectron Spectroscopy, Dowden, Hutchinson & Ross: Stroudsburg, PA, 1978.
15. Practical Surface Analysis, Vol. 1: Auger and X-ray Photoelectron Spectroscopy, 2nd ed., D. Briggs, M. P. seah, Eds., Wiley, New York, 1990.
16. S. Huffner, Photoelectron Spectroscopy, Springer-Verlag: Berlin, 1995.

17. G. Ertl, H. Knozinger, J. Weitkamp, Handbook of Heterogeneous Catalysis, Vol. 2, Wiley-VCH, Weinheim, 1997, p.538.
18. M. Pruski, X. wu, M. N. Smale, B. C. Gerstein, T. S. King, Catalyst Deactivation, Elsevier, Amsterdam, The Netherlands, 1991, Chapter 14.
19. F. Diez, B. C. Gates, J. T. Miller, D. J. Sajkowski, S. G. Kukes, Ind. Eng. Chem. Res. 29 (1990) 1999.
20. T. Mathew, N. R. Shiju, K. Sreekumar, B. S. Rao, C. S. Gopinath, J. Catal. 210 (2002) 405.
21. R. D. Waldron, Phys. Rev. 99 (1955) 1727.
22. E. P. Parry, J. Catal. 2 (1963) 371.
23. J. A. Lercher, C. Grundling, G. Eder-Mirth, Catal. Today, 27 (1996) 353.
24. J. A. Pieterse, S. V. Reyes, K. Seshan, L. Domokos, J. A. Lercher, J. Catal. 187 (1999) 518.
25. B. Wichterlova, N. Ilkova, E. Uvarova, J. Ejka, P. Sarv, C. Paganini, J. A. Lercher, Appl. Catal. A Gen. 182 (1999) 297.
26. V. A. Veefkind, M. L. Smidt, J. A. Lercher, Appl. Catal. A Gen. 194 (2000) 319.
27. H. Knozinger, Adv. Catal. 25 (1976) 184.
28. M. C. Kung, H. H. Kung, Catal. Rev. Sci. Eng. 27 (1985) 425.
29. R. F. Evans, W. Kynaston, J. Chem. Soc. (1962) 1005.
30. R. C. Lord, R. E. Merrifield. J. Chem. Phys. 21 (1953) 166.
31. G. Busca, Catal. Today, 41 (1998) 191.
32. T. Mathew, B. B. Tope, N. R. Shiju, S. G. Hegde, B. S. Rao, C.S. Gopinath, Phys. Chem. Chem. Phys. 4 (2002) 4260.
33. H. Knozinger, H. Krietenbrink, H. D. Muller, W. Schulz, Proceedings of Sixth International Congress on Catalysis, 1977, Vol. 1, p. 183.

34. G. Busca, V. Lorenzelli, Mater. Chem. 6 (1981) 175.

35. P. G. Harrison, E. W. Thornton, J. Chem. Soc. Faraday Trans. 71 (1975) 1013.

36. K. Tanabe, M. Misono, Y. Ono, H. Hattori, Stud. Surf. Sci. Catal. 51 (1989).

37. J. A. Lercher, G. Ritter, H. Vinek, J. Colloid. Inter. Sci. 106 (1985) 215.

38. S. Rajagopal, T. L. Grimm, D. J. Collins, R. Miranda, J. Catal. 137 (1992) 453.

39. M. M. Khader, J. Mol. Catal. A 104 (1995) 87.

Chapter 3: N-methylation of aniline and aniline substrates on $Cu_{1x}Zn_xFe_2O_4$

3.1 Introduction

There is a selectivity issue in synthesizing selectively N-methylaniline over N,N-dimethylaniline with methanol as methylating agent. In general, solid acid-base catalysts, based on oxides [1,2], zeolites [3-8], alumina [9] etc., are not successful in controlling the conversion of N-methyl to N,N-dimethyl aniline and it is mainly controlled by process conditions [9,10]. Infact, very few patents [11-14] are available for the selective synthesis of N-methylaniline, in which DMA forms in sizeable to large amounts (20-90% selectivity). Selva *et al.* [8] reported selective N-methylation of aromatic amines using alkali metal ions exchanged faujasites under batch conditions below 473 K, with DMC (dimethylcarbonate) as solvent cum methylating agent. Very high amines conversion (> 90%) were reported with quite excess of DMC. However, for industrial scale it is economical to use methanol as methylating agent, which can be activated above 473 K on such catalysts. Ko *et al.* [9] studied the methylation of aniline with methanol at 698 K over alumina produces both NMA and DMA and the corresponding apparent activation energies are 62.7±2.1 and 48.3±2.9 $KJmol^{-1}$, respectively, suggests NMA reacts faster than aniline and undergoes consecutive methylation to DMA that leads to poor product selectivity or highly selective DMA production.

Ferrospinels are active and selective catalysts for alkylation of aromatic compounds. Sreekumar and Thomas *et al.* demonstrated that Ni, Co and Zn based ferrospinel catalysts were active for aniline and phenol methylation reaction [15-20]. Hence it is worth investigating these ferrospinels for aniline N-methylation using methanol as methylating agent. A thorough search for the selective catalytic production of N-methylaniline was carried out with $A_{0.5}A'_{0.5}Fe_2O_4$ systems, where A = Fe, Cu, Zn and A' = Fe, Co, Ni, Cu and

Zn. Promising N-methylation activity was observed only with Cu and Zn based ferrospinel. Thus $Cu_{1-x}Zn_xFe_2O_4$ where x = 0.05, 0.25, 0.5, 0.75 and 1 was pursued for serious activity measurements. Detailed catalytic activity studies show that Cu^{2+} is largely responsible for methylation and Zn^{2+} enhances the stability of the system, while $ZnFe_2O_4$ does not display any significant activity towards methylation on its own. Among the compositions examined, x = 0.5 shows the selective mono N-methylation activity atleast upto 100 h, under optimum reaction conditions indicating that on $Cu_{0.5}Zn_{0.5}Fe_2O_4$ system N-monomethylation activity sustains without any significant change in selectivity and overall activity.

Further, this high performance $Cu_{0.5}Zn_{0.5}Fe_2O_4$ system was employed for N-monomethylation of substituted anilines (*o*-, *m*- and *p*-toluidines, 2,6-xylidine, p-anisidine and p-aminoacetophenone) at optimum reaction conditions that were applied for aniline methylation. However, few reactions were also carried out on x = 0.05 and 0.75 compositions for comparison purpose. Although anilines conversion decreases with increasing substrate size, N-monomethylated products selectivity remains high, despite the presence of ring-directing group. Electronic effects (+I and –I or +R and -R) due to different groups in the above aniline substrates marginally influence the reactivity of the substrates. The perpendicular orientation of toluidine substrates on catalyst surface influences the conversion and N-methyltoluidine yield. Increased crowding at ortho position restricts the substrates interaction with the catalyst surface and 2,6-xylidine shows no reactivity.

3.2 Experimental

Vapor phase experiments were performed at atmospheric pressure in a fixed bed, vertical, down-flow, integral glass reactor placed inside a double-zone furnace (Geomechanique, France). Fresh catalyst was charged each time at the center of the reactor in such a way that the catalyst was sandwiched between the layers of inert porcelain beads and glass wool. The upper portion of the reactor served as a vaporizer cum pre-heater. All heating and temperature measurements were carried out using ‘Aplab’ temperature controller and indicator instruments. A K-type thermocouple was positioned at the center of the catalyst bed to monitor the exact temperature of the catalyst. The reactant mixture was fed into the reactor using a syringe pump (Braun, Germany) at a desired flow rate. Reaction products were collected from a condenser fixed below the reactor and circulated with cold water. Products were analyzed using gas chromatography (Agilent Model 19091J-413) with a HP-5.5% phenyl methyl siloxane capillary column equipped with a flame ionization detector and/or gas chromatography-mass spectroscopy (Shimadzu GC-17A equipped with a QP 5000 Mass spectrometer).

Aniline N-methylation was carried out using 0.75 g of calcined $Cu_{1-x}Zn_xFe_2O_4$ with particle size between 10-20 mesh. The fresh catalyst was activated in a sufficient flow of dry air at 773 K for 6 hours before the reaction and then brought to the desired reaction temperature with a stream of N_2 (10 mL/min). The reactant mixture (methanol + aniline + water) was fed using a syringe pump without any carrier gas. Analytical grade aniline and methanol from Merck were used in the present study.

The reproducibility for different samples was checked experimentally, and the measurements were reported two or three times with a relative error of approximately ± 2% for high conversion/selectivity measurements and ± 5% for low conversion/selectivity measurements. The thermal process without catalysts was negligible in all the cases. It is evident from the following discussions that several factors contribute to the total catalytic activity at different extents. Besides, the difficulty in determining the specific surface area of any specific element and the complex nature of active centers in these materials makes it unreliable to express the results in turn over frequency. Hence the results are given in weight percentage.

3.3 Aniline N-methylation

3.3.1 Results

3.3.1.1 Effect of various metal ions towards selective mono-N-methylation

Figure 3.1 shows aniline conversion and NMA yield on $A_{0.5}A'_{0.5}Fe_2O_4$ (A = Fe, Zn, Cu and A' = Fe, Co, Ni, Cu and Zn) at 573 K with 3:1 ratio of CH_3OH: $PhNH_2$. NMA formed selectively on all the systems; however, aniline conversion declines on all the systems with TOS due to catalyst deactivation and/or coke deposition.

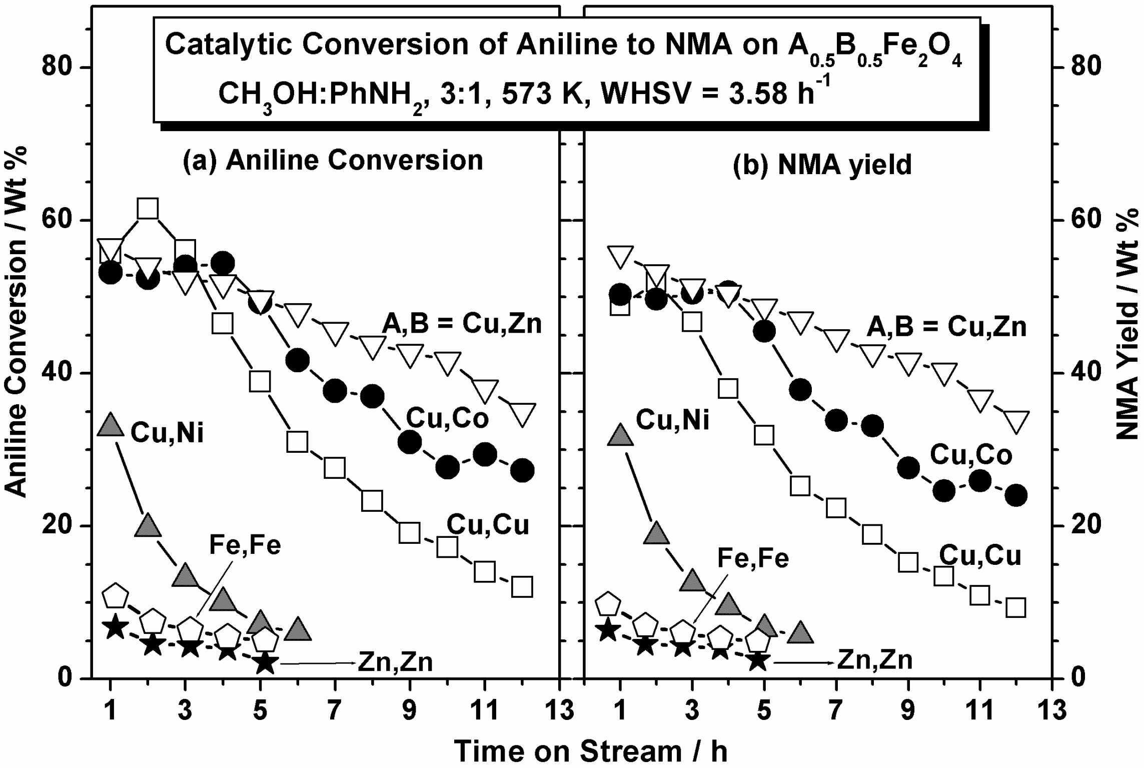

Figure 3.1: Aniline conversion and N-methylaniline yield obtained on $A_{0.5}A'_{0.5}Fe_2O_4$ (A = Fe, Zn, Cu and A' = Fe, Co, Ni, Cu and Zn) at 573 K with 3:1 ratio of CH_3OH:$PhNH_2$ at space velocity 3.58 h^{-1}. Note a better initial catalytic activity was observed when Cu occupies the A-site in ferrites and the stability increases considerably when Zn also occupies the same site.

Initial high aniline conversion to NMA associated with Cu-containing ferrospinels indicates that Cu is largely responsible for selective catalytic methylation activity. Addition of other metal ions to Cu, such as Co and Zn, improves the stability of the systems; however, the Ni addition decreases the activity. It is interesting to note that $Cu_{0.5}Zn_{0.5}Fe_2O_4$ shows a stable and better activity than all other systems that were screened.

This indicates that Zn plays an important role on the stability of the system, although negligible activity is found on $ZnFe_2O_4$.

Individual oxides, such as, CuO, ZnO, CoO, Fe_2O_3 and CuO-ZnO have also been tested and shows negligible or no activity towards aniline methylation. A combination of Cu, Zn and Fe in $Cu_{1-x}Zn_xFe_2O_4$ shows a high and stable activity for aniline N-methylation and this indicates that a suitable multi-component system is essential. Due to above reasons $Cu_{1-x}Zn_xFe_2O_4$ system was chosen for the detailed catalytic and characterization studies.

3.3.1.2 Effect of methanol to aniline molar ratio

The optimum composition of reactants was found out by carrying out aniline methylation using $CH_3OH:PhNH_2:H_2O$ molar ratios between 2:1:1 and 5:1:1 on $Cu_{0.5}Zn_{0.5}Fe_2O_4$ at 573 K (Figure 3.2). It is to be noted that there is no water added to the feed in the results shown in Figure 3.1 and the results shown in the figures henceforth are considerably different due to the addition of water. It is well known that addition of water improves the stability of the catalytic system by avoiding coke deposition through water-gas shift reaction.

Aniline conversion increases gradually with increasing methanol molar ratio up to 5, however, NMA selectivity decreases from 99% to 77%. This shows a linear increase in aniline conversion, (NMA selectivity) is directly (inversely) proportional to the amount of methanol in the feed. As the reaction was performed in vapor phase conditions, some amount of methanol will decompose due to unavoidable side reactions, such as, steam reforming of methanol (SRM) and simple gasification. Hence an excess amount of methanol is necessary, even though the reaction stoichiometry suggests a $CH_3OH:PhNH_2$ molar ratio of 1:1. Optimum feed composition was fixed at 3:1:1, where a maximum aniline conversion with high NMA selectivity was observed. However, it is evident from our *in situ* FT-IR results

(Chapter 4) that the reaction stoichiometry is well obeyed on catalyst surface at 473 K during NMA formation.

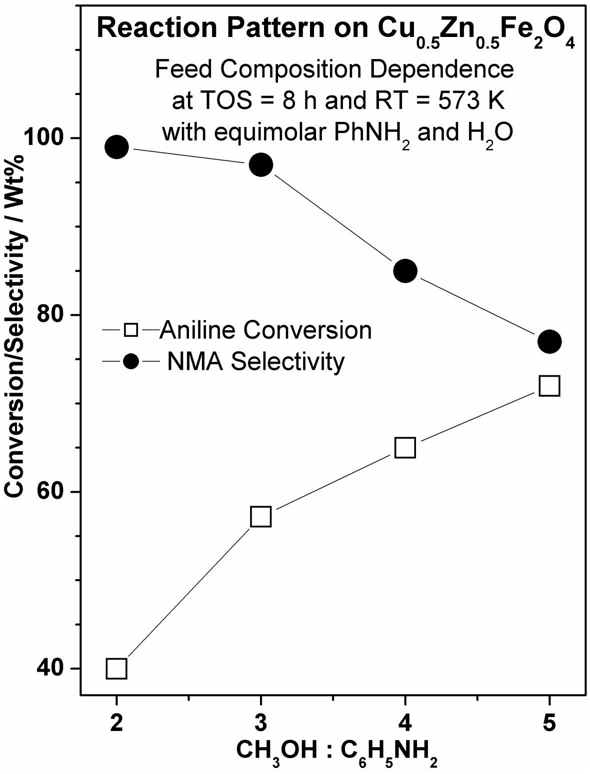

Figure 3.2: Methanol:aniline:water feed composition (between 2:1:1 and 5:1:1) dependence of $PhNH_2$ conversion and NMA selectivity on $Cu_{0.5}Zn_{0.5}Fe_2O_4$ at 573 K and TOS = 8h. 1:1 aniline:water ratio is maintained in all the feed compositions employed.

3.3.1.3 Effect of $Cu_{1-x}Zn_xFe_2O_4$ catalyst composition

Figure 3.3 shows the aniline conversion (a) and NMA yield (b) on $Cu_{1-x}Zn_xFe_2O_4$ (x = 0.05, 0.25, 0.5, 0.75 and 1) at T = 573 K, WHSV = 3.58 h^{-1} with 3:1:1, molar ratio of $CH_3OH:PhNH_2:H_2O$. Activity studies have been carried out without water in the feed and a specific result on x = 0.5 is included to show the effect of addition of water. It is to be noted that samples with x = 0.05 and 0.25 show initially high aniline conversion, which decreases fast with increasing TOS. x = 0.5 shows a stable activity and indeed there is a marginal increase in activity at TOS higher than 6 h. The activity loss in the absence of water is mainly due to coke deposition. This is further confirmed by thermogravimetric analysis of deactivated samples in air atmosphere. $ZnFe_2O_4$ shows the lowest activity compared to any other compositions indicating the direct methylation role on Zn and Fe is negligible. Nevertheless, catalyst stability associated with x = 0.5 under reaction conditions seems enhanced, likely, due to the presence of an optimum amount of Zn in it. The same is reflected in the extended activity measurement for 100 hrs (vide infra, Figure 3.5).

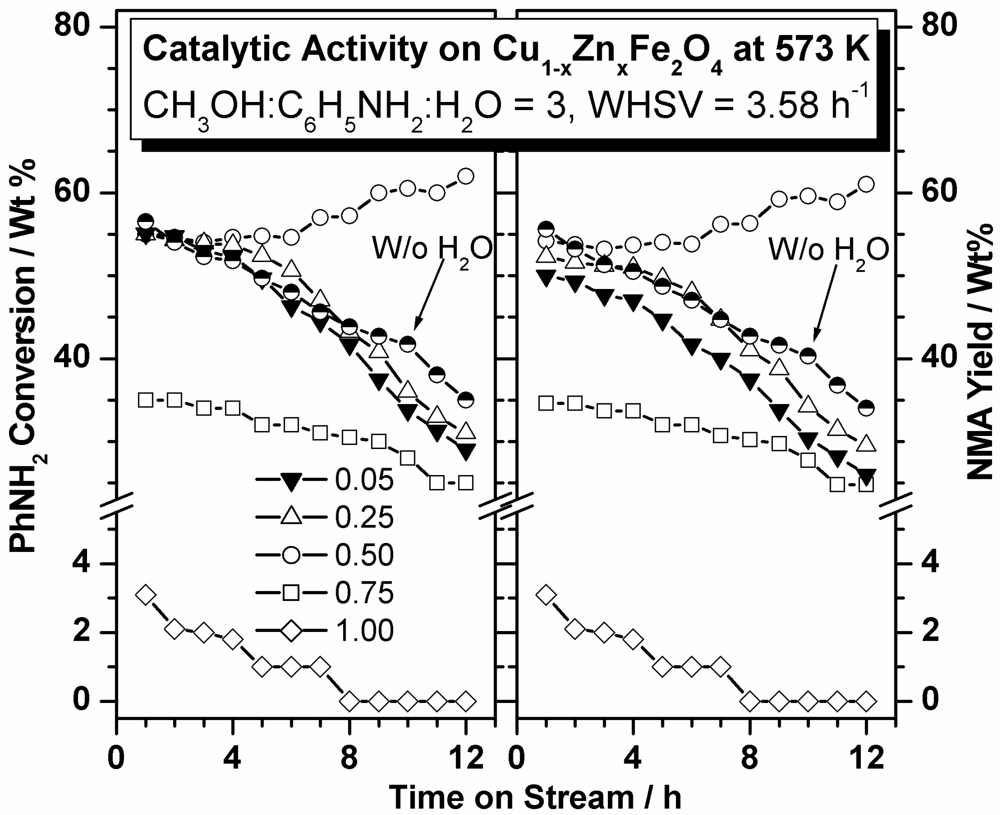

Figure 3.3: TOS dependence of aniline conversion and NMA yield on $Cu_{1-x}Zn_xFe_2O_4$ at 573 K and WHSV = 3.58 h^{-1} with a feed composition of 3:1:1 of MeOH:$PhNH_2$:H_2O. Feed without water was also employed for x = 0.5 composition and denoted by half-filled circles. Note the very poor activity with x = 1 and maximum activity with x = 0.5.

3.3.1.4 Effect of reaction temperature and catalyst composition

Temperature dependent catalytic activity measurements obtained at TOS = 8 h are shown in Figure 3.4. It is clear that the maximum aniline conversion is at 573 K on all Cu containing compositions with a volcano type activity pattern with temperature. NMA selectivity remains >90% on all the catalyst compositions, however it decreases with increasing temperature. Between 543 and 633 K, x = 0.5 shows maximum aniline conversion with >93% NMA selectivity and stable activity. This indicates an equal amount of Cu and Zn is critical for the effective mono-N-methylation of aniline. A small amount of *o*-toluidine (OT) is formed along with DMA at high reaction temperatures (≥ 603K) on Cu rich compositions.

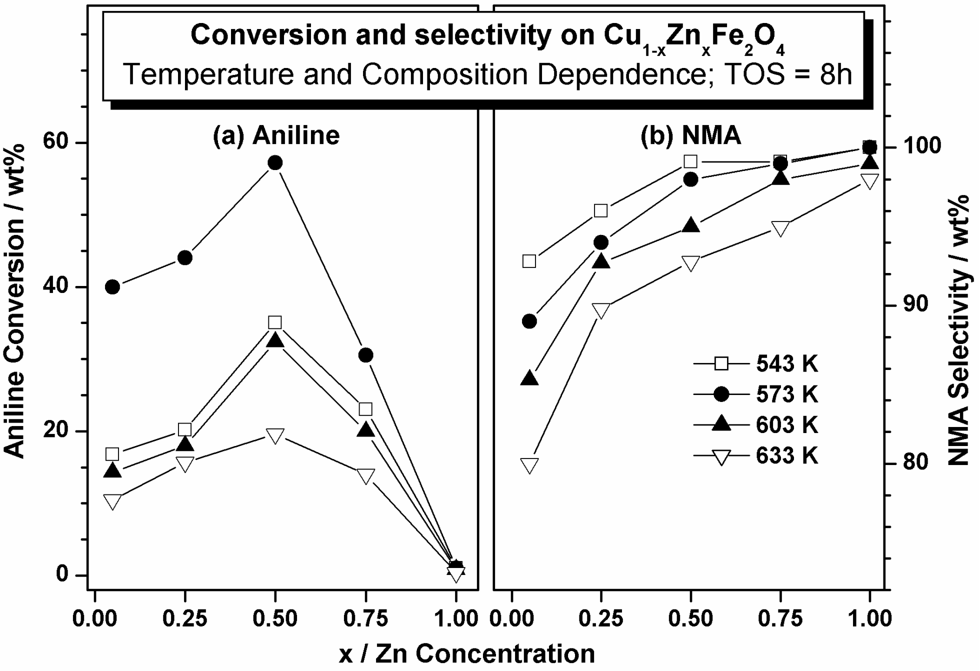

Figure 3.4: $PhNH_2$ conversion and NMA selectivity dependence on reaction temperature and $Cu_{1-x}Zn_xFe_2O_4$ compositions at TOS = 8h and WHSV = 3.58 h^{-1} with 3:1:1, $CH_3OH:PhNH_2:H_2O$.

Indeed the maximum catalytic activity observed at 573 K was further confirmed by measuring the reaction at two different temperatures on $Cu_{0.5}Zn_{0.5}Fe_2O_4$ consecutively with continuous feed flow. The reaction was first carried out at 633 K for 4h TOS and then temperature was brought down to 573 K without taking off the feed and then reaction was carried out at 573 K for another 4h TOS. Aniline conversion and product selectivity are shown in Figure 3.5. The above reaction carried out at 573 K in the second step, indeed, shows an increase in aniline conversion (46%) compared to 20% aniline conversion at 633 K. However, a marginal decrease in aniline conversion in the second step (above) compared to 54% conversion in the reaction carried out directly at 573 K (Figure 3.3) hints a slow change in catalyst surface properties at high temperature (633 K), which is due to small amount of SRM and/or decomposition of methanol.

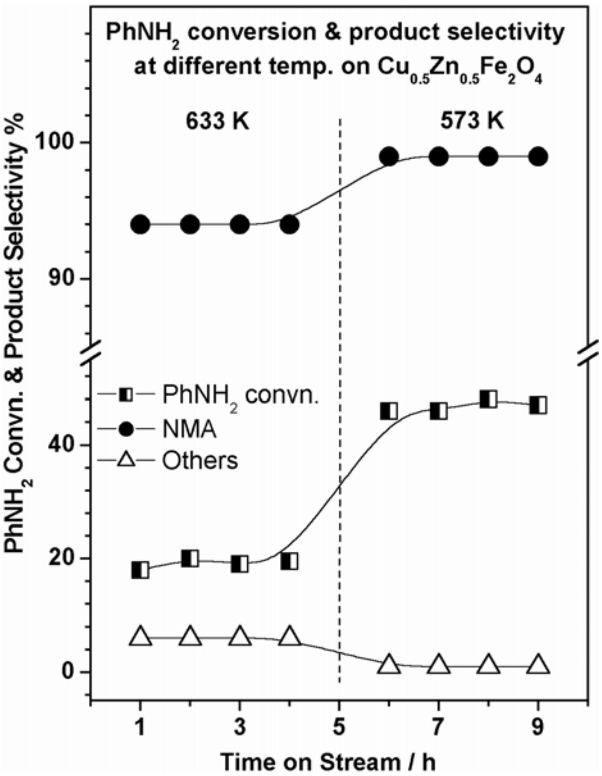

Figure 3.5: Aniline conversion and product selectivity at two different temperatures on $Cu_{0.5}Zn_{0.5}Fe_2O_4$. Note the reaction was carried out in a continuous feed flow.

3.3.1.5 Effect of WHSV or contact time and TOS stability

Figure 3.6 shows the aniline conversion and NMA selectivity on $Cu_{0.5}Zn_{0.5}Fe_2O_4$ at optimized reaction conditions measured up to 100 hrs. The inset displays the weight hour space velocity (WHSV) dependence at TOS = 8 h for conversion and products selectivity. Figure 3.6 demonstrates that the aniline conversion decreases with increasing WHSV. However, DMA formation becomes considerable at lower WHSV (or higher contact time), which indicates a longer residence time of NMA on catalyst surface that leads to consecutive methylation and hence declining NMA selectivity. Similarly, small amount of OT formed only at the lowest WHSV value employed, suggests that it is likely due to the isomerization of NMA.

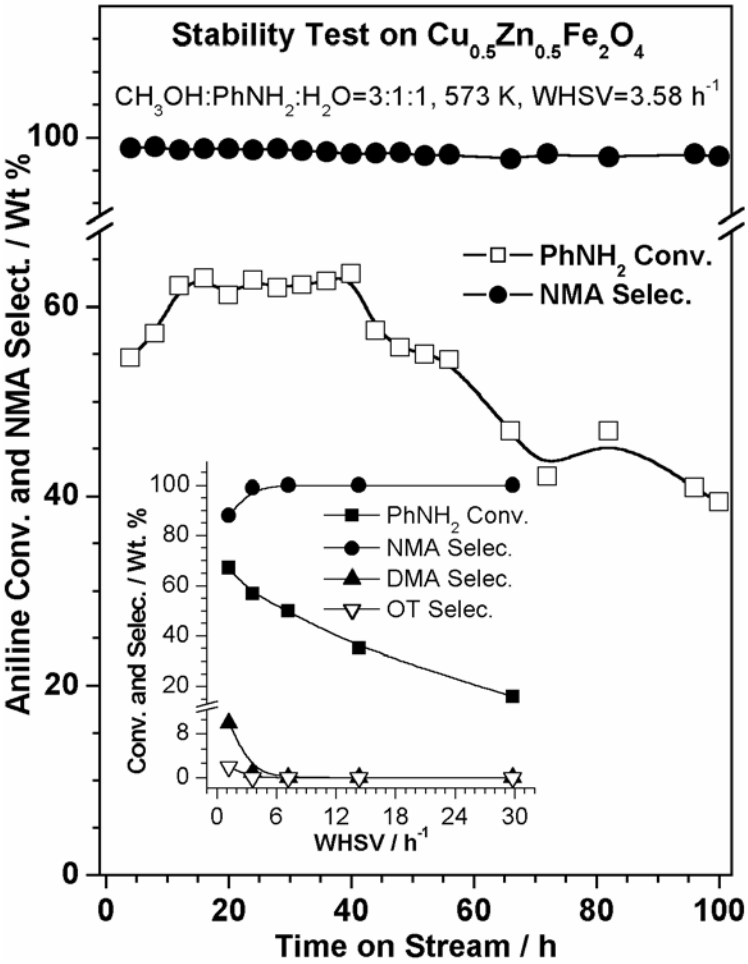

Figure 3.6: Time on stream and weight hour space velocity (inset) dependence of aniline conversion and NMA selectivity on $Cu_{0.5}Zn_{0.5}Fe_2O_4$ at 573 K, with 3:1:1, $CH_3OH:PhNH_2:H_2O$, WHSV = 3.58 h^{-1}. Note the formation of secondary products at low WHSV.

At higher WHSV, NMA forms exclusively and selectively although aniline conversion was poor. An optimum of 58% aniline conversion with nearly 98% NMA selectivity was achieved at WHSV = 3.58 h^{-1} (or contact time = 0.28h). This above optimized WHSV was fixed for all further studies in this chapter.

3.3.2 Discussion

Systematic investigations on aniline methylation using $A_{0.5}A'_{0.5}Fe_2O_4$ lead to selective NMA formation on $Cu_{1-x}Zn_xFe_2O_4$. Aniline N-methylation with methanol leads selectively (>96%) to NMA on $Cu_{0.5}Zn_{0.5}Fe_2O_4$ catalyst with stable activity under optimized reaction conditions. A facile NMA formation from perpendicularly oriented aniline on the above composition (Chapter 4) indicates that $Cu_{0.5}Zn_{0.5}Fe_2O_4$ is a promising catalyst system for this reaction, although the maximum aniline conversion is between 60 and 65% and worth pursuing. However, aniline conversion and/or NMA selectivity decreases on moving either side of the above optimum conditions, in terms of high/low reaction temperatures, WHSV and catalyst compositions. It is evident that DMA forms at the expense of NMA at high reaction temperatures and high contact times. This indicates a sequential methylation mechanism and dimethylation rate increases considerably with temperature. In addition, catalysts deactivate faster with TOS at higher temperatures and this is mainly due to SRM that reduces the active Cu^{2+} to Cu^0.

Very low aniline conversion observed on $x = 1$ is mostly due to a poor interaction among the reactants on the catalyst surface and it is clearly shown in FT-IR results in Chapter 4. In contrast, samples with $x = 0.05$ and 0.25 deactivate faster and it is due to larger degree of SRM to H_2 that reduces Cu^{2+} active species to Cu^0, whereas on increasing Zn ($x \geq 0.5$) concentration Cu^{2+} reduction is highly avoided as evident from the Cu 2p core level XPS (Chapter 5). Introduction of Zn into the $CuFe_2O_4$ systems enhances the catalyst lifetime. In contrast, introduction of Cu into the $ZnFe_2O_4$ displays an increase in aniline conversion, up to two orders of magnitude. This demonstrates that the active site for methylation is indeed Cu^{2+}; however, Zn addition improves the catalyst stability even though Zn does not exhibit significant activity.

Aniline conversion and NMA selectivity vary quite considerably and they depend on the ratio of methanol:aniline in the feed (Figure 3.2). Mixed metal oxide catalysts such as $CuO-Fe_2O_3$, $ZnO-Fe_2O_3$ [21] and $CuO-ZnO-Al_2O_3$ [22] are well known for methanol gasification reactions and support these findings that an excess amount of methanol is necessary in the feed. An optimum methanol to aniline ratio of 3 is required to operate for high NMA selectivity with intermediate aniline conversion with lowest extent of methanol gasification reaction.

Temperature influences the methylation kinetics to a large extent; an appreciable increase in aniline conversion was observed on increasing the temperature from 543 K to 573 K with a negligible decrease in NMA selectivity (Figure 3.4). A further increase in temperature affects the NMA selectivity due to the formation of DMA and OT with a notable drop in aniline conversion. There are few reasons for the above change in catalytic activity at high temperatures. FT-IR studies clearly showed that the aniline desorbs around 573 K (Chapter 4) and partly that is the reason for low aniline conversion at above 573 K. Almost the same catalytic activity was resumed at 573 K after carrying out the reaction at 633 K, indeed hints high aniline desorption at high temperature plays a significant role in aniline conversion. A large extent of inevitable methanol gasification/SRM at high temperature leads to poor methanol availability and hence low NMA yield. General observation of reduced metal ions on the spent catalyst reveals that the overall reaction takes place under moderate to marginal reduction conditions, depending on the copper content. It is obvious that SRM or MeOH gasification/decomposition is highly plausible at high temperatures and the role of the present Lewis acid catalyst is to suppress the above reaction. It is clear that Zn suppresses these reactions on $Cu_{1-x}Zn_xFe_2O_4$ and the same is clearly indicated from the general decrease in carbon content with increasing Zn content.

3.4 Substituted anilines N-methylation

3.4.1 Results and Discussion

3.4.1.1 Effect of catalyst composition

Effect of catalyst composition on selected compositions (x = 0.05, 0.5 and 0.75) of $Cu_{1-x}Zn_xFe_2O_4$ for N-methylation of substituted anilines is given in Figure 3.7. *o*-toluidine (OT), *m*-toluidine (MT), *p*-toluidine (PT), *p*-anisidine (PA), *p*-aminoacetophenone (PAA) and

2,6-xylidine (Xyl) conversion and N-methyl anilines yield were clearly high on $Cu_{0.5}Zn_{0.5}Fe_2O_4$ system, whereas low on x = 0.05 and 0.75 systems. However, N-methyl anilines selectivity on all the compositions was >95% (except in case of PAA) and only traces of N, N-dimethylated and C-methylated products were observed. Cu rich system (x = 0.95) shows large amount of Cu^{2+} reduction to Cu^{0} under reaction conditions like aniline methylation, due to methanol decomposition to reformate products. Hence, the initial TOS anilines conversion on this catalyst composition decreases with increasing TOS.

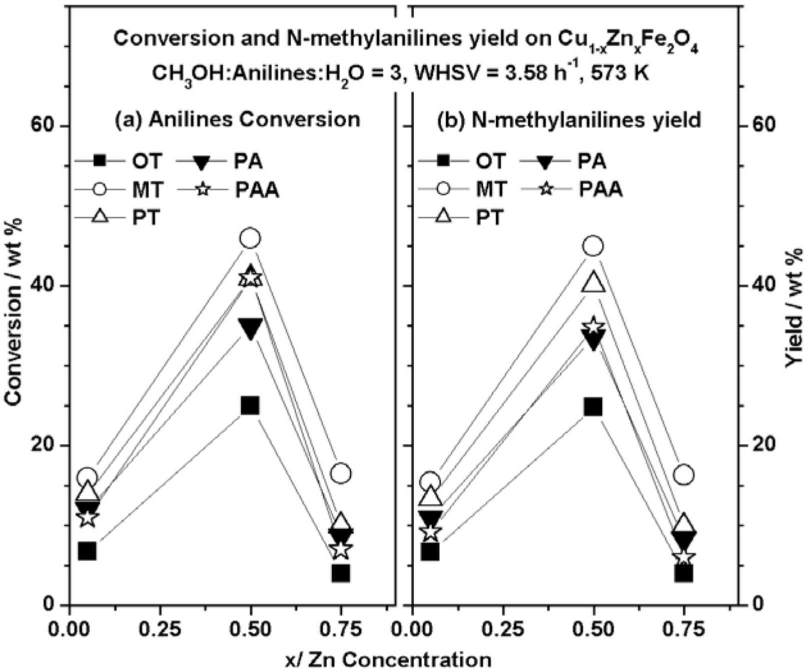

Figure 3.7: Substituted anilines conversion and N-methylanilines yield on selected compositions of $Cu_{1-x}Zn_xFe_2O_4$ at 573 K and WHSV = 3.58 h^{-1}· Conversion and yield data plotted were obtained at TOS = 10 h. Note that N,N –dimethylated and C-methylated anilines were obtained in trace amount with all aniline substrates.

On the other hand, Zn plays no direct role on aniline methylation and hence poor activity on Zn rich system, x = 0.75 (and x = 1) (Figure 3.3). Interestingly, x = 0.5 having 1:1 Cu and Zn shows promising catalytic activity towards N-monomethylation of substituted anilines. Cu^{2+} acts as active methylation center, whereas Zn acts as "active spacer" and maximizes the dispersion of the active Cu^{2+} (Chapter 5). In addition, Zn being methoxy species stabilizer might impede the steam reforming of methanol in the presence of aniline there by preventing Cu^{2+} reduction during reaction conditions. Due to the above observations, further detailed studies on N-methylation of various aniline substrates were carried out only on $Cu_{0.5}Zn_{0.5}Fe_2O_4$.

3.4.1.2 N-methylation of aniline substrates on $Cu_{0.5}Zn_{0.5}Fe_2O_4$

Figure 3.8 shows N-methylation of OT, MT, PT, PA, PAA and Xyl with methanol on $Cu_{0.5}Zn_{0.5}Fe_2O_4$ as a function of TOS. Excess methanol (methanol: PAA:H_2O = 6:1:1) was employed to avoid PAA solubility problem. A feed composition of 3:1:1 (methanol:aniline:H_2O) was employed for all other anilines. Anilines conversion increases in the following order Xyl<OT<PT~PA<MT<PAA.

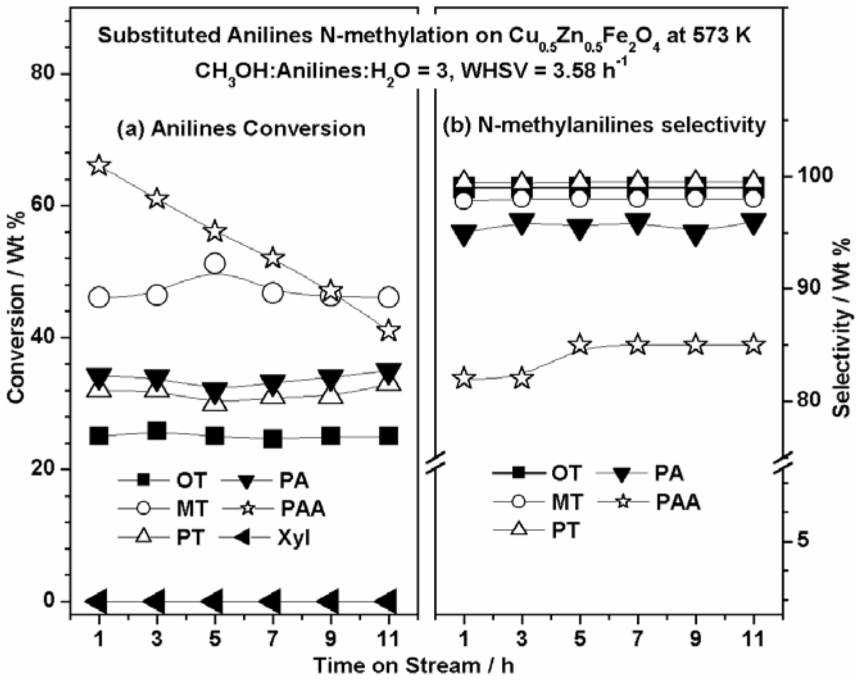

Figure 3.8: Substituted anilines conversion and N-methylation selectivity on $Cu_{0.5}Zn_{0.5}Fe_2O_4$. In the case of PAA, feed with CH_3OH:PAA:H_2O = 6 was taken to avoid solubility problem. Since an excess methanol was used in the feed significant amount of N,N-dimethyl-p-aminoacetophenone was formed and hence N-methyl-p-aminoacetophenone selectivity decreased.

In general, N-methylated products selectivity remains >95% with all the substrates except PAA, which shows about 85% selectivity, in spite of the presence of ring-directing groups that can exert electronic effect into the aromatic ring. No significant reaction occurs with xylidine. The well known inductive effects on aromatic compounds by substituents in which carbon, nitrogen, oxygen and halogen atoms (more electronegative than hydrogen) form sigma-bonds to the aromatic ring exert an inductive electron withdrawal (-I) or donation (+I) from and to the aromatic ring, which perturbs the reactivity of aromatic substrates [23]. Similarly resonance effect on the aromatic ring due to presence of electronegative (-R) or electropositive (+R) groups like nitro, acetyl, methoxy etc will also influence the reactivity of the aromatic substrates [23].

Catalytic conversion of substituted anilines (MT and PAA) was observed to be comparable to aniline under optimized reaction conditions at 573 K (Figure 3.1). However, other substituted anilines (OT, PT and PA) are significantly less reactive than aniline. PT, PA and PAA having different electronic effects +I, +R and -R, respectively at phenyl ring show similar reactivity. This indicates a very small or negligible electronic effect due to the presence of substituents. It is evident from the *in situ* FTIR studies (Chapter 4) that aniline interacts with the catalyst surface through N-atom and phenyl ring orientation is perpendicular to the catalyst surface during methylation. It is expected that substitution at ortho position in the phenyl ring hinder anilines from interacting with the catalyst surface due to large steric hindrance. This is supported from the low conversion observed with OT and hardly any reaction takes place with 2, 6-xylidine. This also demonstrates that the degree of interaction of di-ortho substituted anilines with the catalyst surface decreases with increasing steric factor and the approach of methyl species to amino group is severely restricted.

In the case of PAA, -R effect is expected to influence the reactivity. PAA conversion observed was maximum (66%); however, the reactant mixture contains excess methanol (Methanol:PAA = 6). N-methyl-*p*-aminoacetophenone (NMPAA) selectivity is 85% since N,N-dimethyl-*p*-aminoacetophenone formed in significant amount. PAA conversion decreases with increasing TOS might be likely due to decomposition of extra methanol to reformate products and that reduces the active Cu^{2+} species.

3.4.1.3 Effect of reaction temperature

Effect of reaction temperatures on N-methylation of substituted anilines on $Cu_{0.5}Zn_{0.5}Fe_2O_4$ is given in Figures 3.9 and 3.10. Anilines conversion and N-methylated products yield increased significantly on increasing the reaction temperature from 543 to 573 K for all the aniline substrates, OT, MT, PT, PA and PAA. Selectivity for N-methylanilines remains ≥95% except in the case of PAA. However, at high temperature (603 K), substrate conversion decreases and this is mainly due to the fact that methanol in the feed decomposes excessively to reformate products that lead to unavailability of the methyl group for effective N-methylation of aniline substrates. Further, small but significant increase in the amount of C-methylated products was observed at 603 K.

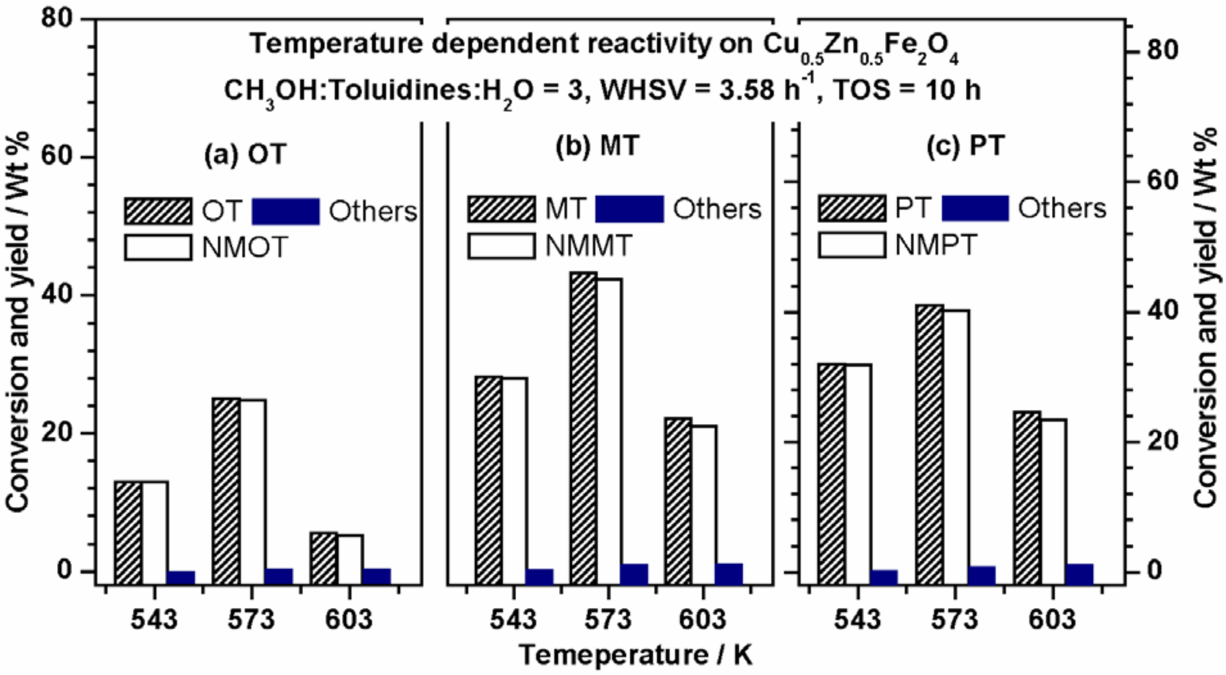

Figure 3.9: Temperature dependent study on toluidines conversion and N-methyltoluidines yield on $Cu_{0.5}Zn_{0.5}Fe_2O_4$ under optimized reaction conditions between 543-603 K at TOS = 10h. NMOT, NMMT and NMPT are N-methyl-o-toluidine, N-methyl-m-toluidine and N-methyl-p-toluidine, respectively. Other products, N,N-dimethylated and C-methylated anilines were obtained in trace quantity.

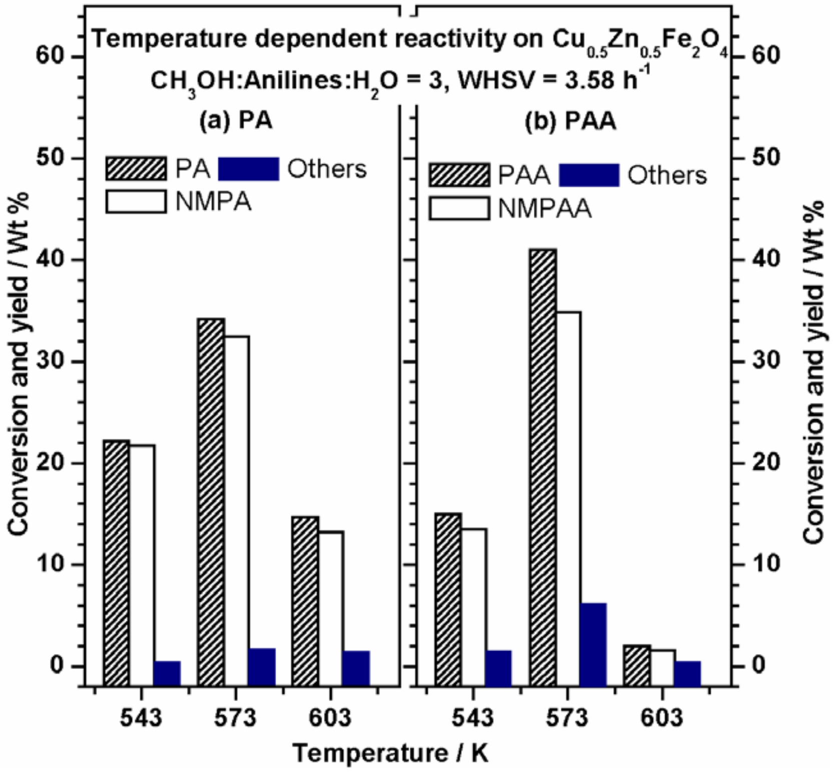

Figure 3.10: Temperature dependent reactivity of PA and PAA under optimized reaction condition on $Cu_{0.5}Zn_{0.5}Fe_2O_4$. NMPA and NMPAA are N-methyl-p-anisidine and N-methyl-p-aminoacetophenone, respectively. Other products, N,N-dimethylated and C-methylated anilines were obtained in traces.

A comparison of simple and substituted anilines catalytic activity data suggests that the optimum conditions for the maximum reactivity remains the same, irrespective of the substituents present in the phenyl ring with different electronic character.

3.5 Conclusions

Systematic search for the selective production of NMA from aniline lead to the conclusion that Cu^{2+} containing ferrite catalysts are the potential candidates. Further studies on Cu-Zn mixed ferrite exhibit a stable activity for longer period. This chapter covers the results from the catalytic study of selective NMA production from aniline methylation on $Cu_{1-x}Zn_xFe_2O_4$ over a wide range of temperatures and catalyst composition with methanol to aniline molar ratio of 3. Although all the catalyst compositions produce NMA selectively at 573 K, only x = 0.5 shows maximum aniline conversion under optimum reaction conditions. All the Cu-containing compositions show high initial activity, however the same decreases with increasing time on stream, except on x = 0.5. $ZnFe_2O_4$ shows hardly any catalytic activity hinting the direct role of Zn and Fe is negligible and Cu seems to be the active species for aniline methylation. Detailed catalytic activity studies show that Cu^{2+} is largely responsible for methylation and Zn^{2+} enhances the stability of the system while $ZnFe_2O_4$ does not display any significant activity towards methylation on its own.

Selective N-monomethylation of ring-substituted anilines (o-toluidine, m-toluidine, p-toluidine, p-anisidine, p-aminoacetophenone and 2,6-xylidine) was also carried out at optimum reaction conditions of 3:1:1 ratio of methanol:aniline:H_2O feed on $Cu_{1-x}Zn_xFe_2O_4$ (x = 0.05, 0.5 and 0.75). Among the catalyst compositions, again x = 0.5 shows maximum conversion with any aniline substrate as expected from aniline. Temperature dependent studies show that maximum anilines conversion is obtained at 573 K and the same decreases above and below 573 K due to different reasons. Selectivity for mono N-methylated products remains more than 95%, which decreases with increasing temperature. Only traces of N, N-dimethylated and C-methylated products were observed. Apparently, Electronic effects due to ring substituents do not play a significant role in the reactivity of the aniline substrates. However, steric factor plays a significant role and the same is clear from the results of o-toluidine and 2,6-xylidine.

3.6 References

1. H. Matsuhashi, K. Arata, Bull. Chem. Soc. Jpn. 64 (1991) 2605.
2. J. Santhalakshmi, T. Raja, Appl. Catal. A. 147 (1996) 69.
3. L. J. Garces, V. D. Makwana, B. Hincapie, A. Sacco, S. L. Suib, J. Catal. 217 (2003) 107.
4. B. L. Su, D. Barthomeuf, Appl. Catal. A. 124 (1995) 73.
5. B. L. Su, D. Barthomeuf, Appl. Catal. A. 124 (1995) 81.
6. P. S. Singh, R. Bandyopadhyay, B. S. Rao, Appl. Catal. A. 136 (1996) 177.
7. M. Onaka, A. Umezono, M. Kawai, Y. Izumi, J. Chem. Soc. Chem. Comm. (1985) 1202.
8. M. Selva, A. Bomben, P. Tundo, J. Chem. Soc. Perkin. Trans 1 (1997) 1042; M. Selva, P. Tundo, A. Perosa, J. Org. Chem. 66 (2001) 677; M. Selva, P. Tundo, A. Perosa, J. Org. Chem. 67 (2002) 9238; M. Selva, P. Tundo, A. Perosa, J. Org. Chem. 68 (2003) 7374.
9. A. K. Ko, C. L. Young, W. D. Zhu, H. E. Lin, Appl. Catal. A. 134 (1996) 53.
10. S. P. Elangovan, C. Kannan, B. Arabindo, V. Murugesan, Appl. Catal. A. 174 (1998) 213.
11. G. Klug, H. J. Buysch, L. Puppe, US Patent 5,068,434 (1991), to Bayer Aktiengesellschaft.
12. P. Wimmer, H. J. Buysch, L. Puppe, C. Froehlich, US Patent 5,055,617 (1991), to Bayer Aktiengesellschaft.
13. A. C. Bayer, C. U. Jr. Pittmann, L. Wang, E. G. Alley, A. C. Maliyackel, US Patent 5,030,759 (1991), to First Chemical Corporation.
14. R. Agrawal, S. R. Auvil, US Patent 5,026,912 (1991), to Air Products and Chemical, Inc.
15. K. Sreekumar, T. Raja, B. P. Kiran, S. Sugunan, B. S. Rao, Appl. Catal. A Chem. 182 (1999) 327.
16. K. Sreekumar, T. M. Jyothi, T. Mathew, M. B. Talawar, S. Sugunan, B. S. Rao, J. Mol. Catal. A Chem. 159 (2000) 327.
17. K. Sreekumar, T. Mathew, S. P. Mirajkar, S. Sugunan, B. S. Rao, Appl. Catal. A Chem. 201 (2000) L1.

18. K. Sreekumar, S. Sugunan, Appl. Catal. A Chem. 230 (2002) 245.

19. K. Sreekumar, S. Sugunan, J. Mol. Catal. A Chem. 185 (2002) 259.

20. T. Mathew, N. R. Shiju, K. Sreekumar, B. S. Rao, C. S. Gopinath, J. Catal. 210 (2002) 405.

21. T. Kotanigawa, M. Yamamoto, K. Shimokawa, Y. Yoshida, Bull. Chem. Soc. Jpn. 44 (1971) 1961.

22 .M. Mascaros, R.M. Navarro, L.G. Sainero, U. Costantio, M. Nocchetti, L.G. Fierro, J. Catal. 198 (2001) 338.

23 .J. March, Advanced Organic Chemistry, 4th Edn. Wiley-Interscience, New York, 1999.

Chapter 4: Aniline N-methylation mechanism on $Cu_{1-x}Zn_xFe_2O_4$: A DRIFTS study

4. 1 Introduction

The conventional pre- and post reaction investigations through physicochemical characterization contribute to some understanding about the reaction sequence. However, most often they do not adequately reflect the events that occur on the system under actual reaction conditions, such as, short-lived intermediates, surface complexes, spectator species and the reaction mechanism. The elucidation of reaction mechanisms in heterogeneous catalysis is a process that involves the reaction network findings, the determination of the sequence of each intermediate step of this network, and the identification and characterization of the active centers, the intermediate products, the activation processes of the reactants, and the surface reactions. In addition to the methods of reaction kinetics, the modern methods of *in situ* spectroscopy are increasingly used for the elucidation of the reaction sequence. IR, NMR, EPR, and UV/Vis spectroscopy techniques are universally used methods for the investigation of catalytically active sites on solid catalysts and the interaction of reactants with these sites. An important advantage of all the four methods lies in the possibility of being able to investigate working catalysts in contact with the reactants under real-world working conditions that is under reasonably high partial pressures of these reactants [1- 5].

Among these *in situ* spectroscopic techniques available, FTIR is the most useful and valuable technique to study heterogeneous catalysis owing to its high sensitivity and the ability to employ it under real-world catalytic reaction conditions. IR spectroscopy also provides a large amount of chemical as well as physical information such as different functional groups of reactants and products, mode of interaction with the catalyst surface, dissociation of reactants and the formation (and desorption) of products competitive adsorption of reactants etc. Further different mode of experiments available such as absorption, transmittance, reflectance and total attenuated reflectance makes any type of materials to be analyzed. The above aspects make IR spectroscopy highly useful than any other spectroscopy. In the recent years, it has been used increasingly for *in situ* investigations to understand the catalytic reaction mechanism. In order to visualize the events that proceed during reaction conditions and to learn the mechanistic aspects of the reaction, *in situ* investigations have to be carried out on the working catalysts directly in the spectrometer [6-8]. Hence a detailed investigation of adsorbed reactants (aniline, methanol and aniline + methanol mixture) and possible products (NMA, DMA and *o*-Toluidine) on $Cu_{1-x}Zn_xFe_2O_4$ (x = 0.05, 0.5, 1) system were carried out using temperature dependent *in situ* DRIFTS (Diffuse reflectance infrared Fourier transformed spectroscopy). The enhanced selectivity towards NMA over DMA and OT was discussed.

4.2 FTIR results

4.2.1 Adsorption of methanol

Figure 4.1 shows the temperature dependent FTIR spectra of methanol adsorbed on $Cu_{1-x}Zn_xFe_2O_4$ (x = 0.05, 0.5 and 1) systems and its vibrational assignments are given in Table 1. At 373 K methanol adsorbed dissociatively as surface methoxy group with characteristic bands at 2924, 2895, 2814, 1440 and 1063 cm^{-1} [9,10]. The C-H asymmetric (ν_{as}) and symmetric (ν_s) stretching vibrations of methoxy species was observed at 2924 and 2895 cm^{-1} and overtone methyl bending (2δ) appeared at 2814 cm^{-1}. The presence of methoxy species during methanol adsorption was indicated by C-O stretching mode at 1063 cm^{-1}, which appears at around 1035 cm^{-1} for liquid methanol. Other low frequency band at 1440 cm^{-1} was due to methyl group symmetric bending (δ_s). Since methanol undergoes oxidation on the present catalyst system, authentic spectra of formaldehyde and formic acid adsorbed on $Cu_{0.5}Zn_{0.5}Fe_2O_4$ are also given in Figure 4.1.

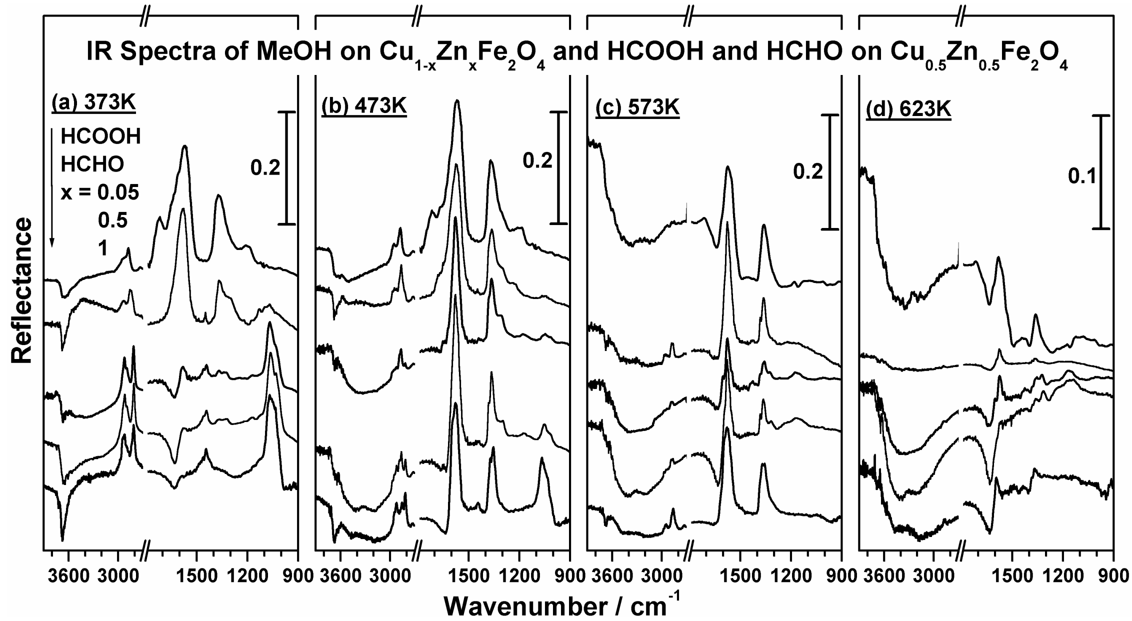

Figure 4.1: Temperature-dependent FTIR spectra of methanol adsorbed on $Cu_{1-x}Zn_xFe_2O_4$ for three selected compositions of x = 0.05, 0.5 and 1 at (a) 373 K, (b) 473 K, (c) 573 K and (d) 673 K. IR spectra of HCOOH and HCHO adsorbed on $Cu_{05}Zn_{0.5}Fe_2O_4$ at different temperatures are also shown for reference.

The vibrational assignments for the same are given in Table 4.2 for comparison. Adsorbed formaldehyde and formic acid also show the formate species with unique features at 2956, 2876, 1570 and 1370 cm^{-1}. At 373 K bands at 2938, 2850 and 1446 cm^{-1} were observed due to C-H asymmetric, symmetric and bending vibrations, respectively of adsorbed formaldehyde species, along with dioxymethylene [11] features at 2870, 1300 and 1068 cm^{-1}. This dioxymethylene was believed to be a surface intermediate species during the oxidation of formaldehyde to formic acid. As the temperature was increased to 473 K there was a loss in intensity of few bands with the formation of entirely new bands. However, such changes were prominent only on copper containing systems (x = 0.05 and 0.5) where new bands at 2868, 1302 and 1171 cm^{-1} were attributed to dioxymethylene species [11] formed by oxidation of methoxy species. This dioxymethylene species was not observed on $ZnFe_2O_4$, on which methoxy species were converted into formaldehyde [11] whose C-H stretching bands were observed at 2946 and 2856 cm^{-1}. Other bending modes were not visible as confirmed by adsorbed formaldehyde on x = 0.5 system (Figure 4.1b). It is to be noted that a strong C-O stretching frequency ($\nu_{C\text{-}O}$) due to surface methoxy species at 1063 cm^{-1} was seen on x = 0.5 and 1 system even at 473 K. On the other hand, x = 0.05 system shows a very weak $\nu_{C\text{-}O}$ at 1063 cm^{-1} which indicates a fast methanol oxidation between 373 and 473 K.

Table 4.1: Vibrational assignments of methanol on $Cu_{1-x}Zn_xFe_2O_4$ (x = 0.05, 0.5 and 1) at various temperatures.

Assignment	373 K			473 K			573 K		
	0.05	0.5	1	0.05	0.5	1	0.05	0.5	1
$\nu_{as}(CO_2^-)+\delta(CH)$	-	-	-	2950	2954	-	1065	-	-
2δ (CH)	-	-	-	-	-	2946	-	-	-
ν_{as} (CH)	2923	2924	2926	2624	2924	2923	-	-	-
ν_s (CH)	2895	2895	2898	-	-	-	-	-	-
ν_s (CH)	-	-	-	2883	2885	-	2878	2878	2880
ν_s (CH)	-	-	-	2868	2867	2856	-	-	2861
2δ (CH)	2814	2814	2814	2814	2818	2817	-	-	-
$\nu_{as}(CO_2^-)$	1580	1573	-	1576	1578	1576	1576	1578	1578
δ (CH)	1441	1442	1443	-	-	-	-	-	-
$\nu_s(CO_2^-)$	1368	1368	-	1364	1366	1363	1364	1364	1363
$\tau (CH_2)$	-	-	-	1306	1300	-	-	-	-
$\Gamma (CH_2)$	-	-	-	1180	1171	-	1176	1171	-
ν (CO)	1068	1065	1067	-	-	1065	-	-	-

Further, on all of the catalyst compositions a series of additional bands appeared at 2952, 2884, 1578 and 1364 cm^{-1} were ascribed to formate species. This was further confirmed from the IR features of adsorbed formic acid on x = 0.5 system (Figure 4.1). Few features of formate species (1578 and 1364 cm^{-1}) were seen even at above 573 K due to surface bidentate carbonate formation [12] and no C-H signatures were observed. These changes were also observed on adsorbing HCHO/HCOOH over x = 0.5 system. It was evident that methanol dissociates to methoxy species at 373 K and then converted to formate species which was completely oxidized to typical reformate products at above 473 K on all of the catalyst compositions.

Table 4.2: Vibrational assignments of formaldehyde and formic acid on $Cu_{0.5}Zn_{0.5}Fe_2O_4$ at various temperatures.

Assignment	373K		473K		573K	
	HCOOH	HCHO	HCOOH	HCHO	HCOOH	HCHO
$\nu_{as}(CO_2^-)+\delta(CH)$	2956	-	2956	2952	-	2960
2δ (CH)	-	2938	-	-	-	-
ν_s (CH)	2876	2850	2877	2870	-	2883
$\nu_{as}(CO_2^-)$	1570	1580	1566	1574	1573	1578
δ (CH)	-	1446	-	-	-	-
$\nu_s(CO_2^-)$	1370	1366	1368	1364	1360	1364
τ (CH_2)	-	1300	-	1301	-	-
ν (CO)	-	1068	-	-	-	-

4.2.2 Adsorption of aniline

Figure 4.2 shows the IR results of aniline adsorbed molecularly on $Cu_{1-x}Zn_xFe_2O_4$ catalyst (x = 0.05, 0.5 and 1) at 373 K. N-H asymmetric and symmetric stretching frequency appears at lower wavenumber around 3320 and 3228 cm^{-1} compared to liquid aniline [13] at 3355 and 3290 cm^{-1}, respectively, indicating a weak N-H bond on adsorption. A broad -OH stretching band between 3800 and 3500 cm^{-1} was observed due to the interaction of proton from polarized amino group with surface oxygen and thus forming surface hydroxyl groups. As -NH_2 deformation band overlaps with phenyl ring stretching bands of aromatic amines [13] ($\nu_{C=C}$) around 1600 cm^{-1}, these bands were not resolved for adsorbed aniline in this present case. A series of low intensity overtone bands observed at 1935, 1860, 1795 and 1725 cm^{-1} are attributed to out of plane aromatic C-H bending vibrations (γ_{C-H}) that clearly indicates the perpendicular adsorption of aniline on the catalyst surface [14,15].

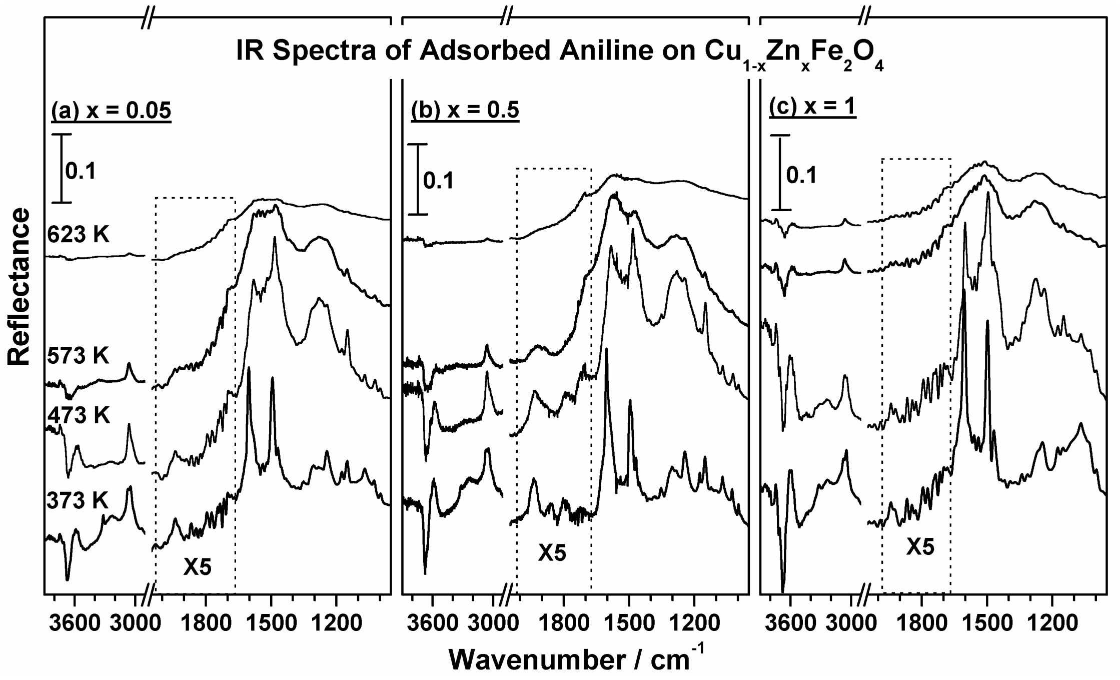

Figure 4.2: Temperature dependent FTIR spectra of aniline adsorbed on $Cu_{1-x}Zn_xFe_2O_4$ for three selected catalyst compositions of (a) x = 0.05, (b) x = 0.5 and (c) x = 1.0. Note that the 2050-1750 cm^{-1} region is multiplied by a factor of 5 to show the out-of-plane C-H bending features clearly.

Bands at 1150, 1245 and 1290 cm^{-1} were ascribed to ν_{C-N} (C-N stretching vibrations) and a pair of strong bands at 1495 and 1600 cm^{-1} were due to phenyl ring C=C stretching vibrations (ν_{13a}, ν_{16a}) [16,17]. These ring-stretching modes were accompanied with a shoulder at 1460 cm^{-1} (ν_{13b}). Aromatic C-H stretchings (ν_{C-H}) were observed at 3070 and 3045 cm^{-1}. The bands that appeared at the lower wavenumber side between 1100 and 1000 cm^{-1} were due to aromatic C-H in-plane bending vibration (β_{C-H}). The above IR features for adsorbed aniline were observed on all of the catalyst compositions at 373 K indicating the similar mode of interaction.

On increasing the temperature to 473 K, $\nu_{N\text{-}H}$ at 3320 and 3228 cm^{-1} disappears since aniline chemisorbs very strongly on the surface and lead to complete N-H bond scission. This occurs on x = 0.05 and 0.5 systems, whereas $\nu_{N\text{-}H}$ were clearly observed even at 473 K on pure $ZnFe_2O_4$. The low intensity $\gamma_{C\text{-}H}$ vibrations start broadening and slowly disappearing with increasing temperature on x = 0.05 and 1 indicates a fairly parallel or tilted phenyl ring on the catalyst surface. However, $\gamma_{C\text{-}H}$ was strong even at 573 K on x = 0.5 system suggesting a perpendicular orientation of the phenyl ring. A red shift of about 15 cm^{-1} for ν_{16a} and 10 cm^{-1} for ν_{13a} of C=C stretching vibration was observed on x = 0.05 and 0.5 systems, whereas no such shift was observed on $ZnFe_2O_4$.

The ring-stretching mode (ν_{13b}) at 1460 cm^{-1} merges with ν_{13a} stretching mode and slightly shifts to higher frequency side and appears as a shoulder. An overlap in $\nu_{C\text{-}N}$ at 1245 and 1290 cm^{-1} occurs with increasing temperature. Another $\nu_{C\text{-}N}$ at 1150 cm^{-1} of aniline appears very strong and indicates aniline was predominantly bound to the copper containing catalyst surface. Nonetheless, this peak appears very weak in intensity along with aromatic C-H in plane bending vibrations on $ZnFe_2O_4$. A general decrease in intensity of all the peaks at 573 K indicates desorption of aniline sets in above 473 K. However, aromatic C-H and N-H stretching frequency appeared on $ZnFe_2O_4$ at all temperature indicates the molecular adsorption and desorption without any dissociation.

4.2.3 Adsorption of NMA, DMA and OT

Figure 4.3 (a, b and c) shows the IR spectra of NMA adsorbed at different temperatures on x = 0.05, 0.5 and 1, respectively. N-H stretching band (3230 cm^{-1}) appears very weak at 373 K. $\gamma_{C\text{-}H}$ were observed at 1935, 1860, 1795 and 1725 cm^{-1} indicates that phenyl ring was perpendicular to the catalyst surface on all of the catalyst compositions. $\nu_{C\text{-}N}$

appeared at 1140 (aliphatic) and 1220, 1240 cm^{-1} (aromatic). Aromatic $\nu_{C=C}$ appeared at 1595 (ν_{16a}) and 1495 cm^{-1} (ν_{13a}) and the latter was accompanied with 1460 cm^{-1} (ν_{13b}). The methyl group symmetric bending (δ_s) was observed at 1355 cm^{-1}. Asymmetric and symmetric stretchings of methyl group appeared at 2850 and 2820 cm^{-1}, respectively.

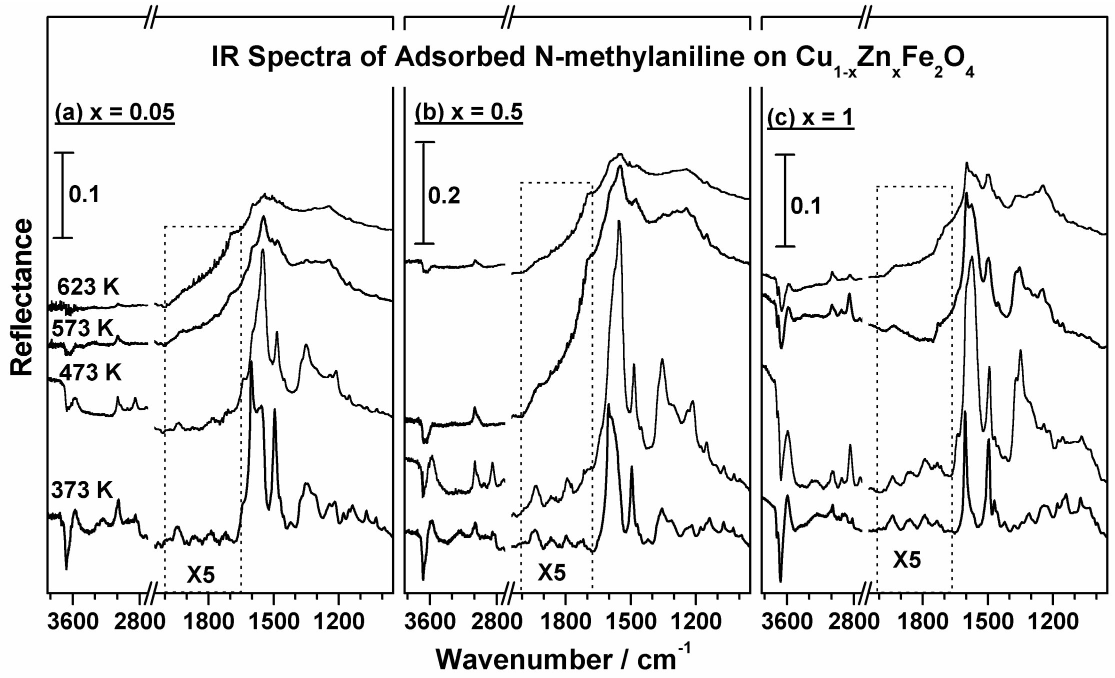

Figure 4.3: Temperature-dependent FTIR spectra of NMA adsorbed on $Cu_{1-x}Zn_xFe_2O_4$ for three selected compositions of (a) x= 0.05, (b) x= 0.5 and (c) x= 1.0. Note that the 2050-1700 cm^{-1} region is multiplied by a factor of 5 to show the features clearly.

Aromatic C-H stretching band was observed at 3050 cm^{-1}. As the temperature was increased to 473 K, $\nu_{C=C}$ shows red shift by 40 cm^{-1} in ν_{16a} and 10 cm^{-1} in ν_{13a}. These shifts were observed on copper containing catalysts whereas $ZnFe_2O_4$ shows a red shift of 20 cm^{-1} in ν_{16a}. $\nu_{C\text{-}N}$ at 1140 cm^{-1} became weak in intensity and at the same time other two $\nu_{C\text{-}N}$ bands at 1220 and 1240 cm^{-1} became strong and overlap with each other. NMA desorption occurs above 473 K and spectral features at above 573 K appeared broad on x = 0.05 and 0.5 systems, whereas x=1 shows very sharp and clear bands. This indicates NMA chemisorbs strongly on x=1 even at high temperature (> 573K).

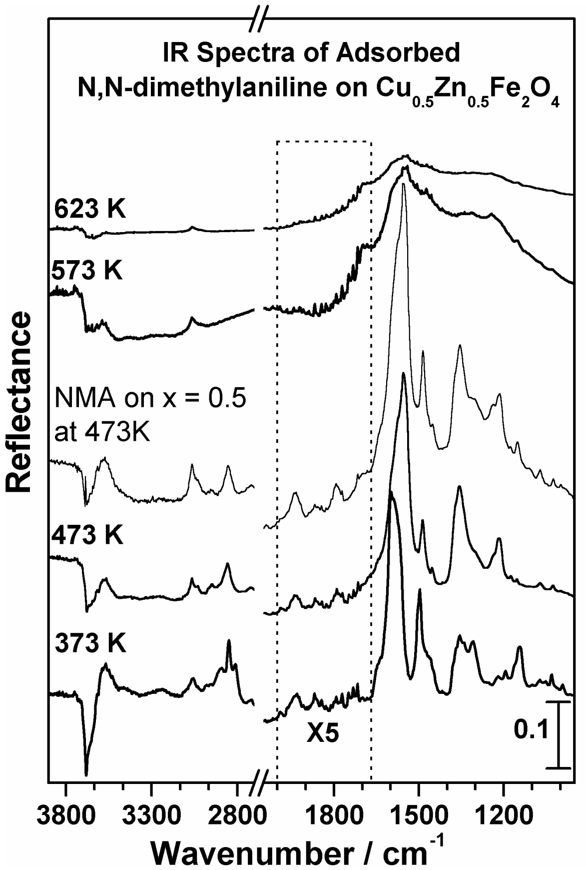

Figure 4.4: Temperature-dependent FTIR spectra of DMA adsorbed on $Cu_{0.5}Zn_{0.5}Fe_2O_4$. Note that the 2050-1700 cm^{-1} region is multiplied by a factor of 5 to show the features clearly. NMA adsorbed is also shown for comparison.

Figure 4.4 shows IR spectra of DMA adsorbed on $Cu_{0.5}Zn_{0.5}Fe_2O_4$ whose spectral features have definite similarities with NMA features except a few differences that are highlighted in the following. The aromatic $\nu_{C\text{-}N}$ band at 1240 cm^{-1} with good intensity for NMA was hardly seen for DMA. In contrast, aliphatic $\nu_{C\text{-}N}$ at 1140 cm^{-1} appeared very strong for DMA due to two methyl groups attached to nitrogen. Methyl group (δ_s) band at 1355 cm^{-1} was higher in intensity for DMA than NMA. The $\gamma_{C\text{-}H}$ for DMA was very weak compared to NMA and aniline suggests that phenyl ring was either tilted or parallel to the catalyst surface. This is attributed to steric factors due to two methyl groups at nitrogen atom. Aromatic $\nu_{C\text{-}H}$ appeared around 3060 cm^{-1} and weak in intensity compared to methyl group $\nu_{C\text{-}H}$ at 2850 cm^{-1}. Unlike NMA, an additional $\nu_{C\text{-}H}$ band was observed at 2890 cm^{-1}.

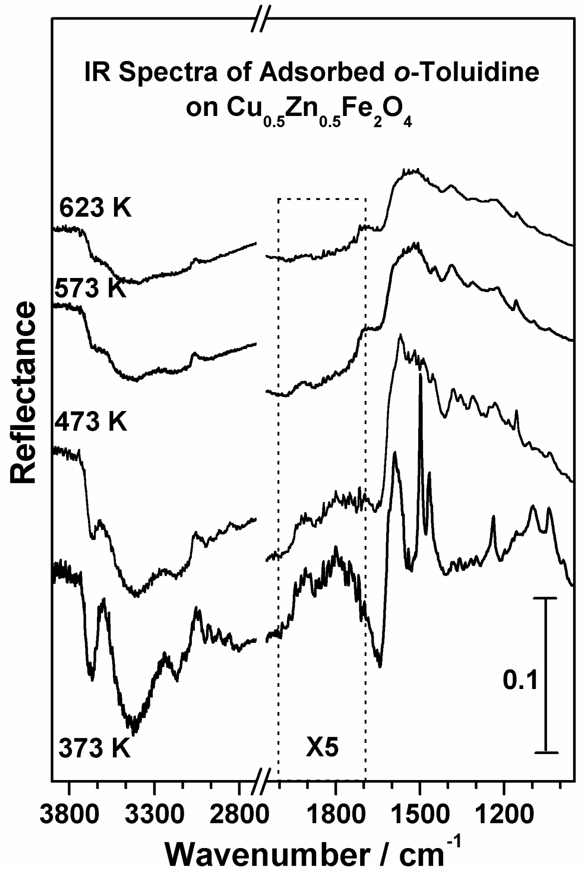

Figure 4.5: Temperature-dependent FTIR Spectra of *o*-toluidine adsorbed on $Cu_{0.5}Zn_{0.5}Fe_2O_4$. Note that the 2050-1700 cm^{-1} region is multiplied by a factor of 5 to show the features clearly.

At 473 K $\nu_{C=C}$ were shifted to lower frequency by 40 cm^{-1} for ν_{16a} and 10 cm^{-1} for ν_{13a}. A noticeable decrease in extinction coefficient (ε_{max}) of ν_{13b} mode was observed compared to NMA features. $\nu_{C\text{-}N}$ at 1140 cm^{-1} disappeared and 1220 cm^{-1} became strong; at this temperature DMA spectral features resemble NMA spectral features. However, aromatic to aliphatic C-H stretching band intensity ratio is more for DMA compared to NMA (Figure 4.4).

Figure 4.5 shows *o*-toluidine spectral features adsorbed on $Cu_{0.5}Zn_{0.5}Fe_2O_4$. $\nu_{N\text{-}H}$, aromatic ring $\nu_{C=C}$ and $\nu_{C\text{-}N}$ have a resemblance with aniline features, except an intensity difference in $\nu_{C=C}$; ν_{13a} vibration which is stronger than ν_{16a}. Methyl group δ_s was observed very weak at 1380 cm^{-1}. Weak phenyl ring $\gamma_{C\text{-}H}$ band at 1820 cm^{-1} suggests that phenyl ring is somewhat perpendicular to the catalyst surface. $\nu_{C\text{-}H}$ appeared at 2860, 2926 and 2975 cm^{-1}

(methyl group) and at 3060 cm^{-1} (phenyl ring). A general decrease in intensity of all bands above 473 K shows desorption of *o*-toluidine; further bands were difficult to be resolved due to broadening at high temperatures.

4.2.4. Adsorption of methanol: aniline reaction mixtures

Figure 4.6 shows adsorption of methanol:aniline reaction mixtures with three molar ratios (1:1, 3:1 and 5:1) at different temperatures (373 K to 623 K) on x = 0.5 system. The bands observed at 373 K for different ratios of aniline and methanol on the catalyst (Figure 4.6a) indicates a simple co-adsorption of aniline and methanol with no significant interaction among them. Methanol was adsorbed dissociatively as surface methoxy group on the catalyst and the spectral features matches with that of adsorbed methanol. The phenyl ring orientation of aniline was perpendicular and it was evident from γ_{C-H} bands at 2050-1700 cm^{-1}. However, significant spectral changes take place above 373 K are mentioned as follows. No signature of formate species, 2973, 2884, 1578 and 1365 cm^{-1} had been observed above 373 K irrespective of aniline to methanol feed ratio. This indicates methanol oxidation to formic acid was hindered in the presence of aniline. In contrast to IR features at 373 K, methoxy species ν_{C-O} (1063 cm^{-1}) and ν_{C-H} (2924, 2895 and 2814 cm^{-1}) were completely vanished at 473 K for 1:1 and 5:1 feed.ratios; whereas an intense ν_{C-H} and ν_{C-O} of methoxy features exist only for 3:1 feed ratio, which completely disappeared at 573 K The above observations clearly show that methanol was either utilized for methylation or oxidized to typical reformate products and a combination of both. $\nu_{C=C}$ bands at 1600 and 1495 cm^{-1} at 373 K shifts to 1558 and 1483 cm^{-1} at 473 K, respectively. The $\nu_{C=C}$ bands decreased in intensity and broadened at high temperature.

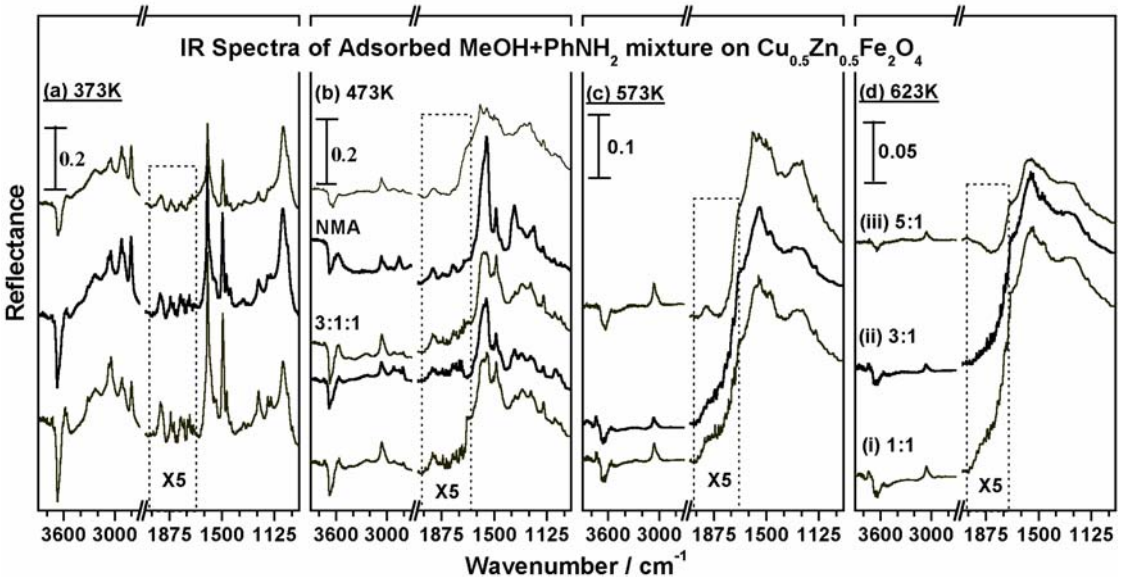

Figure 4.6: Temperature- and feed composition-dependent FTIR spectra of methanol+aniline co-adsorbed on $Cu_{0.5}Zn_{0.5}Fe_2O_4$ system. Three different methanol:aniline feed compositions, namely (i) 1:1, (ii) 3:1 and (iii) 5:1 are employed. 3:1:1, Feed with water adsorbed at 473 K is shown for comparison. NMA adsorbed at 473 K is shown for reference. Note that 2050-1700 cm^{-1} region is multiplied by a factor of 5 to show the features clearly.

A decrease in intensity of ν_{C-N} at 1150 cm^{-1} and a new peak at 1220 cm^{-1} coupled with a 1240 cm^{-1} peak was observed. The above said changes were observed for adsorbed NMA on x = 0.5 system at 473 K and given in Figure 4.6b. Other new band at 1355 cm^{-1} matches well with methyl group bending vibration observed for methylated anilines especially that of NMA and obviously ν_{C-H} of methyl groups was present at 2850 cm^{-1}. This highlights the formation of main product NMA at 473 K on the catalyst surface.

Effectively there was no catalytic aniline conversion and NMA production was observed at 473 K. This is in contrast to large (no) NMA production at 573 K (473 K) under catalytic reaction conditions. Besides, 5:1 feed composition shows less intense and broadened aniline features at 473 K. At above 573 K, very broad bands of phenyl ring stretching with clear aromatic ν_{C-H} stretching was seen for all the feed composition. 3:1:1 ratio of methanol:aniline:water at 473 K on x = 0.5 system was also given to show the effect of water on methylation (Figure 4.6b). The spectral features of aniline and methanol hardly show any change that highlights water did not take part directly in any of the reaction sequence that aniline and methanol undergo. However, it just enhances the stability of the catalyst by removing the coke deposits on catalyst surface and enhances the catalyst lifetime as it was observed in TOS catalyst stability study for 100 h. (Chapter 3).

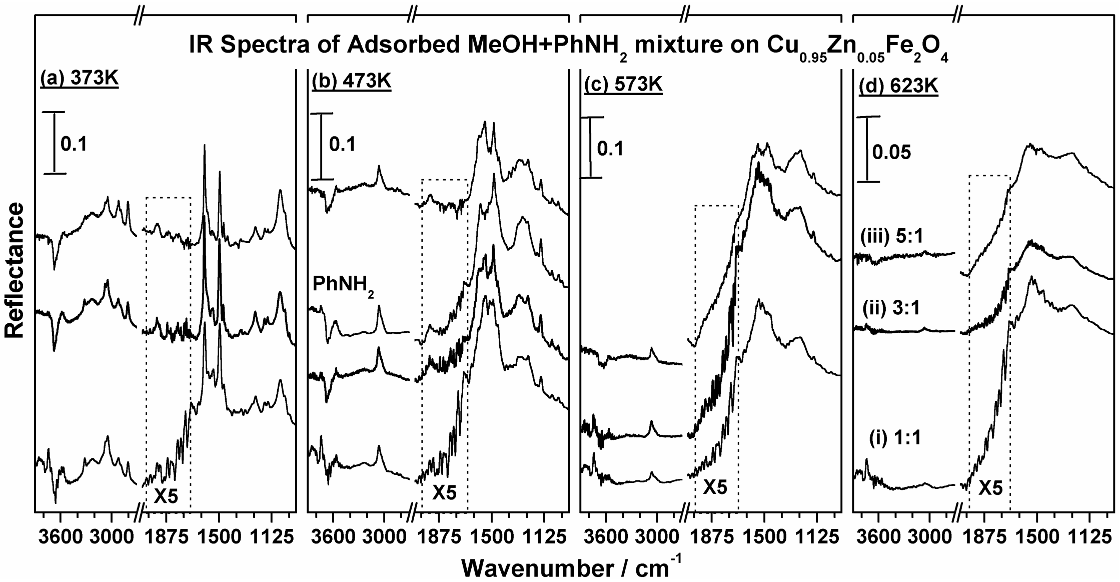

Figure 4.7: Temperature- and feed composition-dependent FTIR spectra of methanol+aniline co-adsorbed on $Cu_{0.95}Zn_{0.05}Fe_2O_4$ system. Three different methanol:aniline feed compostions, namely (i) 1:1, (ii) 3:1 and (iii) 5:1 are employed. Aniline adsorbed at 473 K is also shown for reference. Note that the 2050-1700 cm^{-1} region is multiplied by a factor of 5 to show the features clearly.

Figure 4.7 shows adsorption of methanol:aniline reaction mixtures with three molar ratios (1:1, 3:1 and 5:1) at different temperatures (373 K to 623 K) on x = 0.05 system. The bands observed at 373 K for different ratios of aniline and methanol on the catalyst (Figure 4.7a) indicates a simple co-adsorption of aniline and methanol with no significant interaction among them. Methanol was adsorbed dissociatively as surface methoxy group on the catalyst and the spectral features matches with that of adsorbed methanol. The phenyl ring orientation of aniline was perpendicular and it was evident from γ_{C-H} bands at 2050-1700 cm^{-1}. However, significant spectral changes take place above 373 K are mentioned as follows. No signature of formate species 2973, 2884, 1578 and 1365 cm^{-1} had been observed above 373 K irrespective of aniline to methanol feed ratio. This indicates methanol oxidation to formic acid was hindered in the presence of aniline. In contrast to IR features at 373 K, methoxy species $\nu_{C\text{-}O}$ (1063 cm^{-1}) and $\nu_{C\text{-}H}$ (2924, 2895 and 2814 cm^{-1}) were completely vanished at 473 K for all the feed ratios. Only aniline features without any methanol features were seen at 473 K and that was attributed to unreacted aniline. Surface methoxy species were oxidized to reformate products and hence the disappearance of methanol derived features at 473 K that is independent of methanol to aniline ratios. $\nu_{C=C}$ of phenyl ring at 1585 and 1485 cm^{-1}, $\nu_{C\text{-}N}$ at 1150 and 1240 cm^{-1} observed were attributed to unreacted aniline on $x = 0.05$ system. This is in good agreement with the spectra observed for adsorbed aniline on $x = 0.05$ at 473 K (Figure 4.7b). IR spectra recorded at above 573 K is in good resemblance to that of aniline on $x = 0.05$

Figure 4.8 shows adsorption of methanol:aniline reaction mixtures with three molar ratios (1:1, 3:1 and 5:1) at different temperatures (373 K to 623 K) on $x = 1$ system. The bands observed at 373 K for different ratios of aniline and methanol on the catalyst (Figure 4.8a) indicates a simple co-adsorption of aniline and methanol with no significant interaction among them. Methanol was adsorbed dissociatively as surface methoxy group on the catalyst and the spectral features match with that of adsorbed methanol. The phenyl ring orientation of aniline was perpendicular and it was evident from $\gamma_{C\text{-}H}$ bands at 2050-1700 cm^{-1}. However, significant spectral changes take place above 373 K are mentioned as follows. No signature of formate species 2973, 2884, 1578 and 1365 cm^{-1} had been observed above 373 K irrespective of aniline to methanol feed ratio. This indicates methanol oxidation to formic acid was hindered in the presence of aniline. Spectral features of $\nu_{C\text{-}O}$ (1063 cm^{-1}) and $\nu_{C\text{-}H}$ (2924, 2895 and 2814 cm^{-1}) for methoxy species were seen very clearly even at 473 K which was dependent on methanol concentration; Higher the methanol to aniline molar ratio stronger the band intensity of methoxy species.

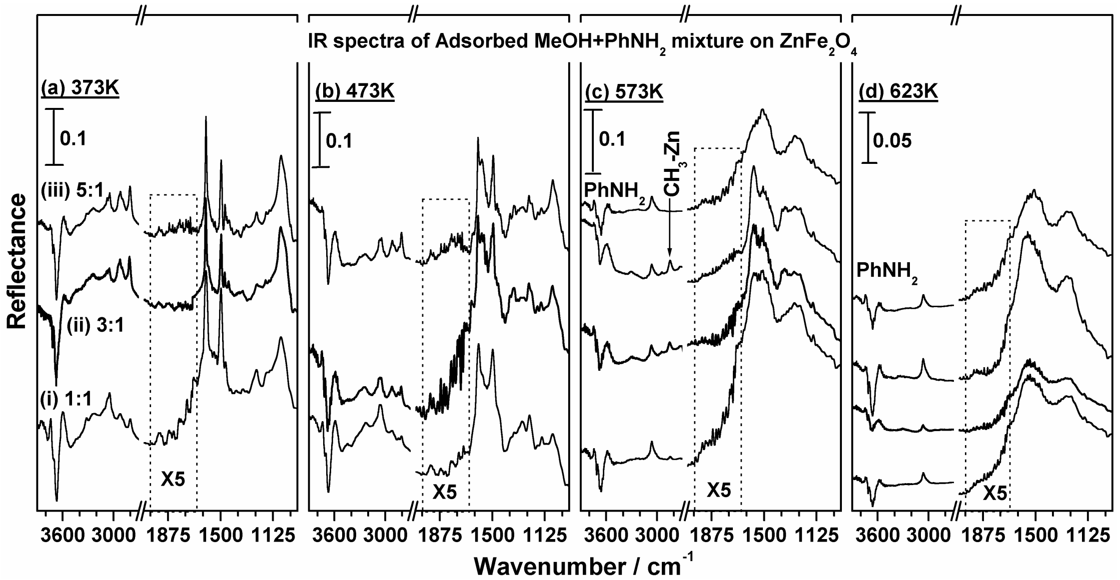

Figure 4.8: Temperature- and feed compostion-dependent FTIR spectra of methanol+aniline co-adsorbed on $ZnFe_2O_4$. Three different methanol:aniline feed compostions, namely (i) 1:1, (ii) 3:1 and (iii) 5:1 are employed. Aniline adsorbed at 473 K is also shown for reference. Note that the 2050-1700 cm^{-1} region is multiplied by a factor of 5 to show the features clearly.

ν_{C-H} at 2852 cm^{-1} was even observed at 573 K without ν_{C-O} band indicating a stable CH_3-Zn feature (Figure 4.8c dotted arrow) that vanished only at 623 K. As evident from the spectral features, no new bands appeared or disappeared at 473 K for adsorption of all methanol:aniline feed ratio. The spectra were ascribed to chemisorbed methanol:aniline mixture without any interaction among them even at 473 K irrespective of the feed ratio. No shift in $\nu_{C=C}$ and ν_{C-N} bands were observed as in the case of aniline on the catalyst at 473 K. Above 473 K, although aniline N-H bond scission takes place to some extent hardly there was any change in aniline features. No bands due to any of the possible products were seen even at above 373 K.

4.3 Discussion

4.3.1 Reactivity of methanol, formaldehyde and formic acid

Copper containing systems (x = 0.05 and 0.5) behave differently from $ZnFe_2O_4$ when methanol was the sole adsorbate. Although on all of the catalyst compositions methanol was oxidized to formate species above 373 K, on copper containing systems surface methoxy species was first converted to dioxymethylene species and then to formate species. In contrast to the above methanol decomposition, a different route through HCHO formation was observed and identified from the C-H stretching vibrations at 2946 and 2856 cm^{-1} on $ZnFe_2O_4$. Also an intense $\nu_{C\text{-}O}$ band even at 473 K on $ZnFe_2O_4$ suggests the presence of stable methoxy species. Above 373 K methoxy species was oxidized to formate species, which was very pronounced on copper rich compositions especially on x = 0.05 system.

It is to be noted that adsorbed HCHO over $Cu_{0.5}Zn_{0.5}Fe_2O_4$ was also oxidized to dioxymethylene species at 373 K. This indicates copper promotes the above oxidation rapidly and suggests that no stable formaldehyde could be identified over copper containing systems above 373 K. In other words, a faster oxidation of methoxy species to dioxymethylene, formate and then to reformate products leads to faster reduction of copper species and hence catalysts deactivation.

On x = 0.05, methyl or methoxy species features vanished below 473 K and completely oxidized to reformate products between 373 K and 573 K and this could be the reason for its fast deactivation during reaction conditions compared to other Cu-containing compositions. Further, methyl group signatures were seen clearly over $ZnFe_2O_4$ even above 473 K indicating a strong chemisorption of methanol-derived species. Hence, a 1:1 copper and zinc combination on x = 0.5 system catalyze minimum methanol oxidation and maximum methyl species availability for methylation. This reveals the importance of the role of Zn in aniline methylation reaction by slowing down the methanol oxidation reaction and acts as a spacer for better distribution of Cu.

4.3.2 Reactivity of anilines and methylated anilines

Aniline and methylated anilines, NMA, DMA and OT are adsorbed on to the catalyst system as a coordinated species. The nitrogen atom of aniline coordinates to the cationic sites, which act as Lewis acid center, and thereby N-H bond became weak. N-H bond was further polarized and the proton from polarized -NH_2 group interacts with surface oxygen to form surface -OH. This is evident from a broad -OH stretching band between 3800 and 3500 cm^{-1} whose intensity decreases with increasing temperature. This N-H bond polarization affects ν_{C-N} of aniline as evident from a sharp and strong band at 1150 cm^{-1} (intensity increases with temperature) along with 1245 and 1290 cm^{-1}. The phenyl ring perpendicular to the catalyst surface was identified from the low intensity γ_{C-H} bands and it is free from interaction with the catalyst surface; hence phenyl ring C-H can freely undergo out of plane bending vibrations [14,15]. However, parallel orientation of adsorbed OT shows no well-defined γ_{C-H} and supports the above statement. The complete N-H bond scission occurs above 373 K as it was seen from the disappearance of N-H stretching band between 3320 - 3230 cm^{-1} at 473 K for copper containing systems. However, at 473 K ν_{N-H} band was strong on $ZnFe_2O_4$ that shows poor catalytic activity and suggests that N-H bond scission could be a rate-limiting step for aniline methylation.

NMA adsorption on catalyst surface followed a similar trend as aniline adsorption. However, ν_{C-N} and $\nu_{C=C}$ have notable differences; aliphatic ν_{C-N} appears at 1140 cm^{-1} with aromatic ν_{C-N} at 1220 and 1240 cm^{-1}, out of which 1140 cm^{-1} disappeared above 473 K. Further, phenyl ring orientation to the catalyst surface was perpendicular and comparable to that of aniline and clearly shows NMA orientation was stabilized in a perpendicular fashion on catalyst surface as evident from γ_{C-H} between 2050 and 1700 cm^{-1}. Above bands were relatively strong on $x = 0.5$ system. This suggests that extent of phenyl ring perpendicularity of NMA was high on $x = 0.5$ system, despite a methyl group at N center.

DMA bands were obviously similar to NMA adsorption band features, however the intensity is different. A less intense γ_{C-H} bands were observed suggests that phenyl ring orientation in DMA was tilted towards or parallel to the catalysts surface. OT shows very weak interaction with the catalyst surface compared to aniline, NMA and DMA. The adsorption bands have similarities as that of aniline, except the high intensity ratio of ν_{13a}/ν_{16a}. A general decrease in intensity of all the bands at 473 K was ascribed to the weak interaction of OT with the catalyst surface and hence a faster desorption.

4.3.3 Reactivity of methanol:aniline mixtures on $Cu_{1-x}Zn_xFe_2O_4$

IR spectra due to methanol:aniline mixtures show no significant interaction among them at 373 K. On increasing the temperature spectral changes takes place depending on catalysts composition and methanol:aniline ratio. Methanol oxidation to formate species was hindered in the presence of aniline, which was in contrast to the interaction of methanol alone on the catalyst surface. This may be a due to the protonation process that hinders the formate species formation from methanol in the presence of aniline. In addition, the extent of methanol protonation depends on the ease of aniline N-H bond scission that occurs above 373 K on x = 0.05 and 0.5 and ≥ 573 K on x = 1.

On x = 0.05 system no methanol derived features were seen at 473 K, indicating that protonated methanol undergoes oxidation to form typical reformate products. Consequently, faster reduction of active Cu^{2+} to Cu^0 and hence methylation activity ceases irrespective of the methanol:aniline ratio. XPS analysis results also show a large reduction of Cu^{2+} to metallic Cu on spent catalysts (Chapter 5). Hence aniline methylation was not effective on x = 0.05; catalytic reaction results also show some initial aniline conversion that declines very fast with high TOS on x = 0.05 system.

On x = 0.5 system, methanol protonation was favored as aniline N-H bond scission took place between 373 and 473 K. Zn having strong tendency to stabilize the methyl species prevents them from further oxidation by Cu^{2+} and aids for an efficient methylation. This synergistic performance of Cu-Zn varies considerably with methanol:aniline ratio; at equimolar ratio (1:1) methyl cation availability is less and at higher ratio (5:1) more methanol tends to dissociate to reformate products and led to Cu^{2+} reduction. An intermediate methanol to aniline ratio (3:1) shows a steady state aniline conversion with no catalyst deactivation for longer reaction time as revealed from the catalytic studies.

Aniline spectral features also changes with respect to catalyst composition, methanol to aniline ratio and temperature. On x = 0.5 system, γ_{C-H} bands observed between 2050 and 1700 cm^{-1} irrespective of the feed ratio suggests that phenyl ring orientation is perpendicular at 373 K. N-H bond scission takes place irrespective of the feed ratio suggest that aniline was preferentially bound to the catalysts surface. Like NMA, above 373 K, $\nu_{C=C}$ bands of aniline at 1600 and 1495 cm^{-1} shift to 1560 and 1485 cm^{-1}, respectively for 1:1 and 3:1 feed composition. Aniline ν_{C-N} bands 1245 and 1290 cm^{-1} were accompanied with a new band at 1220 cm^{-1} that matches well with that of ν_{C-N} of NMA. Other ν_{C-N} originates from chemisorbed aniline at 1150 cm^{-1} became weak at above 373 K. This indicates strongly interacting aniline was methylated to NMA irrespective of the feed ratio. Methyl group at 1355 (δ_s), 2820 (ν_s) and 2850 cm^{-1} (ν_{as}) appears very strong for 3:1 methanol to aniline ratio compared to other two feed ratios and suggests that 3:1 ratio could be optimum for effective aniline methylation to NMA. No interaction between methanol and aniline was clear from the spectral features at 473 K for all the feed ratios on $ZnFe_2O_4$. γ_{C-H} of phenyl ring was very weak compared to other two catalyst compositions indicating that aniline orientation was comparatively tilted on $ZnFe_2O_4$. ν_{C-N} and $\nu_{C=C}$ bands shows hardly any changes in band positions and intensities for all the feed ratios at 473 K, unlike copper containing catalysts. ν_{C-N}, ν_{C-H} and $\nu_{C=C}$ of aniline broadened with decreasing intensity indicates the onset of aniline desorption above 573 K. However, ν_{C-H} band at 2856 cm^{-1} appeared strong at 573 K indicates the stability of methyl species (Figure 4.8c) and hardly there is any interaction among reactants even at high temperature. Catalytic reaction results on $ZnFe_2O_4$ also show small amount of aniline methylation to NMA at any reaction temperature.

4.3.4 Mechanism of aniline methylation on $Cu_{1-x}Zn_xFe_2O_4$

A possible reaction mechanism is suggested and the same is pictorially represented in Figure 4.9. It shows that aniline molecule is activated through N-H bond polarization on Lewis acidic sites, which led to N-H bond scission between 373 and 473 K on Cu-containing catalysts. This lead to an unsaturated, and electron rich coordinatively bonded N atom on the catalysts surface. N-H bond scission leaves a labile H^+ on the surface that protonates methanol ($CH_3\overset{+}{O}H_2$) and its dissociation lead to electrophilic $CH_3^{\delta+}$ and water. Thus electron rich N-atom was preferentially attacked by $CH_3^{\delta+}$ group. In addition, perpendicular orientation of aniline on all Cu-containing catalysts composition was facile for product formation. Some supporting evidences for the above mechanism are given in the following section.

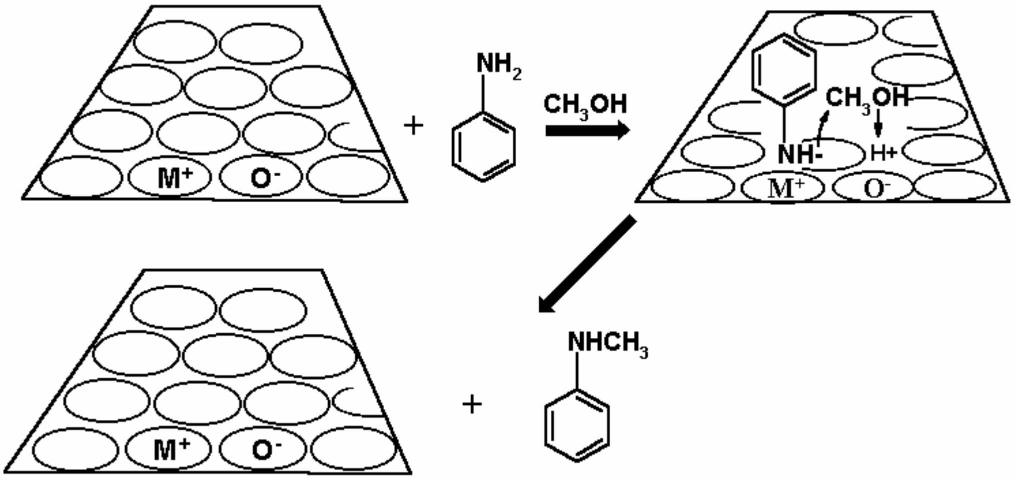

Figure 4.9: A pictorial representation of aniline N-methylation mechanism

To support the above proposed aniline methylation mechanism, IR experiments with aniline and methanol adsorbed sequentially before or after pyridine adsorption on catalyst was carried out [9]. Aniline and methanol protonation is highly unlikely on the virgin catalyst surface since the surface -OH group was incapable of protonating even strong bases like pyridine (absence of pyridinium ion band or Bronsted acid sites) [18]. Hence, Lewis acid-base pair sites are the most probable sites for adsorption of aniline and methanol. Since aniline is more basic than methanol, Lewis acid-base pair sites are covered by aniline and that enhances aniline N-H bond scission. N-H bond scission on acid-base pair sites generates labile H^+ on the surface. This freshly formed surface H^+ group has a tendency to protonate methanol molecules leading to $CH_3^{\delta+}$ cations. Proton from N-H bond scission of adsorbed aniline changes the course of methanol interaction through protonation. Methanol molecules are directed to adsorb on H^+ released from aniline and hence the active center for N-methylation is likely to be single acid-base pair site. The above suggested aniline single methylation mechanism was verified by three different experiments.

Figure 4.10 (a-c) shows sequential adsorption of reactants with acidity probe molecules like pyridine was carried out at different temperature on $Cu_{0.5}Zn_{0.5}Fe_2O_4$. Figure 4.10a shows the sequential adsorption of aniline, pyridine and then methanol at 373 K. Aniline and pyridine features coexist after pyridine exposure to aniline adsorbed catalyst surface. However, methanol features were hardly seen with subsequent methanol adsorption. Figure 4.10b shows the co-adsorption of a 1:1 ratio of aniline and pyridine at various temperatures. The catalyst surface was clearly dominated by pyridine features at 373 K. However, due to broad features at 1495 and 1600 cm^{-1}, aniline bands were unresolved from pyridine bands. At 473 K a broadening of 1600 cm^{-1} peak up to 1540 cm^{-1} clearly shows pyridinium ion formation [18,19]. This supports the N-H bond dissociation, methanol protonation and subsequent aniline methylation mechanism. The above result also indicates that the pyridine and aniline are equally competing for the adsorption sites when adsorbed sequentially, but pyridine competes at a higher level in the case of co-adsorption being more basic than aniline. Figure 4.10c shows both the sequential and the co-adsorption of methanol and pyridine. Sequential adsorption of methanol and pyridine carried out at 373 K clearly demonstrates that initially adsorbed methanol was displaced fully by pyridine. Co-adsorption of 1:1 methanol: pyridine mixtures show spectra dominated by pyridine at 373 K. These results demonstrate that the weakly acidic methanol can be displaced easily by strongly adsorbing pyridine.

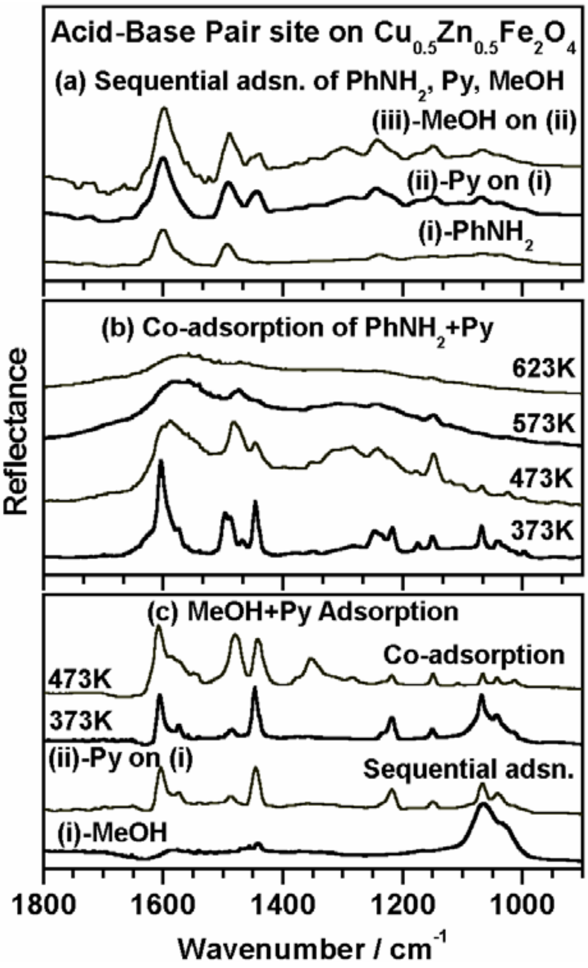

Figure 4.10: FTIR spectra recorded on $Cu_{0.5}Zn_{0.5}Fe_2O_4$ for competitive adsorption of reactants: (a) sequential adsorption of aniline, pyridine and then methanol at 373 K; (b) temperature dependence of co-adsorption of 1:1 ratio of aniline and pyridine and (c) sequential adsorption of methanol and pyridine at 373 K and co-adsorption of methanol and pyridine at 373 K and 473 K.

The weak methanol features in Figures 4.6, 4.7 and 4.8 (methanol:aniline) and 4.10c (methanol:pyridine) clearly support the aniline methylation reaction mechanism and justify the strong domination of aniline on the catalyst surface. The above results also indicates that despite a high methanol content in the aniline methylation feed (3:1, methanol:aniline), on the catalyst surface it may be close to a 1:1 ratio of methanol:aniline and also supports the reaction stoichiometry. However, larger amount of methanol in the reaction mixture was necessary due to weak interaction of methanol on the catalyst surface.

4.4 Conclusions

FTIR study of adsorbed reactants and products of aniline N-methylation on $Cu_{1-x}Zn_xFe_2O_4$ are described in the present work. Adsorption of methanol on $Cu_{1-x}Zn_xFe_2O_4$ indicates a dissociative chemisorption as methoxy species on catalyst surface at 373 K. As the temperature is increased, oxidation of methoxy species to formaldehyde to dioxymethylene to formate species is observed and above 573 K complete oxidation takes place to CO, CO_2 and H_2. Methoxy and formate species are comparatively reactive on Cu-containing samples due to the presence of easily reducible Cu^{2+} ions.

Adsorption of aniline on $Cu_{1-x}Zn_xFe_2O_4$ indicates its molecular adsorption through N-atom on an acid-base pair site. However, above 373 K N-H bond breaks and aniline chemisorbed strongly on the catalyst surface. Chemisorbed aniline molecules are on the Lewis acid sites with phenyl ring perpendicular to the plane of the catalyst surface. Phenyl ring of aniline and NMA also interacts in a very similar manner and the out of place C-H bending vibrations are observed supporting this point. However, for DMA and o-toluidine a very weak or no C-H bending vibrations are seen indicating that they interact fairly parallel to the plane of the oxide. Also it is found that NMA formation from the reaction mixture at 473 K on the catalyst surface and its desorption above 473 K indicates a desorption limited kinetics. High catalytic activity observed on $x = 0.5$ is apparently due to well-separated Cu^{2+} sites by Zn and hints that Zn acts as an '*active spacer*'.

It is found that methylation of aniline is initiated by the protonation of methanol with aid of a Lewis acid-base pair. The protonation of methanol occurs on the oxides by accepting protons released from the adsorbed aniline and to form the N-methylated products. Thus the active center for the methylation is an acid-base pair site. This mechanism is further supported by the IR studies of competitive adsorption of reactants with acidity probe molecule pyridine.

4.5 References

1. R. Schlogl, Angew. Chem. Int. Ed. 32 (1993) 381.
2. J. W. Niemantsverdiet, Spectroscopy in Catalysis, VCH, Weinheim. (1995) p. 1-284.
3. G. Ertl, H. Knozinger, J. Weitkamp, Handbook of Heterogenous Catalysis, Vol. 2, Wiley-VCH, Wieheim. (1997) p. 427-770.
4. J. A. Lercher, V. A. Veefkind, K. Fajerwerg, Vibrational. Spect. 19 (1999) 107.
5. I. Ivanova, E. B. Pomakhina, A. I. Rebrov, M. Hunger, Y. G. Kolyagin, J. Weitkamp, J. Catal. 203 (2001) 375.
6. G. Mirth, J. A. Lercher, J. Catal. 132 (1991) 244.
7. M. Hunger, J. Weitkamp, Angew. Chem. Int. Ed. 40 (2001) 2954.
8. A. Bruckner, Cata. Rev. 45 (2003) 97.
9. T. Mathew, M. Vijayaraj, S. Pai, B. B. Tope, S. G. Hegde, B. S. Rao, C. S. Gopinath, J. Catal. 227 (2004) 175.
10. G. Busca, V. Lorenzelli, J. Catal. 66 (1980) 155.
11. G. Busca, A. S. Elmi, P. Forzatti, J. Phys. Chem. 97 (1987) 5263.
12. G. Busca, V. Lorenzelli, Mater. Chem. 5 (1980) 213.
13. The Aldrich Library of FTIR Spectra, Vol. 2, II ed., Aldrich, Wisconsin, U.S.A., Spectrum No. 24228-4 (1997) p. 2024A.
14. D. R. Taylor, K. H. Ludlum, J. Phys. Chem. 76 (1972) 2882.
15. S. Scire, C. Crisafulli, R. Maggiore, S. Minico, S. Galvagno, Appl. Surf. Sci. 93 (1996) 309.
16. M. Tanaka, S. Ogaswara, J. Catal. 25 (1972) 111.
17. J. C. Evans, Spectrochim. Acta 16 (1960) 428.
18. T. Mathew, B. B. Tope, N. R. Shiju, S. G. Hegde, B. S. Rao, C. S. Gopinath, Phys. Chem. Chem. Phys. 4 (2002) 4260.
19. K. Tanabe, M. Misono, Y. Ono, H. Hattori, Stud. Surf. Sci. Catal. **51** (1989) 12.

Chapter 5: Photoemission studies on $Cu_{1-x}Zn_xFe_2O_4$

5.1 Introduction

The surface structure, chemical composition and electronic properties of the catalyst play prime role in determining the course of the reaction and catalytic activity. Since the first step in heterogeneous catalysis is the adsorption of reactants on the catalyst surface, which is followed by the reaction of the chemisorbed molecules and desorption of the products. Hence, understanding the nature of the solid surfaces will help to derive the structure activity relation. Very detailed idea about the surface structure, chemical composition and electronic properties of the surfaces are explored with ease due to the developments in surface science techniques. The developments in ultra high vacuum (UHV) techniques have facilitated the surface catalyst characterization techniques to a great extent. XPS and XAES are most powerful surface techniques employed quite often to understand the electronic structure details, oxidation state of the surface exposed elements, surface chemical compositions [1-3].

XPS and XAES investigations on fresh and spent $Cu_{1-x}Zn_xFe_2O_4$ catalysts were carried out in detail to understand the role of metal ions on aniline N-methylation. The changes in oxidation state of metal ions and the associated changes in electronic interaction, before and after the reaction were also investigated. The spent catalysts after aniline N-methylation at 573 K for 4h with 3:1:1 feed composition of CH_3OH:$PhNH_2$:H_2O, WHSV=3.58 h^{-1} was taken for the analysis. A careful comparison of aniline conversion data (Figure 3.3, Chapter 3) on all the catalyst compositions indicates the onset of decrease in activity starts at TOS = 4-5 h, except on x = 0.5. XRD of spent catalysts (x = 0.05 and 0.25) shows Cu^0 formation after TOS = 8h. Further, analysis of the spent catalysts at TOS >8h shows high coke content, except on x = 0.5 and provides no significant new information. Hence an analysis of the spent, but still active, catalysts after 4h of reaction and a comparison amongst all of the catalysts could give a better indication of changes that occurred due to the reaction. The results from fresh and spent catalysts were compared to understand the associated changes in terms of surface composition and changes in oxidation state of metal ions, Cu, Zn and Fe. The structural and electronic properties of the catalysts and the interaction between the metal ions were highlighted. XRD, surface area and TPR (temperature programmed reduction) results are also presented to reveal the changes in bulk properties of the fresh and spent catalysts and to substantiate the conclusion derived from photoemission studies.

5.2 Results

5.2.1 XRD and surface area

XRD of the fresh and spent $Cu_{1-x}Zn_xFe_2O_4$ (x = 0.05, 0.25, 0.5 0.75 and 1) catalysts are shown in Figure 5.1.

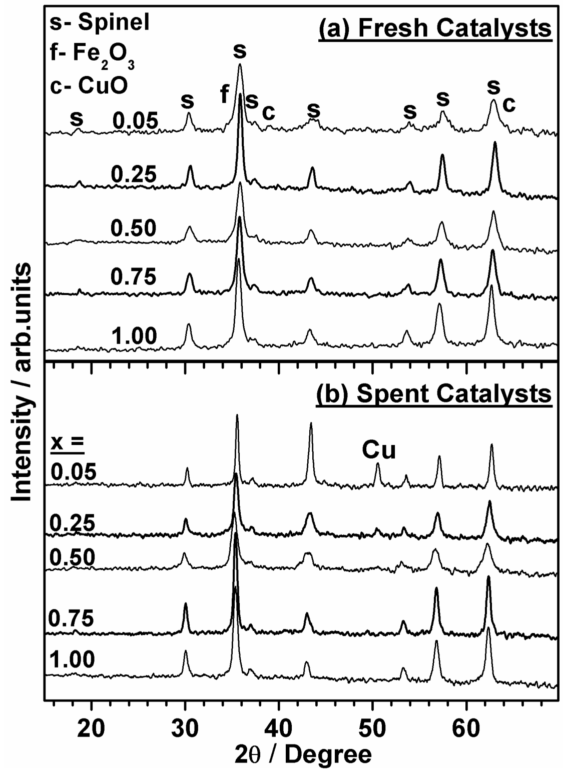

Figure 5.1: X-ray diffractogram of fresh and spent $Cu_{1-x}Zn_xFe_2O_4$ catalysts. XRD from spent catalysts are obtained after aniline methylation at 573 K for 8h with 3:1:1 composition of methanol:aniline:water. Note the metallic Cu is observed only for x = 0.05 and 0.25.

The spent catalysts reflections are sharp and intense compared to the fresh ones. Peaks corresponding to metallic copper (Cu^0) is observed only for x = 0.05 and 0.25 compositions. This indicates the reductive reaction conditions after a time on stream (TOS) for 8h. However, with other catalyst compositions no Cu^0 is observed. An appreciable increase in the crystallite size of the spent catalysts is observed as shown in Table 5.1, except for x = 0.5, hints to some sintering effect under the reaction conditions. No significant changes in the XRD pattern of fresh and spent $ZnFe_2O_4$ are observed and it is to be noted that hardly any catalytic activity observed with x = 1. There was a decrease in surface area for all of the spent catalysts, after reaction with methanol:aniline:water (3:1:1) at 573 K for 8h, due to the carbon deposition compared to fresh catalysts. However, no significant decrease in the surface area was observed for x = 0.5 system. A decrease in micro pore volume of spent catalysts also reveals the carbon deposition on spent catalysts.

Table 5.1:Physical and Textural properties of fresh and spent $Cu_{1-x}Zn_xFe_2O_4$ catalysts.

x	Crystallite Size [a] Spent (Fresh) [b] (nm)	Lattice Constant ‘a’ (Å) Spent (Fresh)	S_{BET} (m^2/g) Spent (Fresh)	Pore Volume (cm^3/g) 10^{-2} Spent (Fresh)
0.05	23.4 (10.0)	8.3723 (8.3459)	16.0 (23.0)	6.6 (9.5)
0.25	19.5 (15.9)	8.3946 (8.4090)	34.0 (45.2)	6.5 (7.3)
0.5	12.1 (10.7)	8.4133 (8.4052)	41.0 (49.3)	11.1 (13.6)
0.75	19.5 (11.7)	8.4153 (8.4150)	22.0 (42.0)	3.8 (12.3)
1	16.0 (13.0)	8.4117 (8.4180)	28.0 (35.0)	7.5 (12.5)

[a] Obtained from Debye-Scherer analysis.

[b] Spent catalysts after aniline N-methylation at 573 K with 3:1:1, feed composition of methanol:aniline:water for 8h.

5.2.2 XPS analysis

5.2.2.1 O 1s Core level

O1s spectra recorded before and after *in situ* surface cleaning gives the details of atmospheric degradation on the surface of solids if any [4-6]. Figure 5.2 shows O 1s core level spectra recorded before and after *in situ* scraping for $Cu_{0.5}Zn_{0.5}Fe_2O_4$. A shoulder clearly visible on the unscraped surface at a binding energy, 531.2 eV; nonetheless, the same almost disappears after a thorough scraping of the surface in the vacuum chamber and a very significant increase in O 1s intensity is also observed.

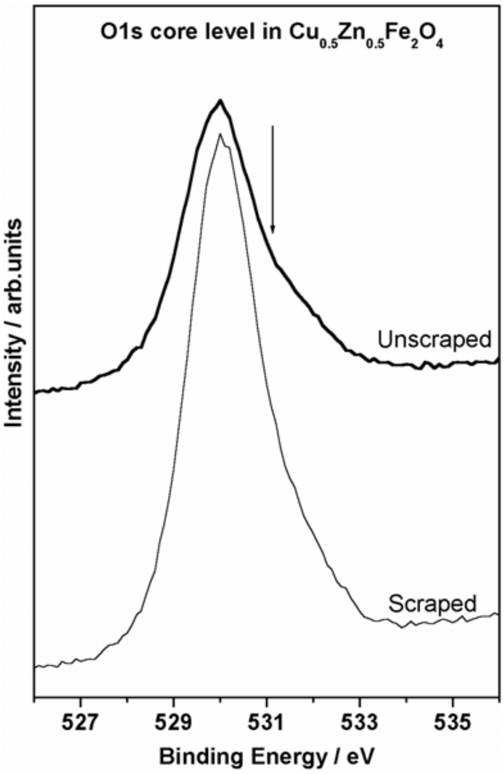

Figure 5.2: O 1s core level photoemission spectra from $Cu_{0.5}Zn_{0.5}Fe_2O_4$ catalyst without scraping and in situ scraped surfaces. Note a large decrease in the shoulder intensity around 531 eV, indicated by an arrow, demonstrates the atmospheric degradation that is limited to surface.

The main peak became more symmetrical and does not shift after scraping, as observed at 530 eV. This main peak is attributed to oxide ions in the spinel phase and the shoulder accompanying the main peak on unscraped surface is due to impurities such as OH^- and CO_3^{2-} species due to atmospheric degradation. The binding energy difference between the oxygen species that are associated with Fe, Cu and Zn might be small and hence they overlap to a great extent and are difficult to resolve under the present experimental conditions. No considerable difference is observed on the BE of the O 1s peak at different compositions. XPS results on fresh catalysts in the following sections are taken after thorough scraping. However, spent catalysts are analyzed in the powder form as used in the reactions.

5.2.2.2 Cu 2p core level and Cu-$L_3M_{45}M_{45}$

Cu 2p core level photoemission spectra from calcined and spent $Cu_{1-x}Zn_xFe_2O_4$ catalysts are shown in Figure 5.3. Table 5.2 summarizes the binding energy and FWHM (full width at half maximum) values from Cu $2p_{3/2}$ core levels. All calcined samples exhibit Cu $2p_{3/2}$ main line at 934.2±0.2 eV with a FWHM = 3 eV indicating the electron density on Cu remains the same and irrespective of the amount of Zn present. Good satellite intensity (I_s) is observed around 942 eV for all of the x values, indicating the existence of Cu^{2+} ions. The intensity ratio between satellite and main line (I_s/I_m) is 0.45 – 0.55 in all cases (Figure 5.3c), which is very close to that of pure CuO [7-9].

Table 5.2: XPS Cu $2p_{3/2}$ parameters from Fresh and spent $Cu_{1-x}Zn_xFe_2O_4$ catalysts

x	BE of Cu $2p_{3/2}$ (FWHM) eV	
	Fresh	Spent
0.05	934.1 (3.0)	932.1, 933.8 (4.0)
0.25	934.4 (3.0)	932.2, 933.5 (4.1)
0.50	934.2 (3.0)	932.1 934.1 (3.8)
0.75	934.4 (3.0)	932.2, 933.9 (3.5)

XPS results of Cu $2p_{3/2}$ core level from spent catalysts are interesting and new features are seen compared to fresh catalysts. Considerably large broadening (FWHM = 4 eV) was observed with satellites for x = 0.5 and 0.75; however a relatively sharp feature at lower BE with a shoulder on the higher BE and weak I_s were observed for x = 0.05 and 0.25. A deconvolution using peak fitting software [10], shown for x = 0.5 (Figure 5.2b and Table

5.2), reveals the contribution from a new peak at lower BE (932.2 eV) by reduced Cu-species. For x = 0.05 and 0.25 the I_s at higher BE appeared weak. An important point to be noted is the partial reduction of Cu^{2+} ions during the course of the reaction. Nonetheless the extent of reduction decreases with increasing Zn concentration.

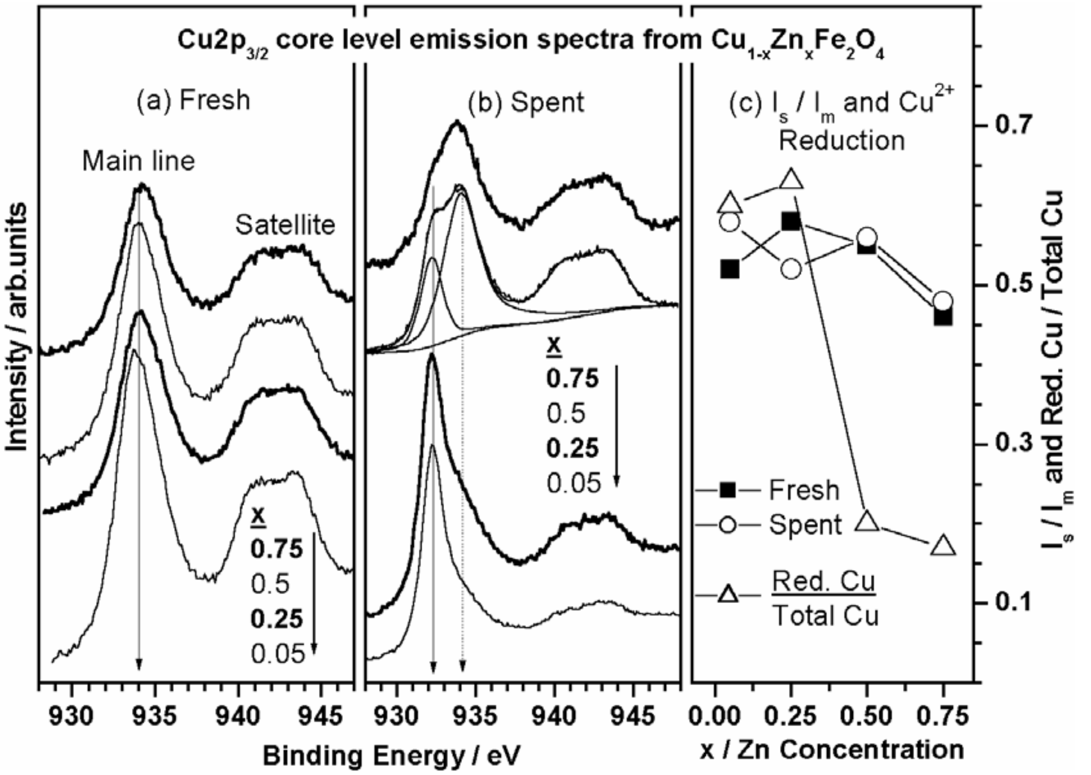

Figure 5.3: Cu $2p_{3/2}$ core level photoemission spectra from (a) fresh and (b) spent $Cu_{1-x}Zn_xFe_2O_4$ catalysts. Cu $2p_{3/2}$ core level from x = 0.5 (spent) spectrum was deconvoluted to show the presence of reduced Cu-species. (c) I_s/I_m for the fresh and spent catalysts and the ratio of reduced Cu-species to that of total Cu on spent catalyst. Note the marked decrease in the reducibility of copper for x = 0.5 and 0.75 compositions.

The I_s/I_m of fresh and spent catalysts and the reducibility of Cu calculated as the percentage of reduced Cu species to total Cu content is given in Figure 5.3c. This reducibility shows a sudden decrease from x = 0.05/0.25 to x = 0.5/0.75. It is apparent that the large amount of Zn prevents the reduction of Cu^{2+}. I_s/I_m of fresh and spent catalyst systems are very close to each other indicating the nature of unreduced Cu^{2+} remains the same.

Reduced Cu-species (Cu^0 and Cu^+) cannot be distinguished by XPS, since they appear at the same BE without any satellite features. Nevertheless, the valence states of reduced Cu species are easily distinguished by employing XAES, since the Cu^+ and Cu^0- $L_3M_{45}M_{45}$ (LMM) appears at around 916.5 and 918.5 eV, respectively [11-13]. The Cu - LMM Auger spectra of calcined and spent catalysts are given in Figure 5.4, and the results are summarized in Table 5.3.

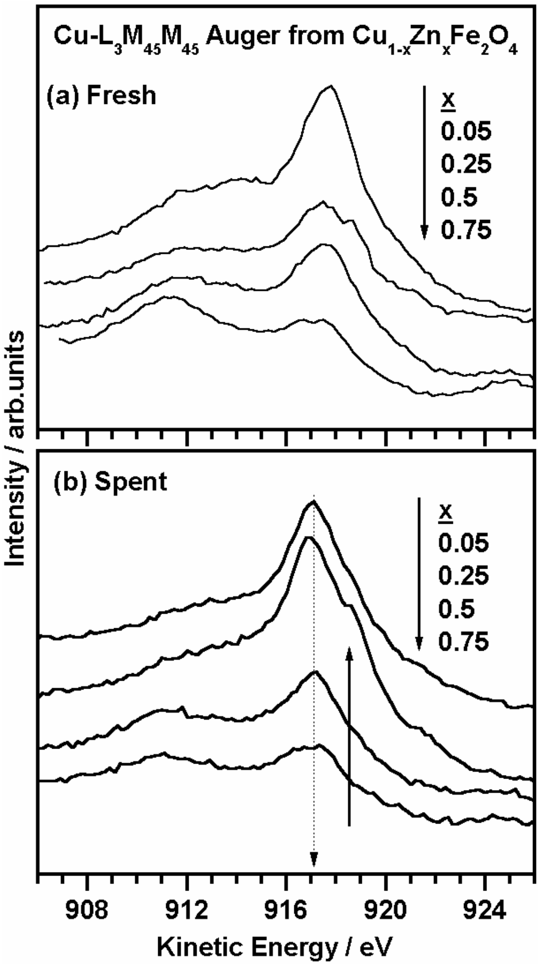

Figure 5.4: Cu $L_3M_{45}M_{45}$ Auger spectra from $Cu_{1-x}Zn_xFe_2O_4$, (a) Fresh and (b) Spent catalyst.

It is observed that fresh catalysts with x = 0.5 exhibit LMM line at a KE of 917.7 eV that are very close to that of CuO at 917.6 eV [11]. However, on other calcined catalysts the above value decreases up to 917.1 eV. On spent catalyst of x = 0.05 and 0.25, the Cu-LMM transition can be observed with relatively sharp peak at 917.0 eV, which is intermediate between Cu_2O and CuO and a shoulder at 918.5 eV, typical of Cu^0. It is in line with the XRD results, which shows metallic Cu. It is to be noted here that the Cu^0 on the surface can get oxidized easily to Cu_2O in the atmosphere and this could be a reason for the above intermediate KE at 917 eV. However, x = 0.5 and 0.75 exhibit a broad peak structure at high KE, 917.2 eV. It is to be noted that the fresh catalysts also exhibit a single peak around 917.4 ±0.2 eV, in this region. This clearly indicates an increasing contribution of Cu^{2+} at higher x values. However, the broadening indicates the contribution of Cu^+ species at low KE.

Table 5.3: Auger Parameters from Fresh and spent $Cu_{1-x}Zn_xFe_2O_4$

x	KE of Cu LMM		α' (eV)	
	Fresh	Spent	Fresh	Spent
0.05	917.7	918.6, 917.0	1851.8	1850.7, 1850.8,
0.25	917.5	918.5, 917.0	1851.9	1850.7, 1850.5
0.50	917.5	917.2	1851.7	1849.3, 1851.3
0.75	917.1	916.5, 917.3	1851.5	1848.7, 1851.2

Auger parameter (α') has generally been used to further confirm the chemical state of Cu [11,14]. The Auger parameter is defined as $\alpha' = E_B + E_K$ where, E_B is the BE of the Cu $2p_{3/2}$ core level and E_K is the KE of the Cu LMM Auger electron. α' calculated for spent catalysts (Table 5.3) is 1851.2 eV for x = 0.5 and 0.75 indicating the major contribution of Cu^{2+}. Overall, the large extent of reduction in the form of Cu (and some Cu^+) is clear on x = 0.05 and 0.25 and limited reduction to Cu^+ along with majority of Cu^{2+} on x = 0.5 and 0.75.

5.2.2.3 Zn 2p ore level and Zn-$L_3M_{45}M_{45}$

The Zn $2p_{3/2}$ core level spectra and Zn - $L_3M_{45}M_{45}$ Auger spectra are given in Figure 5.5 for fresh and spent catalysts. Zn-LMM results from spent catalyst are given along with calcined catalyst (x = 0.5) for comparison.

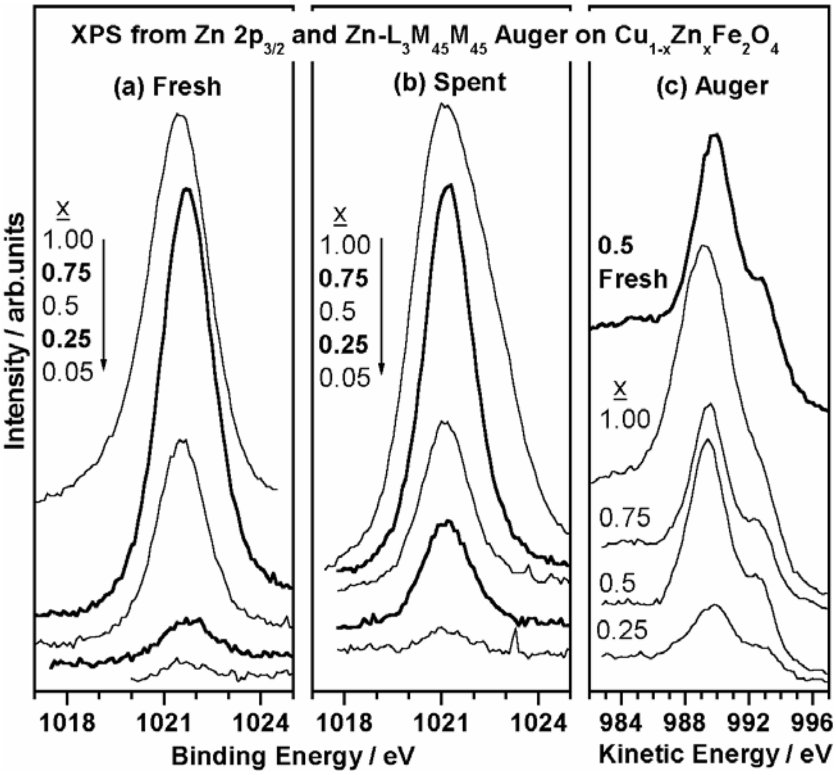

Figure 5.5: Zn $2p_{3/2}$ core level photoemission spectra from (a) fresh and (b) spent $Cu_{1-x}Zn_xFe_2O_4$ catalysts. (c) Zn-LMM spectra from spent $Cu_{1-x}Zn_xFe_2O_4$ catalysts. Note the difference in stacking on panel b and a high intensity feature for x = 0.5 and a broadening for x = 1.

The BE and FWHM of Zn $2p_{3/2}$ core level are summarized in Table 5.4. All of the fresh catalysts exhibit a peak centering at 1021.6±0.1 eV, which is very close to the BE of ZnO at 1022±0.2 eV [11]. Zn $2p_{3/2}$ peak appeared at 1021.2 eV for all spent catalysts compositions that show a significant shift in the BE compared to that of fresh catalysts. This also hints that there could be significant but similar changes occurring under reaction conditions. There is a possibility of contribution from two types of Zn species on $ZnFe_2O_4$ since a noticeable increase in FWHM was observed. However, Zn-LMM XAES of all spent catalysts show a main line KE feature at around 989.5 eV, which is due to Zn^{2+} since metallic Zn-LMM Auger line appears at ~992 eV [15,16].

The α' calculated for Zn^{2+} (2010.1-2011 eV) on spent catalyst also confirms the existence of Zn^{2+}, and not that of metallic Zn (2014 eV) [11]. However, α' is different for fresh x = 0.5 catalyst and observed at 2011.5 eV. Shift in the BE of Zn 2p might be due to a change in environment around Zn on spent catalysts due to the partial reduction of other metal ions.

Table 5.4: Binding energy and FWHM of Zn $2p_{3/2}$ core level on fresh and spent $Cu_{1-x}Zn_xFe_2O_4$ catalysts.

x	BE of Zn $2p_{3/2}$ (FWHM) eV	
	Fresh	Spent
1	1021.4 (2.3)	1021.1 (2.9)
0.75	1021.7 (1.9)	1021.1 (1.8)
0.5	1021.5 (1.8)	1021.2 (1.8)
0.25	1021.7 (1.8)	1021.2 (1.8)
0.05	1021.5 (2.3)	1021.1 (2.7)

5.2.2.4. Fe 2p core level and Fe-$L_3M_{45}M_{45}$

Photoemission spectra of Fe $2p_{3/2}$ core level are given in Fig. 5.6a and 5.6b for fresh and spent catalysts, respectively. The following important points to be noted: (i) A clear satellite around 719 eV with $2p_{3/2}$ main line centering at 711.2 eV is observed due to the predominant Fe^{3+} on fresh catalysts; however, weak I_s was observed on spent catalysts with $x \leq 0.5$ (ii) Spent catalysts display a shoulder at 709.7 eV, characteristic of Fe^{2+} species, for catalysts with $x \leq 0.5$ [17,18]. A peak deconvolution for x = 0.5 clearly shows the contribution from Fe^{2+}. Intensity of Fe^{2+} decreases with increasing bulk Zn-content and no reduction was observed on $ZnFe_2O_4$.

Fe-$L_3M_{45}M_{45}$ spectra for catalysts with $x \leq 0.5$ are given in Figure 5.6c. The spent catalysts spectra are normalized to fresh catalysts spectra for better presentation. Fresh catalysts spectra are similar with peak centered at KE 701.5 eV and no significant difference is observed. A considerable change is clear on the spent catalysts, especially, with x = 0.0.5

and 0.25. A shoulder observed at KE 698 eV (dotted arrow) is ascribed to Fe^{2+}; however, the intensity of this feature is less at x = 0.5. Fe-$L_3M_{45}M_{45}$ result indicates the partial reduction of Fe^{3+} and the extent of reduction decreases with increasing x, as observed with Fe 2p core level.

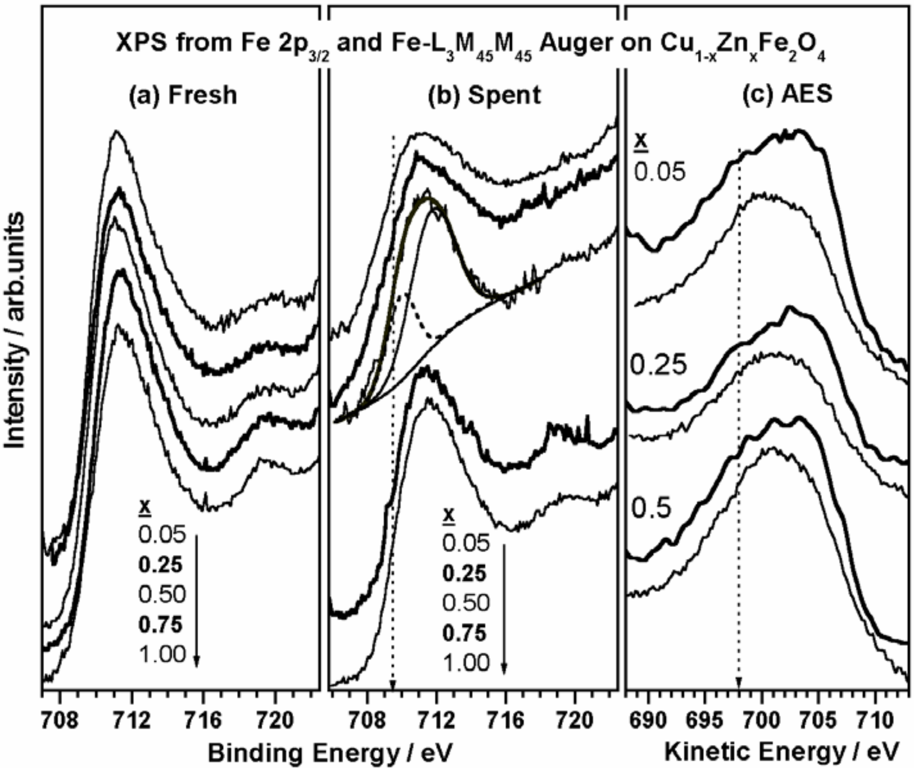

Figure 5.6: Fe 2p core level XPS of (a) fresh and (b) spent $Cu_{1-x}Zn_xFe_2O_4$ catalysts. A shoulder seen below 710 eV on spent catalysts (dotted line) indicates a partial reduction of iron. Deconvolution of Fe $2p_{3/2}$ peak for x = 0.5 demonstrates Fe^{2+} and Fe^{3+} on spent catalysts. (c) Fe-LMM Auger spectra of selected fresh and spent catalysts.

5.2.2.5 Valence band photoemission

XPS spectra of the valence band (VB) region obtained from all of the fresh and spent $Cu_{1-x}Zn_xFe_2O_4$ catalysts are shown in Figure 5.7. The main VB appears <8 eV have contribution from 3d bands of Cu and Fe and O 2p bands. At hν = 1253.6 eV employed in these experiments, the photo ionization cross-section (σ) value (Cu 3d = 0.021, Fe 3d = 0.0045 and O 2p = 0.0005 Mb) [19] is the dominating factor in deciding the spectral intensity. The above data suggest that Cu 3d should make large contributions to the VB and the contribution from O 2p is negligible. The VB assignments are straightforward from the intensity and the BE of the bands. High-intensity VB observed around 4 eV corresponds to Cu 3d, and its intensity decreases with increasing x value on fresh catalysts. A low intensity broad band observed between 4-7.5 eV is due to the contribution from Fe 3d and O 2p bands. A completely filled Zn 3d band is observed, far away from the main VB, at 9.4 eV and its intensity increases linearly with increasing x value.

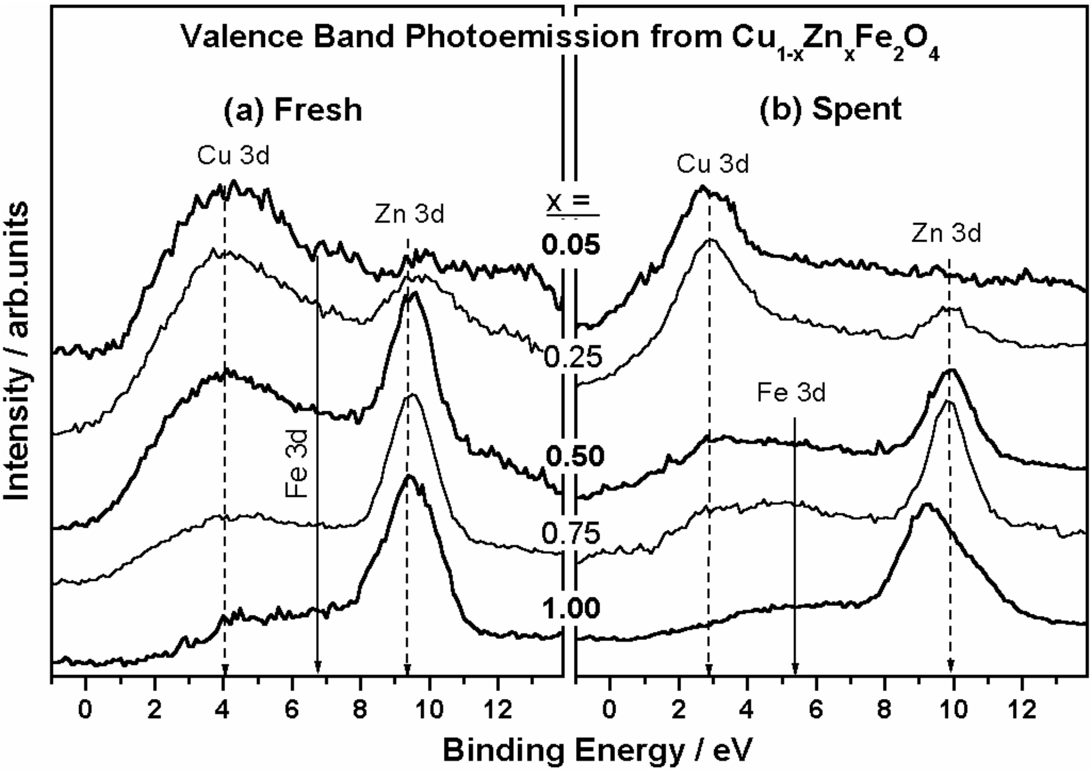

Figure 5.7: Valence band XPS of (a) fresh and (b) spent $Cu_{1-x}Zn_xFe_2O_4$ catalysts. Note a decrease (increase) in the BE of Cu 3d (Zn 3d) level on spent catalysts compared to fresh, except x = 1.

Significant changes observed from core levels of spent catalysts are reflected strongly in the VB spectra too. The main observations are: (i) Cu 3d band shifts to lower BE by 1 eV (dotted arrow at 3 eV) accompanied by a narrowing of the band on x = 0.05 and 0.25, where as for x = 0.5 and 0.75 systems Cu 3d band appears very broad and centered at 4 eV. (ii) A shift of about 1 eV is observed for Fe 3d level, which is very clearly seen. (iii) Zn 3d band too shifts marginally to higher BE (dotted arrow at 10 eV) for $0.25 \leq x \geq 0.75$ systems, whereas it remains centered at 9.2 eV with an asymmetric broadening for $ZnFe_2O_4$. The above points suggest that on spent catalysts the changes in Cu and Fe VB are significant. However, a comparison of BE of Zn 3d band on fresh (9.4 eV) and spent catalysts (10 eV) suggests that Zn might be in a significantly different environment, due to the partially reduced metal ions on spent catalysts. However, the energy gap between Cu 3d (or Fe 3d) and Zn 3d increases by not less than 1 eV, indicating the electronic interactions, if any, becomes weaker on spent catalysts compared to fresh catalysts.

5.2.2.6 Surface Composition of Fresh and Spent $Cu_{1-x}Zn_xFe_2O_4$

Metal ions ratio on the surface of all the catalyst systems is given in Table 5.5. This helps in understanding the metal ions distribution and their heterogeneity on the surfaces that directly influences the catalytic activity. A linear relationship exists between the surface metal ions content with the nominal metal ion input amount (x) on all of the fresh catalysts (Table 5.5). In contrast, a dramatic change in surface compositions was observed on spent catalysts. A high Cu/Fe (>1) was found on spent catalysts with x = 0.05 and 0.25, where as x = 0.5 and 0.75 systems show Cu/Fe<1. x= 0.5 spent catalyst after 24 h on TOS was also subjected to XPS study, due to its stable catalytic activity. Cu/Fe ratio decreases from 0.72 (TOS = 4h) to 0.57 (TOS = 24h) on x = 0.5 spent catalyst.

An appreciable increase in Zn/Fe ratio was observed from fresh (0.20) to spent (0.58) catalyst with x = 0.5 after 4h TOS; nonetheless, it decreases to 0.40 after 24h TOS. Both Cu/Fe and Zn/Fe ratio decreases for x = 0.5 system at 24 h after initial hours (4h) of the reaction indicating a continuous change in the metal ions concentration on the surface during the transient reaction period of first 12 h and then it stabilizes. Further, (Cu+Zn)/Fe ratio of <1 for all the fresh samples reveals somewhat Fe-dominated surface character before the reaction. Nonetheless, (Cu+Zn)/Fe for all spent catalysts increased to >1 hints an enrichment of Cu and/or Zn on the surface due to reaction and the role of Fe decreases substantially.

Table 5.5: Surface atomic ratio calculated from photoemission studies on fresh and spent $Cu_{1-x}Zn_xFe_2O_4$ catalysts

x	Fresh				Spent[a]						
	Cu/Zn	Cu/Fe	Zn/Fe	(Cu+Zn)/Fe	Cu/Zn	Cu/Fe	Zn/Fe	(Cu+Zn)/Fe	Cu/C	Zn/C	Fe/C
0.05	68.55	0.86	0.01	0.87	34.2	1.25	0.04	1.29	0.35	0.01	0.28
0.25	13.43	0.74	0.05	0.79	7.42	1.47	0.20	1.67	0.50	0.07	0.34
0.5	2.81	0.54	0.20	0.73	1.25	0.72	0.58	1.30	0.48	0.38	0.66
0.5[b]	-	-	-	-	1.48	0.57	0.40	0.97	0.55	0.37	0.96
0.75	0.79	0.37	0.47	0.84	1.38	0.62	0.45	1.10	0.17	0.12	0.27
1	-	-	1.00	1.00	-	-	1.20	1.20	-	0.77	0.64

[a] Spent Catalyst collected at TOS = 4 h

[b] Spent Catalyst collected at TOS = 24 h

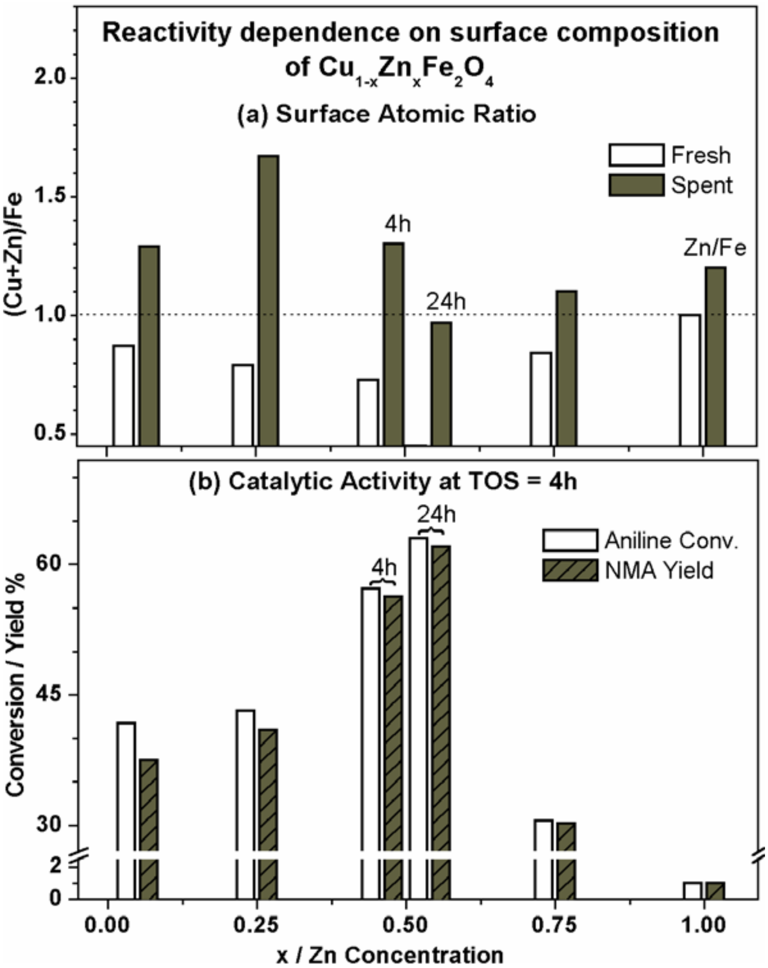

Figure 5.8: Comparison of (a) atomic ratio of Cu+Zn/Fe for all fresh and spent catalyst compositions and (b) aniline conversion and NMA selectivity on $Cu_{1-x}Zn_xFe_2O_4$ catalysts. Note the Cu+Zn/Fe ~1 after 24 h of reaction on x = 0.5 and stable catalytic activity associated with it.

Cu contribution is major to (Cu+Zn)/Fe ratio on all of the spent catalysts, as evident from Cu/Fe ratio for $x \leq 0.75$. After TOS = 24h, (Cu+Zn)/Fe ratio comes close to unity (0.97) on the surface of x = 0.5 indicating an optimum heterogeneous distribution of all metal ions on the surface. A good amount of carbon deposition is also evident from the ratios between metal ions and carbon. However, carbon deposition is relatively less on x = 0.5 and 1. Interestingly, catalyst with x = 0.5, after 24h TOS, shows highest metal/C ratio than other compositions. High C and low Zn concentration were observed, as evident from Zn/C, on x = 0.05, 0.25 and 0.75, irrespective of bulk concentration. Figure 5.8 displays the (Cu+Zn)/Fe, (Zn/Fe for x = 1) ratio calculated from XPS results in the top panel (a) and aniline conversion with NMA yield for all the compositions in the bottom panel (b). Interestingly, when the (Cu+Zn)/Fe ratio is close to 1 (dotted line in Figure 5.8a), generally, the aniline conversion is reasonably good. This might be a reason why all the Cu-containing catalysts show a high conversion in the first few hours of the reaction. However, the ratio changes with time and at the onset of deactivation (TOS = 4h) the ratio reflects the state of the surface composition.

Clearly there is a redistribution of metal ions on the surface, as the reaction progresses on all the compositions. Although, a same (Cu+Zn)/Fe ratio was observed for x = 0.05 and 0.5 (TOS = 4h), the nature of Cu-species dramatically changes from dominantly Cu^{2+} on x = 0.5 to reduced Cu-species on x = 0.05. Further, an increase in the (Cu+Zn)/Fe ratio is almost entirely due to an increase in the Cu-content on x = 0.05 and this leads to Cu-agglomeration and sintering, as observed in XRD (Figure 5.1b). Although x = 0.75 spent catalyst shows the above atomic ratio to be 1.1, the amount of carbon deposition is high (Table 5.5) and hence the active metal content on the surface is low. However, somewhat stable activity observed with x = 0.75 correlates well with the (Cu+Zn)/Fe ratio close to 1.

These observations hint at the necessity of sufficient concentration of oxidized Cu^{2+} for sustainable alkylation activity. Only on x = 0.5 (TOS = 24h) the (Cu+Zn)/Fe ratio was maintained at 1 and hence the extended catalytic activity was observed. It is clear that not a single metal ion, but the heterogeneity of the surface, specifically a combination of all three metal ions, brings out the desired reactivity with stability.

5.3 Discussion

5.3.1 Electronic structure and distribution of metal ions on $Cu_{1-x}Zn_xFe_2O_4$

Spent catalysts show predominant spinel phase with small amount of Cu^0, on Cu-rich compositions, due to some reductive atmosphere under methylation conditions. Nonetheless, Cu^+ was observed in XPS on all of the compositions indicates the possibility that either the surface Cu^0 clusters are oxidized due to aerial oxidation or due to partial reduction of Cu^{2+}

ions due to reaction. However, coke deposition prevents the oxidation of metal species in the bulk and diffraction corresponds to Cu metal is seen in the XRD. This also indicates the inevitable structural change to some extent at $x = 0.05$; nevertheless, the Cu^{2+} reduction is observed at a less significant level for catalysts with $x > 0.25$ and as evident from the absence of metallic reflections in the XRD. Surface area decreases after the reaction for all the compositions (except $x = 0.5$), and is probably due to surface agglomeration of metal ions and/or deposition of coke on the surface as evident from the surface atomic composition results (Table 5.5). Decrease in surface area is prominent for $x = 0.05$, 0.25 and 0.75 systems and the deposited carbon content is also high. It is to be noted that an increase in crystallite size on spent catalysts lead to a decrease in surface area. Nevertheless, $x = 0.5$ composition alone retains its textural properties and there is no significant influence by the reaction on its structural integrity. This also hints the spinel can accommodate some amount of reduced metal ions without structural collapse.

Several discrepancies are observed between the fresh and the spent catalysts revealing the changes in the oxidation state of the metal ions that occurred under experimental conditions. The main points from the XPS results can be summarized here: (a) a decrease in the Cu^{2+} reducibility with increasing Zn-content, and (b) an unambiguous redistribution of metal ions on the surface of spent catalysts which depends on the catalyst compositions. As it is evident from the surface atomic ratio for better performing $x = 0.5$ spent catalyst, Cu/Fe ratio increases marginally with an increase in Zn/Fe ratio and indicates an optimum distribution of active Cu^{2+} surrounded by Zn and Fe. However, for Cu-rich compositions Cu/Fe ratio increases significantly, which indicates a high probability for agglomeration of Cu as the reaction proceeds and that leads to faster deactivation for these compositions. In contrast, on $x = 0.5$ system Zn content also increases that hinders the Cu aggregation and a value close to unity for Cu+Zn/Fe ratio perfectly supports that all the metal ions are separated sufficiently, so that no metal ion meets the similar ion in the near neighbor environment. This could be one of the reasons for the high and stable catalytic activity observed with x = 0.5. An increase in the Fe content was also seen (TOS = 24h for x = 0.5) on the surface in order to maintain the initial structural integrity of the catalytic system. The above observation might be due to reaction-induced change in surface composition in the first 12 h followed by a stable activity observed at least up to 60 h.

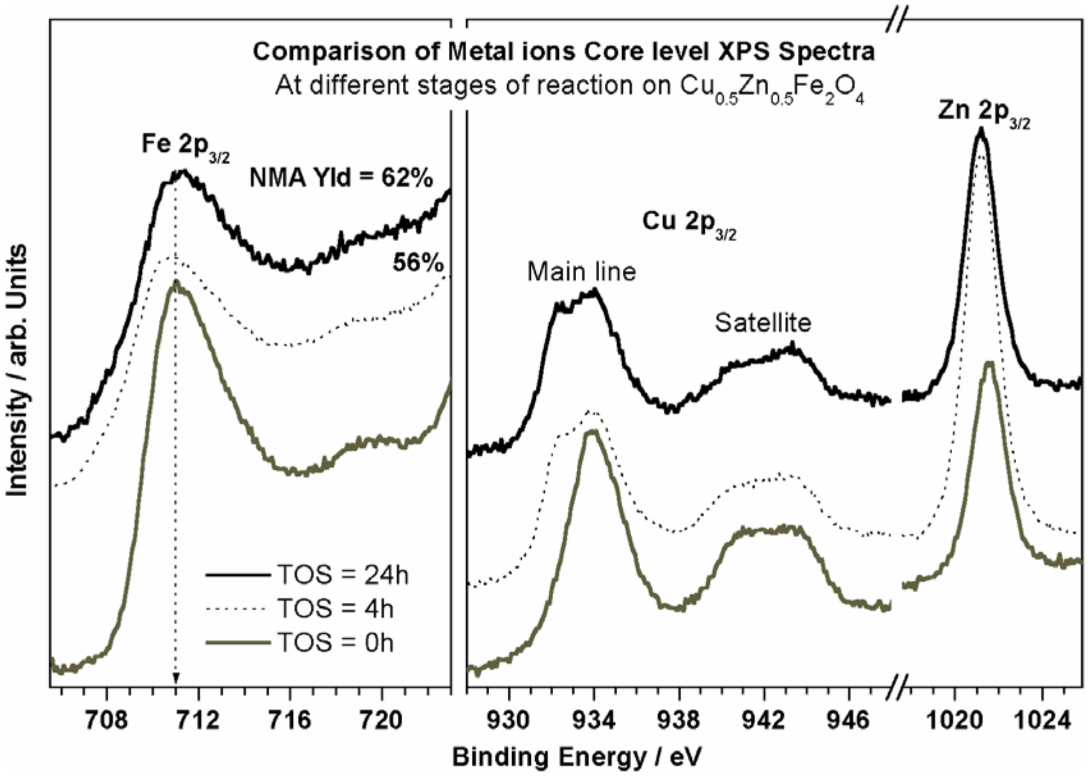

Figure 5.9: A comparison of Fe 2p, Cu 2p and Zn 2p core level features on fresh and after two different stages of reaction on $Cu_{0.5}Zn_{0.5}Fe_2O_4$ catalyst. Note a drastic change in the transition metal content accompanied with some reduction after different stages of reaction.

As shown in Cu 2p photoemission on x = 0.5 system at different TOS (Figure 5.9) the active Cu^{2+} and structural integrity of the system are retained even after 24h. Except for some Cu^{+} formation after the initial period of reaction, the overall Cu-content remains the same on the surface throughout the reaction. It is the change in Zn and Fe content on the surface, which keeps the average surface atomic composition constant and helps to maintain the activity for a longer period. This finding reiterates that it is the heterogeneity of all metal ions that decides the stability of the catalyst. Although (Cu+Zn)/Fe is close to unity on x = 0.75, the decreasing aniline conversion is mostly due to the very high C content and it reflects in the very low ratio of metal ions to C (Table 5.5).

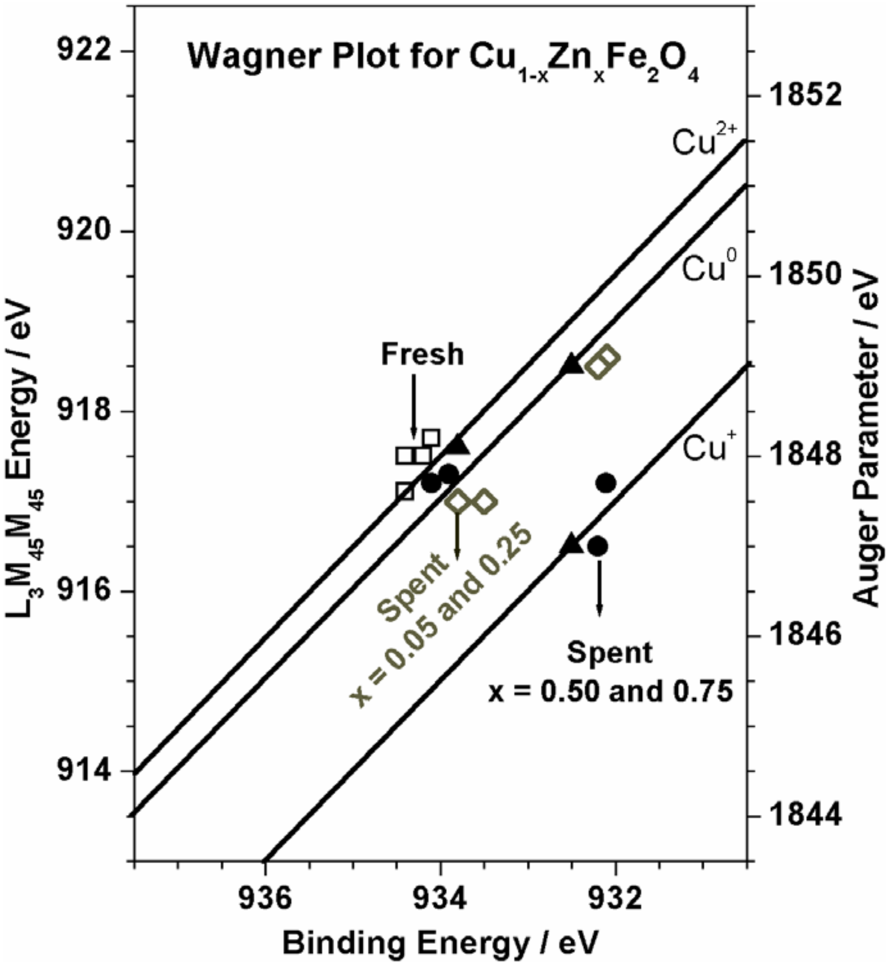

Figure 10: Wagner plot for $Cu_{1-x}Zn_xFe_2O_4$ catalysts from the Cu $2p_{3/2}$ core level and Auger spectral data. Data points for standard compounds (Cu, Cu_2O and CuO) are given by solid triangles and fresh catalyst by open squares. Spent catalysts with x = 0.05 and 0.25 composition indicated by open diamond and x = 0.5 and 0.75 by solid circles, respectively. The Auger parameter is described by solid straight line with a slope of –1. Nature of reduced Cu-species is dominantly Cu^0 on x = 0.05 and 0.25 and Cu^+ on x = 0.5 and 0.75.

Although XPS and XAES results were explained earlier, a Wagner plot [7,20] shown in Figure 5.10 makes the identification of the different reduced species easier. Here, the kinetic energy of Auger transition on the y-axis and the Cu $2p_{3/2}$ binding energy of the photoemission line on the x-axis in the negative direction, for all the catalysts are plotted. The data for Cu, Cu_2O and CuO reference samples [21] are also plotted in the same Figure 5.10.

The Auger parameters are described by solid straight line with a slope of –1. It is clear that Cu^{2+} in all of the fresh and the spent catalysts are similar to that of CuO. Indeed, x = 0.5 and 0.75 resemble more closer to CuO than x = 0.05 and 0.25. The nature of reduced species on x = 0.05/0.25 corresponds to that of Cu^0; however the same corresponds to Cu_2O-like species on x = 0.5 and 0.75.

5.3.2 Zn^{2+} - an 'active spacer' on catalyst and stabilizer towards reaction

XPS and XRD results in the present study reveal that Cu-rich systems, x = 0.05 and 0.25 exhibit a significant Cu^{2+} reduction and agglomeration due to the decomposition of methanol to reformate products and H_2 production. In contrast, at x = 1 no such dramatic changes are observed with Zn. However, at an intermediate composition (x = 0.5) the extent of Cu^{2+} reduction to metal is totally suppressed and the catalytic activity was maintained for a longer period of time. The large energy gap observed between Cu or Fe 3d and Zn 3d bands (Figure 5.7) suggests it can hardly have any electronic interaction. It is to be noted that there is no Fe^{3+} reduction to Fe or Fe_xC_y, as in the case of, closely related, $Cu_{1-x}Co_xFe_2O_4$ used for phenol ethylation [22]. Further, it is clear from the surface atomic composition results that both Cu and Zn content on the surface changes significantly for x = 0.5 system as the reaction proceeds in the first 12 hours. After that, almost a 1:1 combination of Cu and Zn is maintained on the catalyst surface. The change in surface atomic composition, a transient change in catalytic activity up to 12 h before it reaches a stable activity and a comparison of deactivation trend and surface atomic composition of other catalyst compositions clearly indicates the role of Zn as an 'active spacer' on $Cu_{0.5}Zn_{0.5}Fe_2O_4$ and prevents the reduction/agglomeration of Cu^{2+} under present experimental conditions. A considerable increase in the lattice constant for x = 0.5 (Table 5.1) supports the view that the lattice can accommodate Cu^+ ions to certain degree without structural collapse. As the role of Zn-spacer marginally increases and helps to maintain the catalytic activity in the present system, we termed it as *'active spacer'*, in contrast to the lower activity observed when any spacer is introduced in a catalytic system. Low aniline conversion at x = 1 changes dramatically with the addition of Cu at x = 0.5, demonstrating the prime importance of Cu in aniline methylation and combined effect of Cu + Zn in overall catalyst performance. It is called synergetic performance from Cu and Zn that play a major role in the aniline methylation and catalyst stability.

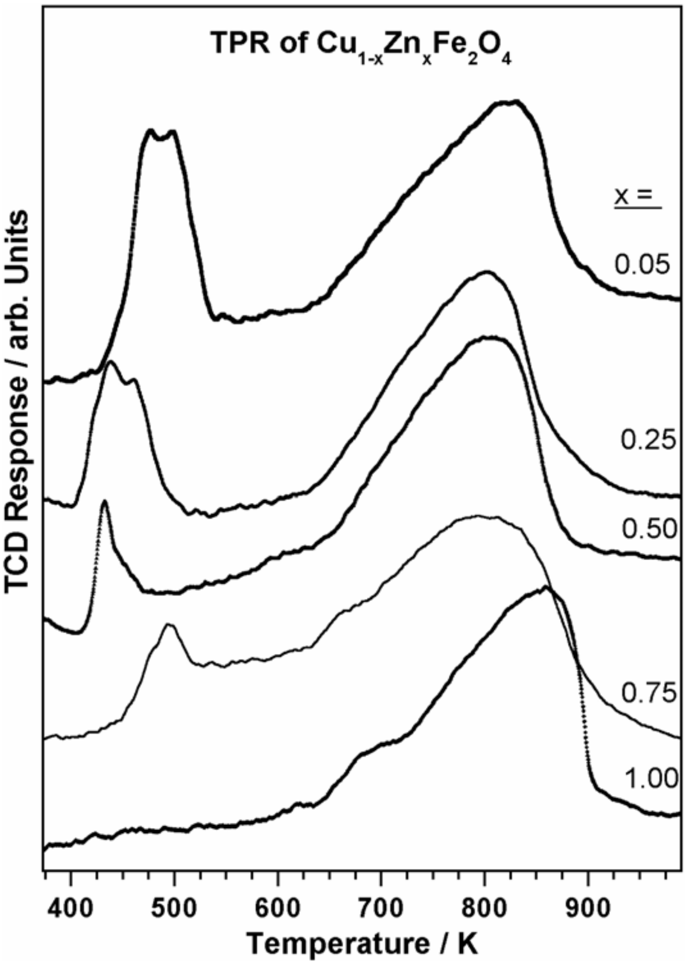

Figure 11: TPR profiles of $Cu_{1-x}Zn_xFe_2O_4$ catalysts measured with 5% H_2 in Argon, under a flow rate of 30 ml/min. at a heating rate of 5K/min. A continuous H_2 consumption between 525 and 650 K to be noted on x = 0.5 and 0.25.

A final support to the active spacer role in preventing the Cu^{2+} reduction is obtained from TPR experiments, shown in Figure 5.11. All the Cu-containing $Cu_{1-x}Zn_xFe_2O_4$ compositions clearly show a Cu-reduction peak around 473 K and Fe and Zn reduction features in a broad peak between 650 K and 900 K. Cu^{2+} reduction peak appearing around 475 and 500 K for x = 0.05 and 0.75 shifts to lower temperatures between 425 and 450 K for x = 0.25 and 0.5. It is to be mentioned here that a variety of Cu^{2+} reduction peaks were observed in mixed Cu-Zn-Al oxide system [23-25].

A careful analysis also reveals the amount of H_2 uptake decreases non-linearly with decreasing Cu-content. A quantitative analysis of x = 0.5 (0.05) results hints the amount of H_2 uptake in the temperature regime of 413 to 500 K (425-525 K) corresponds to Cu^{2+} to Cu^+ (Cu^{2+} to Cu^0) reduction. A further careful look at the x = 0.5 trace reveals a continuous H_2 uptake, at a lower level, between 523 K and 653 K. Indeed similar H_2 uptake pattern can be seen for x = 0.25 although at a still lower intensity level; however this feature is not observed on (Cu-rich) x = 0.05 composition indicating the complete reduction to Cu^0 at 525 K. This clearly supports the total Cu^{2+} reduction takes place only above 573 K on x = 0.5 composition due to the active spacer role of Zn. However a partial reduction to Cu^+ is clear as also observed in XPS.

5.4 Conclusions

Photoemission studies on aniline N-methylation catalysts $Cu_{1-x}Zn_xFe_2O_4$ have been carried out to address the changes in activity with catalyst composition and a structure-activity correlation. Fresh catalysts clearly indicate the existence of Cu^{2+}, Zn^{2+} and Fe^{3+} species. However, the spent catalysts show a composition dependent oxidation states. A significant reduction of Cu^{2+} to Cu is observed for $x \leq 0.25$. The above total reduction is fully suppressed on 0.5 and 0.75; however, a partial reduction of Cu^{2+} to Cu^+ and Fe^{3+} to Fe^{2+} observed to occur. The valence band shows a significant change in BE of 3d bands of Cu and

Fe on spent catalysts. Redistribution of cations on the spinel surface during reaction conditions is also evident from the surface composition analysis. Above redistribution of metal ions on the surface determines the course of the reaction. Presence of an almost equal amount of Cu and Zn on the surface is necessary for a longer TOS methylation activity on these spinel systems, in which Cu^{2+} is the active species for methylation and Zn^{2+} acts as an active spacer and stabilizer to decrease the extent of Cu^{2+} reduction and Cu agglomeration on the surface. It is the complete heterogeneity of the surface metal ions composition that helps for the stable catalytic activity and retention of the structural integrity of the catalyst.

5.5 References

1. A. M. Ellis, M. Feher, T. G. Wright, Electronic and Photoelectron Spectroscopy; Fundamentals and Case studies, Cambridge University Press, Cambridge, 2005.
2. S. Hufner, Photoelectron Spectroscopy, Springer-Verlag, Berlin, 1995.
3. T. A. Carlson, X-ray Photoelectron Spectroscopy, Dowden, Hutchison and Ross, Stroudsburg, PA, 1978.
4. C. S. Gopinath, S. Subramanian, M. Paranthaman, A. M. Herman, Phys. Rev. B 48 (1993) 15999.
5. C. S. Gopinath, S. Subramanian, P. S. Prabhu, M. S. R. Rao, G. V. S. Rao, Physica C, 218 (1993) 117.
6. T. Mathew, N. R. Shiju, K. Sreekumar, B. S. Rao, C. S. Gopinath, J. Catal. 210 (2002) 405.
7. S. Velu, K. Suzuki, H. Yoshida, T. Hattori, Phys. Chem. Chem. Phys. 4 (2002) 1990.
8. S. Velu, K. Suzuki, C. S. Gopinath, J. Phys. Chem. B 106 (2002) 12737.
9. S. Velu, K. Suzuki, M. Vijayaraj, S. Barman, C.S. Gopinath, Appl. Catal. B 55 (2004) 281.
10. http://www.hkbu.edu.hk/~csar/links.html.
11. G. Moretti, G. Fierro, M.L. Jacono, P. Porta, Surf. Interface. Anal. 14 (1989) 325; http://www.srdata.nist.gov/xps/
12. T. H. Fleish, G. Mains, J. Appl. Surf. Sci. 10 (1982) 51.
13. J. P. Espinos, J. Morale, A. Barranco, A. Caballero, J. P. Holgado, A. R. Gonzalez-Elipe, J. Phys. Chem. B 106 (2002) 6921.
14. F. Severino, J. L. Brito, J. Laine, J. L. G. Fierro, J. Catal. 177 (1998). 82.
15. Y. Okamoto, K. Fukino, T. Imanaka, S. Teranishi, J. Phys. Chem. B 87 (1983) 3741.
16. Y. Okamoto, K. Fukino, T. Imanaka, S. Teranishi, J. Phys. Chem. B 87 (1983) 3747.

17. P. Mills, J.L. Sullivan, J. Phys. D 16 (1983) 723.
18. T. Fujil, F.M.F. deGroot, G.A. Sawatzky, F.C. Voogt, T. Hibma, K. Okada, Phys. Rev B 59 (1999) 3295.
19. J.J. Yeh, I. Lindau, Atom. Data Nucl. Data Tables 32 (1985) 1.
20. Moretti, J. Electron Spectrosc. Relat. Phenom. 76 (1995) 365.
21. S. Poulston, P.M. Parlett, P. Stone, M. Bowker, Surf. Interface Anal. 24 (1996) 811.
22. T. Mathew, N.R. Shiju, V.V. Bokade, B.S. Rao, C.S. Gopinath, Cata. Lett. 94 (2004) 223.
23. S. Velu, K. Suzuki, M. Okazaki, M.P. Kapoor, T. Osaki, F. Ohashi, J. Catal. 194 (2000) 373.
24. S. Murcia-Mascaros, R.M. Navarro, L. Gomez-Sainero, U. Costantino, M. Nocchetti, J.L.G. Fierro, J. Catal. 198 (2001) 338.
25. M. Turco, G. Bagnasco, U. Costantino, F. Marmottini, T. Montanari, G. Ramis, G. Busca, J. Catal. 228 (2004) 43; and references there in.

Chapter 6: O-methylation of dihydroxybenzenes on MgO: Selective production of MP

6.1 Introduction

O-methylated dihydroxybenzenes (DHB) are important synthetic intermediates in the production of fine chemicals and pharmaceuticals. An introduction about methoxyphenols (MP) and a brief list of literature reports highlighting various catalysts and the reaction employed for the production of MP are given in Chapter 1. Selective catalytic production of MP from DHB is an interesting and challenging problem from the process as well as also from the kinetic point of view. Very few reports are available in the literature [1-16] about production of 2-MP from O-methylation of catechol. However, O-methylation of other two DHB, namely resorcinol and hydroquinone, to 3-MP and 4-MP, respectively has not been measured in detail. This chapter covers the O-methylation of all the three DHB with DMC as methylating agent on MgO and alkali ions (Li, K and Cs) promoted MgO. Selective production of MP was achieved with the above catalysts and the catalytic results were given and discussed.

6.2 Experimental

O-methylation of dihydroxybenzenes was carried out using 0.5 gm of MgO or alkali metal ions promoted MgO with particle around 25 mesh. The catalyst was activated *in situ* with a stream of air at 673 K for 2h for the complete decomposition of nitrate and hydroxide. After decomposition, the catalyst was cooled in a stream of N_2 (10 mL/min) and brought down to the desired reaction temperature. The reaction mixture (dihydroxybenzenes and dimethylcarbonate (DMC)) was fed into the reactor using a syringe pump in presence of N_2 stream (10mL/min). Analytical grade dihydroxybenzenes and DMC from Merck were used in the present study. Products were analyzed using gas chromatography (Agilent Model 19091J-413) with a HP-5.5% phenyl methyl siloxane capillary column equipped with a flame ionization detector and/or gas chromatography-mass spectroscopy (Shimadzu GC-17A equipped with a QP 5000 Mass spectrometer).

6.3 Results

6.3.1 Catechol methylation

6.3.1.1 Effect of catalyst systems

Figure 6.1 (a-d) shows catechol conversion and 2-MP selectivity on pure MgO and different alkali metals promoted MgO with DMC at 583 K. The amount of alkali metal hydroxides or nitrates loaded were 5 mMol per gram of MgO. 2-MP formed as a major product along with catecholcarbonate (PCC), 1,2-dimethoxybenzene (1,2-DMB) and C-methylated products (3-methylcatechol, 3-methylguaiacol and 4-methylguaiacol).

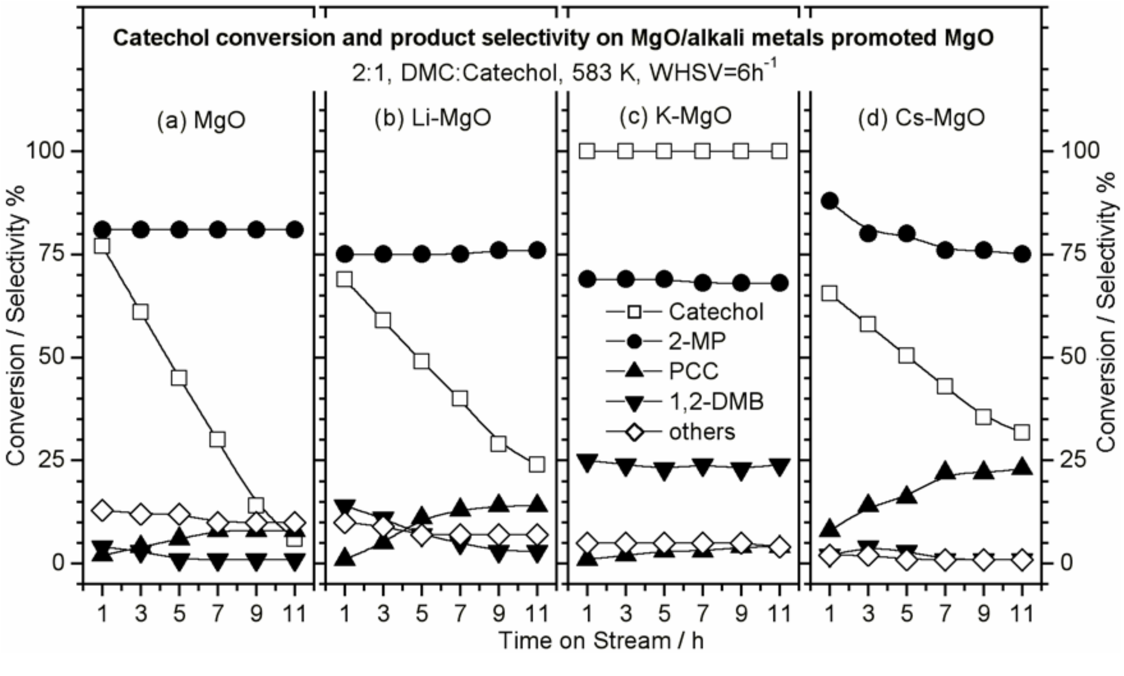

Figure 6.1: Selective O-methylation of catechol to 2-MP on MgO and alkali metal ions promoted MgO at 583 K at a space velocity = 6 h^{-1} with 2:1, DMC:Catechol feed mixture. 5mMol of alkali nitrates or hydroxides was loaded on MgO for the results shown in b-d.

It has been observed that MgO promoted by alkali metal ions show an improved activity for catechol methylation, especially towards selective 2-MP formation. Among the catalysts employed, K$^+$ promoted MgO (K-MgO) shows a stable 100% catechol conversion.

On MgO (Figure 6.1a) 2-MP selectivity was 80% and C-methylated products formed predominantly over 1,2-DMB and PCC. However, on Li (K) promoted MgO, 2-MP selectivity decreases to 75% (70%) and C-methylated products selectivity drops to 5% on K-MgO (Figure 6.1b and 1c). 1,2-DMB (PCC) formation decreases (increases) with TOS on MgO as well as Li-MgO. On the other hand, sizeable amount of 1,2-DMB formed (24%) on K-MgO. Suppression of PCC formation at the cost of 1,2-DMB on K-MgO is to be noted compared to Li- or Cs-MgO catalysts. On Cs-MgO (Figure 6.1d) 2-MP and PCC formation were observed to be more; however, initial 2-MP selectivity (88%) drops to 75%, whereas PCC selectivity increases up to 23% with TOS.

6.3.1.2 Effect of DMC to Catechol ratio

The feed composition studies on K-MgO at 573 K with DMC:catechol = 2 and 4 are shown in Figure 6.2a and 6.2b, respectively. The amount of KNO_3 loaded was 5 mMol per gram of MgO. 100% catechol conversion was obtained in both cases; however, products selectivity dramatically changed with the amount of DMC.

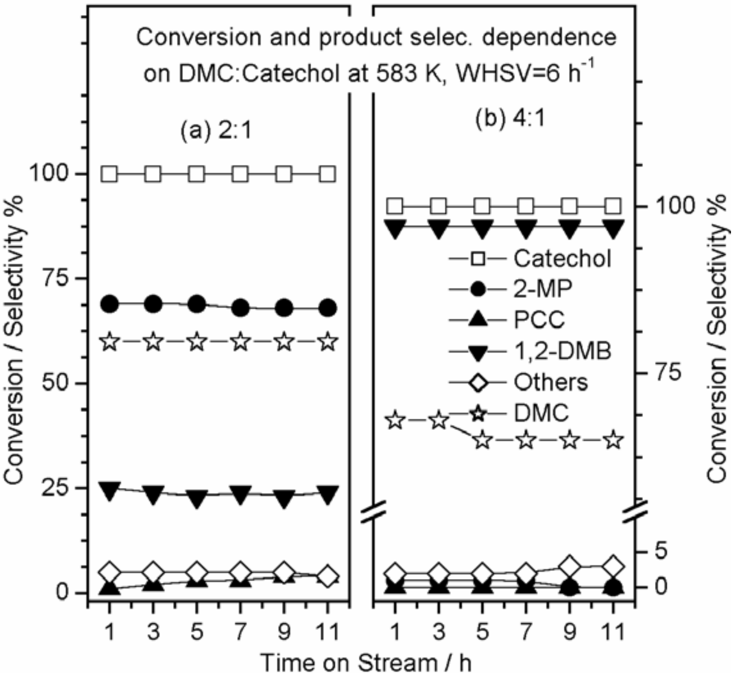

Figure 6.2: Feed composition dependence of catechol- and DMC- conversion and products selectivity on K-MgO at 583 K at a space velocity = 6 h^{-1}.

On increasing the feed ratio from 2 to 4, selective 1,2-DMB production was achieved. A dramatic change was observed in 1,2-DMB selectivity from 24% to 97% for a change in DMC:Catechol = 2 to 4, respectively. Only trace amount of 2-MP and C-methylated products and no PCC was formed at feed ratio = 4. DMC conversion was also shown in Figure 6.2 with respect to TOS, indicating that 60-65% DMC reacted for the complete conversion of catechol to methylated products and hence an effective utilization in the case of 2:1. However, some inevitable loss due to decomposition, vaporization of DMC cannot be prevented when excess DMC was added in the feed, as in the later case of 4:1.

6.3.1.3 Effect of reaction temperature

The effect of reaction temperature (523-583 K) on catechol conversion and product selectivity was given in Figure 6.3a-c. Reaction was carried out with feed mixture containing DMC:Catechol = 2 on 5 mMol K promoted MgO.

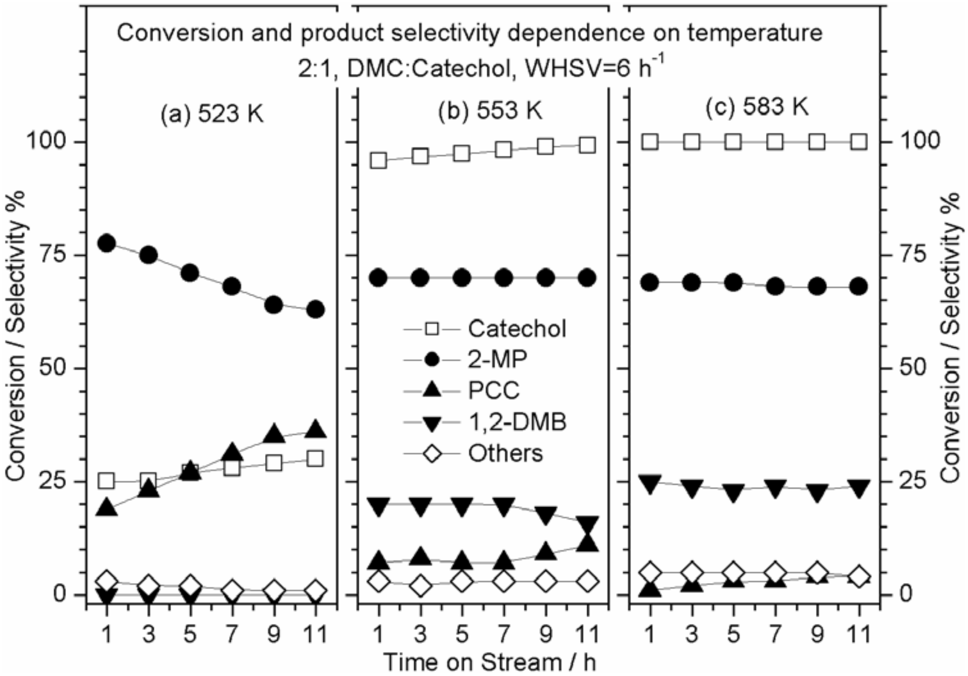

Figure 6.3: Reaction temperature dependence of catechol conversion and products selectivity on K-MgO at a space velocity = 6 h^{-1} with 2:1, DMC:Catechol feed mixture.

Catechol conversion increases from 25% at 523 K with increasing reaction temperature to nearly 100% at 553 K and then reaches 100% at 583 K. 2-MP selectivity was affected marginally at 523 K and it remains around 70% between 553 and 583 K. It is to be noted that PCC formation increases with TOS (18 to 36%) at 523 K. 1,2-DMB (PCC) selectivity increases (decreases) with increasing temperature from 523 to 583 K. This indicates 1,2-DMB forms at the expense of PCC at high reaction temperature and it is not likely through subsequent methylation of 2-MP. Since the 2-MP selectivity remains the same irrespective of the reaction temperature employed.

6.3.1.4 Effect of alkali metal Ions loading amount on MgO and activity

Figure 6.4a-c show catechol conversion and products selectivity dependence on amount of K loading per gram of MgO. 1-5 mMole KNO_3 was loaded per gram of MgO and the catalysts were screened for reaction at 583 K.

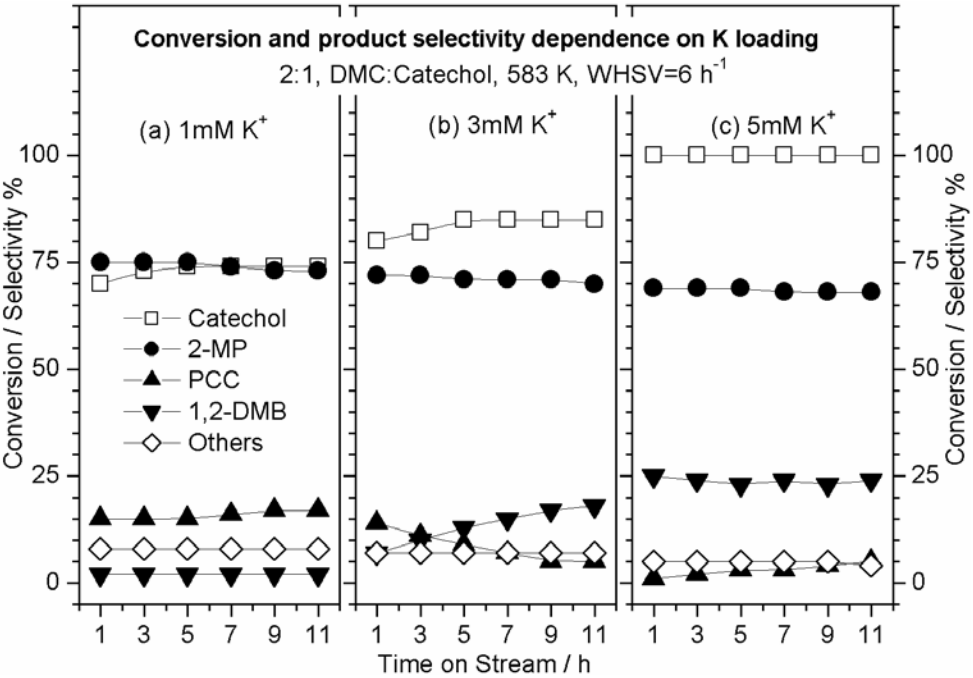

Figure 6.4: Catechol conversion and products selectivity dependence on the amount of KNO_3 loading (a= 1mM; b= 3 mM; c= 5 mM) on MgO at 583 K and at a space velocity = 6 h^{-1} with 2:1, DMC:Catechol feed mixture.

The results show that catechol conversion reached 100% at 5 mMol of K loading. 2-MP selectivity was almost unaffected and remains between 70 and 75% with 1-5 mMol of K loading amount. At lower loading (1 mMole) PCC forms appreciably, whereas 1,2-DMB forms at higher loading, which again indicates that 1,2-DMB forms exclusively at the expense of PCC. Large amount of K content (5mMol) and high temperature (583 K) favors 1,2-DMB formation rather than PCC, and 2-MP selectivity is marginally affected.

6.3.1.5 Effect of WHSV

WHSV (weight hourly space velocity) studies carried out on 5mMol K-MgO with DMC:Catechol = 2 feed at 583 K are shown in Figure 6.5. The result clearly indicating that catechol conversion is influenced to a large extent due to changes in WHSV.

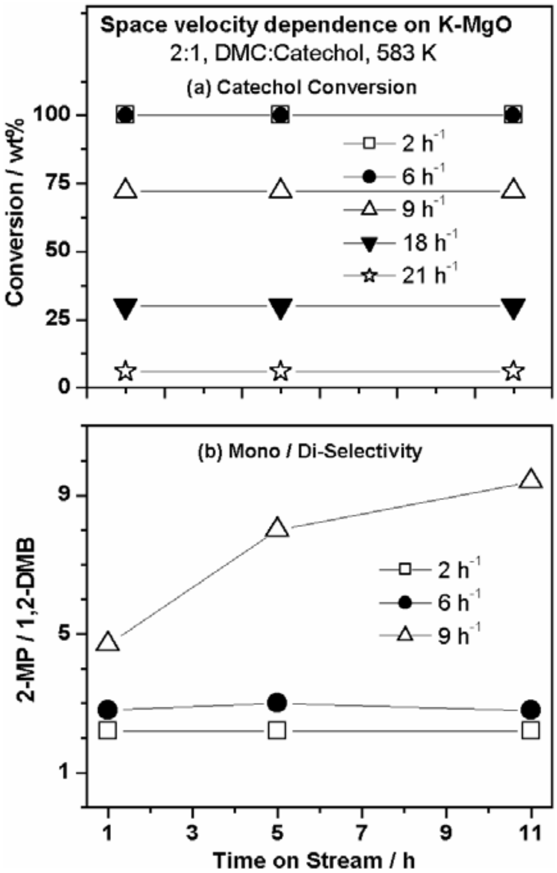

Figure 6.5: WHSV dependence of catechol conversion and the ratio between 2-MP to 1,2-DMB (mono to di methylation) at 583 K on K-MgO with 2:1, DMC:Catechol feed mixture. It is to be noted that at high WHSV, only 2-MP is produced and hence 2-MP to 1,2-DMB ratio is not given in panel b.

Although catechol conversion decreases to one third with increasing the space velocity from 6 to 18 h^{-1}, the initial conversion level for any WHSV values remains at the same level up to 12h indicating the stable catalytic activity (Figure 6.5a). O-methylated product selectivity is expressed in terms of 2-MP to 1,2-DMB (monomethoxy to dimethoxy) ratio in Figure 6.5b. It was found that the ratio is more than one indicating the selective monomethylation over dimethylation. The above methylation ratio increases exponentially at higher space velocity since 2-MP selectivity increases to 100% with no C-methylated products at space velocity above 9 h^{-1}. At space velocity=18 and 21 h^{-1} no 1,2-DMB and PCC were formed, where as, 1,2-DMB formed appreciably at space velocity < 9 h^{-1}.

6.3.2 Resorcinol methylation

6.3.2.1 Effect of catalyst systems

Figure 6.6 shows resorcinol methylation activity and product selectivity on pure and 5 mMole of alkali metals loaded MgO at 583 K with DMC:Resorcinol = 2. 3-methoxyphenol (3-MP) formed as a major product with 1,3-dimethoxybenzene (1,3-DMB) and other C-methylated products (4-methylresorcinol, 6-methyl-3-guaiacol and 4-methyl-3-guaiacol) as side products. Some high boiling biphenolic molecular fragments were also identified from GC-MS of reaction products.

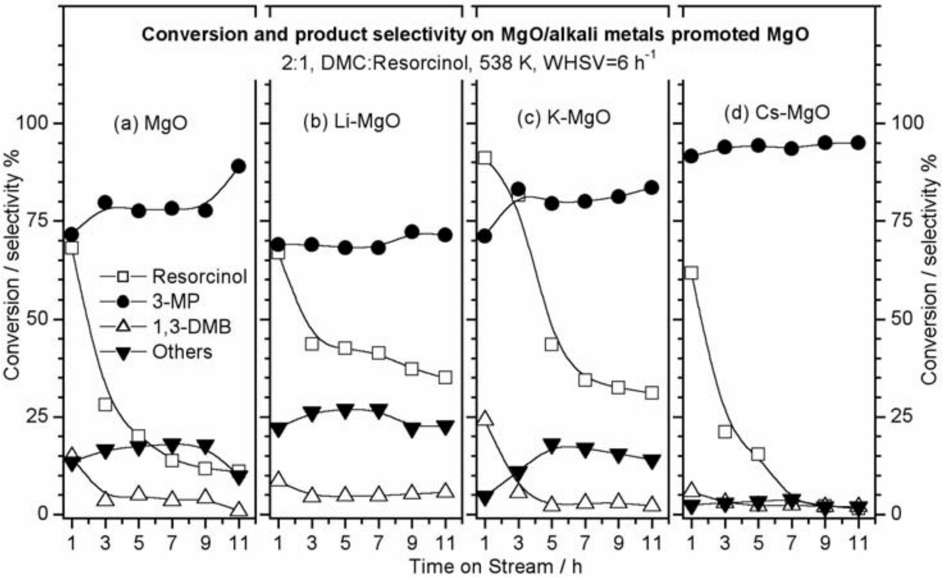

Figure 6.6: Selective O-methylation of resorcinol to 3-MP on MgO and alkali metal ions promoted MgO at 583 K and at a space velocity = 6 h^{-1} with 2:1, DMC:Resorcinol feed mixture. 5mMol of alkali nitrates or hydroxides loaded on MgO for the results shown in b-d.

It is evident that resorcinol conversion decreases significantly on all of the catalyst systems, unlike as in the case of stable catechol methylation on K-MgO (Figure 6.3c). Nonetheless, a considerably high initial resorcinol conversion was observed, indicating a possibility of high potential, on all of the catalysts. K-MgO shows 80-90% conversion up to TOS = 3h. Further the conversion decreases from the initial levels to about 40% on Li- and K-MgO catalysts. 3-MP selectivity remains at 80% on MgO and K-MgO, however it drops to 70% on Li-MgO. Cs-MgO shows faster deactivation than MgO though a highest 3-MP selectivity (>90%) was observed. Significant aromatic ring methylation was observed on all the systems, except Cs-MgO.

6.3.2.2 Effect of reaction temperature

The effect of reaction temperature on resorcinol conversion and products selectivity were studied at temperatures between 543 and 603 K (Figure 6.7). Conversion level increases systematically with increasing reaction temperature, however, deactivation was also observed with increasing TOS at all temperatures studied.

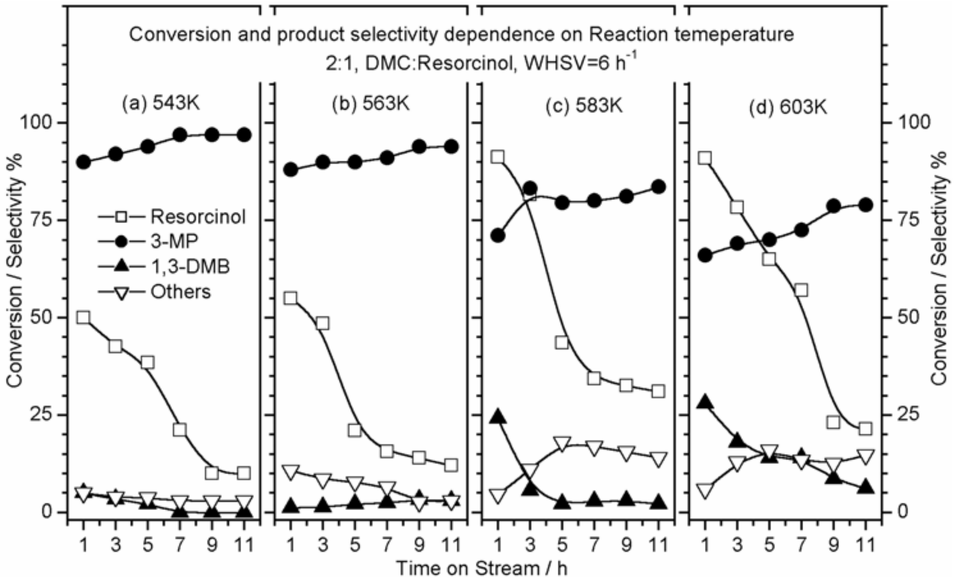

Figure 6.7: Reaction temperature dependence of resorcinol conversion and products selectivity on K-MgO at a space velocity = 6 h^{-1} with 2:1, DMC:Resorcinol feed mixture.

At low temperatures, 543 and 563 K, 3-MP formed selectively (90-97%) with traces of C-methylated resorcinol and 1,3-DMB. However, above 563 K secondary products formed appreciably and 3-MP selectivity drops to 80-70% between 583 and 603 K. Formation of 1,3-DMB in the initial few hours of reaction at ≥ 583 K at the expense of 3-MP indicating the step-wise methylation of 3-MP to 1,3-DMB.

6.3.2.3 Effect of DMC to Resorcinol ratio

Figure 6.8a-c show the effect of DMC to resorcinol molar ratio on resorcinol conversion and 3-MP selectivity.

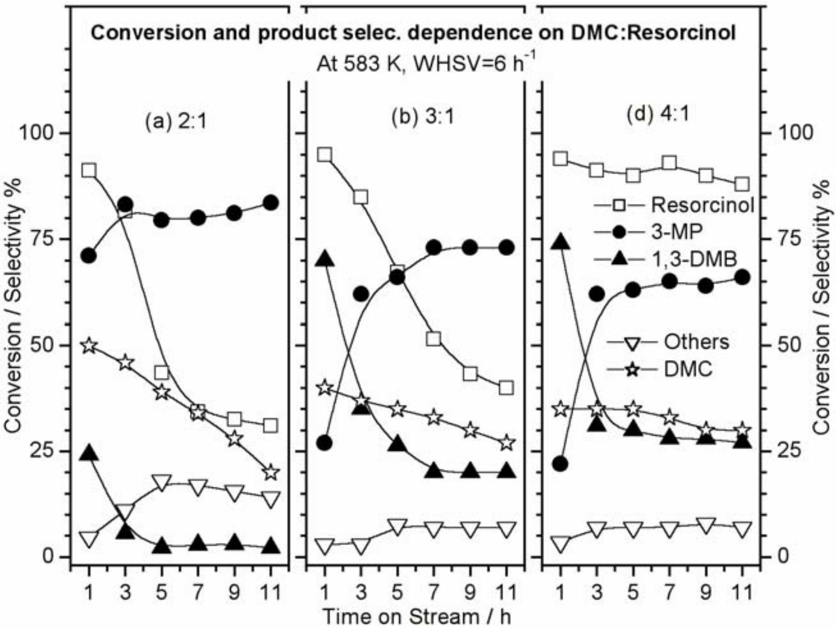

Figure 6.8: Feed composition (DMC:Resorcinol) dependence of resorcinol- and DMC- conversion and products selectivity on K-MgO at 583 K and at a space velocity = 6 h^{-1}.

It is interesting to note that the catalyst deactivation rate decreases on increasing DMC to resorcinol molar ratio from 2 to 4. A stable resorcinol conversion was observed, at least, up to 11h for DMC:Resorcinol = 4 (Figure 6.8c). 3-MP (1,3-DMB) selectivity increases (decreases) after the transient state (TOS = 1h), although 1,3-DMB was formed selectively (70-75%) during initial TOS (Figure 6.8b and 6.8c). The above results indicate the excess DMC prevents the catalyst deactivation. DMC conversion with respect to TOS was also given in Figure 6.8. The conversion of DMC decreases from 50% to 35% with increasing DMC amount.

6.3.2.4 Effect of WHSV

Figure 6.9 shows the effect of space velocity on resorcinol conversion and the desired product (3-MP) formation at various TOS.

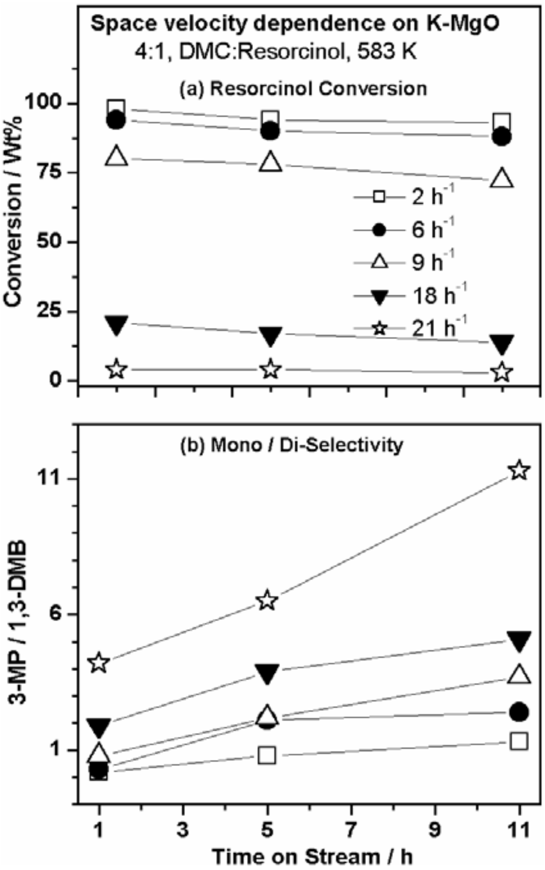

Figure 6.9: WHSV dependence of resorcinol conversion and ratio between 3-MP to 1,3-DMB (mono to di methylation) at 583 K on K-MgO with 4:1, DMC:Resorcinol feed mixture.

DMC:Resorcinol = 4 feed was used on 5 mMol of K promoted MgO at 583 K. A stable resorcinol conversion was observed at all the range of space velocity though conversion decreases with increasing space velocity (Figure 6.9a). Methylation capacity is plotted in terms of 3-MP to 1,3-DMB (monomethoxy to dimethoxy) ratio and the same is more than one at space velocity above 9 h^{-1}. This indicates the 3-MP selectivity improved to a large extent by reducing the substrates contact time with the catalyst. It is also to be noted that with time on stream the monomethoxy to dimethoxy products ratio increases substantially at all the space velocities.

6.3.3 Hydroquinone methylation

6.3.3.1 Effect of catalyst systems

Hydroquinone methylation on MgO and alkali metal loaded MgO with DMC:Hydroquinone = 2 feed ratio at 583 K was carried out and shown in Figure 6.10a-d. Methanol was added in the feed as solvent for all hydroquinone methylation studies since it is sparingly soluble in DMC. As such methanol has no methylation activity on these catalysts, it hardly affects the course of the reaction and the same was confirmed by carrying out independent experiments with methanol and hydroquinone and it shows no methylation at all.

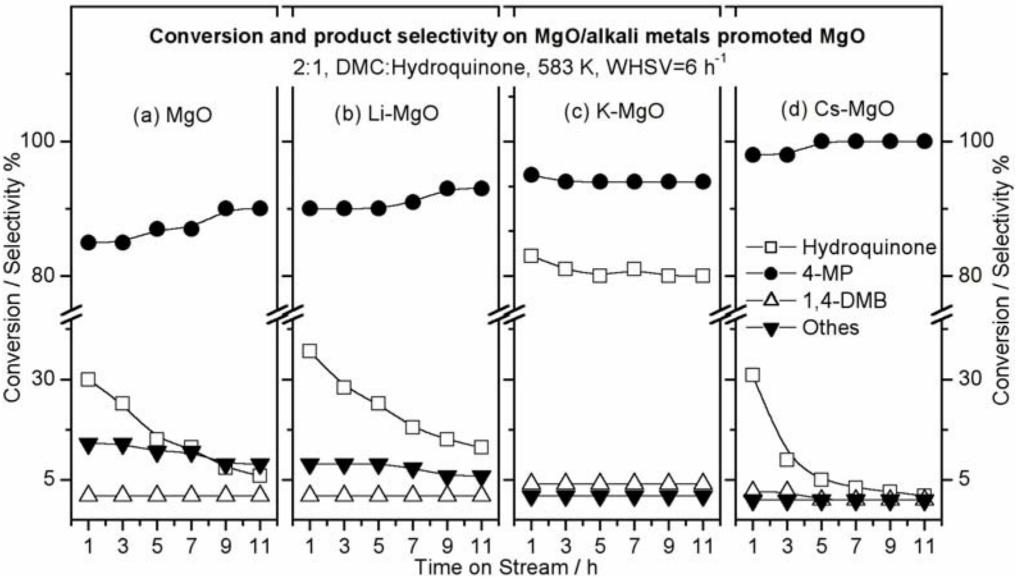

Figure 6.10: Selective O-methylation of hydroquinone to 4-MP on MgO and alkali metal ions promoted MgO at 583 K and at a space velocity = 6 h^{-1} with 2:1, DMC:Hydroquinone feed mixture. 5mMol of alkali nitrates or hydroxides loaded on MgO for the results shown in b-d.

4-methoxyphenol (4-MP) formed selectively along with small amounts of 1,4-dimethoxybenzene (1,4-DMB) and 2-methylhydroquinone. MgO shows considerable initial O-methylation activity with 90% 4-MP selectivity and significant amount of 2-methylhydroquinone (Figure 6.10a). It was observed that Li- and Cs-MgO also show some initial activity that declines with increasing TOS (Figure 6.10b and 6.10d). Nevertheless, K-MgO shows a stable hydroquinone conversion (80%) and selectively produces 4-MP (95% - Figure 6.10c). Generally, selectivity for 4-MP increases considerably on alkali ion promoted MgO. 1,4-DMB and 2-methylhydroquinone formed in traces only.

6.3.3.2 Effect of DMC to Hydroquinone ratio

The effect of feed composition was studied with DMC to hydroquinone molar ratio of 2 and 4 on 5 mMol K promoted MgO at 583 K.

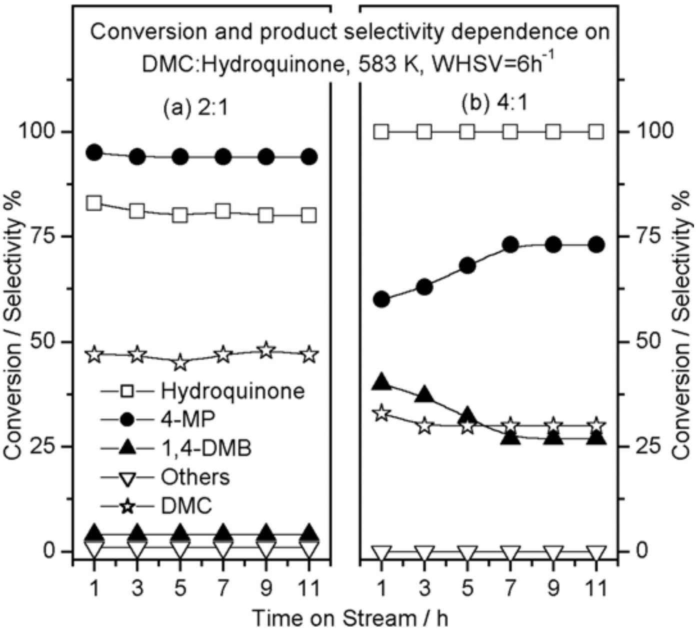

Figure 6.11: Feed composition (DMC:Hydroquinone) dependence of hydroquinone- and DMC-conversion and products selectivity on K-MgO at 583 K and at a space velocity = 6 h^{-1}.

Molar ratio of DMC:Hydroquinone = 2 displays 80% hydroquinone conversion with 95% selectivity for 4-MP (Figure 6.11a). At high molar ratio (4:1), 100% hydroquinone conversion was observed; however, selectivity for 4-MP drops significantly low to 70% with an increase in 1,4-DMB formation (30%). Higher DMC content in the feed leads to methylation of second phenolic –OH group or subsequent O-methylation of 4-MP to 1,4-DMB. 50 and 30% DMC conversion was observed with 2:1 and 4:1 molar ratio of DMC and hydroquinone, respectively indicating a significant loss of DMC in side reactions like gasification, dissociation etc.

6.3.3.3 Effect of WHSV

Space velocity influences the hydroquinone conversion and 4-MP selectivity as shown in Figure 6.12. Reaction was tested with DMC:hydroquinone = 2 feed mixture on 5 mMole of K loaded MgO.

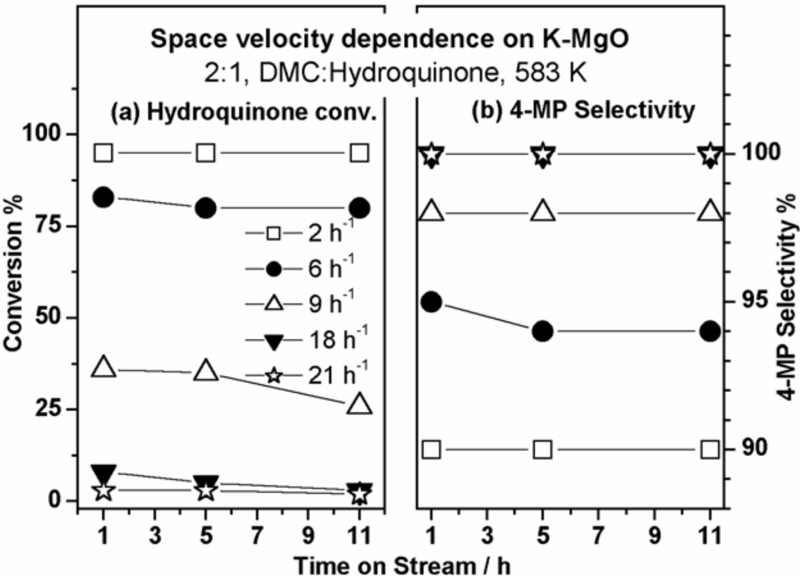

Figure 6.12: WHSV dependence of hydroquinone conversion and 4-MP selectivity at 583 K on K(5)MgO with 2:1, DMC:Hydroquinone feed mixture.

Hydroquinone conversion decreases rapidly from 95 % to 3 % on increasing the space velocity from 2 to 21 h^{-1}. 4-MP was produced with 90-100% selectivity for all the space velocities employed. It is to be noted that even at low space velocity ($2h^{-1}$), 4-MP selectivity did not decrease significantly as sizeable amount of 1,4-DMB was also not produced. This is in contrast to the results observed from catechol and resorcinol, where 1,2-DMB and 1,3-DMB was substantially produced at low space velocity ($2h^{-1}$). This clearly indicates that the second phenolic –OH groups is not at all vulnerable to methylation.

6.4. Discussion

6.4.1 Catechol and hydroquinone methylation

2-MP production from catechol on MgO and alkali ions loaded MgO was carried out effectively with DMC as a methylating agent. No methylation activity was found when methanol was used as methylating agent under identical reaction conditions ($\leq$ 603 K). Only K loaded MgO shows stable activity although 2-MP selectivity was marginally higher on other three catalysts (MgO, Li- and Cs-MgO) systems. Secondary products like PCC, 1,2-DMB and C-methylated catechol formation compete with each other depending on the reaction conditions. More C-methylated products were formed on MgO and Li-MgO. PCC formation increases with TOS on all the systems except K-MgO in which sizeable amount of 1,2-DMB formed. In general, 2-MP selectivity was affected by C-methylation and PCC formation. Catechol conversion increases and reached 100% on increasing the reaction temperature. 2-MP selectivity (70%) hardly changes with temperature between 523 and 583 K. At low temperature (523 K) formation of PCC increases, whereas 1,2-DMB formation increases at high temperature (583 K). This indicates the 1,2-DMB formation is likely through PCC methylation at high temperature.

An increase in K content also generally increases the extent of O-methylation capacity and hence an increase in 1,2-DMB linearly with K content. Space velocity study also confirms the formation of 1,2-DMB mainly through PCC methylation in a passive manner such that neither PCC nor 1,2-DMB formation occurs at space velocity >9 h^{-1}. Hence sequential methylation step of 2-MP to 1,2-DMB may either be ruled out or occur at minimum level. Since the mono- to di- O-methylation ratio is more than one and a stable 2-MP selectivity remains between 70-75% at space velocity < 9 h^{-1} indicating no sequential methylation of 2-MP to 1,2-DMB. A linear increase in O-methylation capacity with K concentration and very low side products at high space velocity ($\geq$ 9 h^{-1}) clearly indicates that by optimizing the process conditions and selective removal of 2-MP could lead to the selective production of 2-MP.

In the case of hydroquinone, K-MgO shows stable methylation activity and methylation activity decreases exponentially on other catalyst systems. 4-MP is formed selectively over 1,4-DMB and 2-methylhydroquinone. This indicates a perpendicular orientation of aromatic ring to the catalyst surface with one –OH group away from the adsorption site. On increasing DMC to hydroquinone molar ratio from 2 to 4, hydroquinone conversion reached 100%, with significant formation of 1,4-DMB at the cost of 4-MP selectivity. This demonstrates a sequential methylation of 4-MP to 1,4-DMB. Space velocity study also confirms that 4-MP formed exclusively at higher space velocity ($\geq 18\ h^{-1}$). Nonetheless, except with large DMC content in the feed, 4-MP forms selectively even under unfavorable conditions such as high contact time clearly indicating that the second phenolic –OH group is not easily accessible for methylation.

6.4.2 Resorcinol Methylation

Resorcinol methylation using DMC on MgO and alkali metal ions loaded MgO produces selectively 3-MP along with 1,3-DMB and C-methylated products. 3-MP selectivity was affected by sequential methylation to 1,3-DMB and C-methylated product formation. It is to be noted that 1,3-DMB fairly formed during initial TOS. C-methylated products formation was significant on all of the catalysts system except Cs-MgO, which is exclusively selective towards 3-MP. Methylation activity declines rapidly on all the of catalysts system, unlike catechol methylation, which is likely due to resorcinol condensation that produces polyaromatic chains that blocks the active sites, as shown in NMR and thermal analysis (Chapter 7).

Resorcinol conversion increases to larger extent with increasing amount of DMC in the feed. Resorcinol conversion reached 90% with 4:1, DMC:Resorcinol feed mixture, and stable activity was observed at least up to 11h. 3-MP selectivity increases after the transient state, while 1,3-DMB formed selectively during initial TOS. Apparently, an excess amount of

DMC, most likely prevents the intermolecular interaction of resorcinol on the catalyst surface. Hence resorcinol condensation and consequently the extent of polyaromatic chain formation were hindered. Thus a stable resorcinol conversion was observed with 4:1 feed mixture.

Resorcinol conversion increases with increasing reaction temperature (Figure 6.7); however, deactivation was observed with increasing TOS at all temperatures studied. At lower temperatures 543 and 563 K, 3-MP formed selectively (90-97%) with traces of C-methylated resorcinol and 1,3-DMB. Above 563 K secondary products are formed significantly and hence 3-MP selectivity drops subsequently. It is likely in the transient state at > 563 K subsequent methylation of 3-MP occurs to produce 1,3-DMB. However, 3-MP selectivity was stabilized at higher level at high TOS (3h). An opposite trend in selectivity between 1,3-DMB and other ring-methylated products indicates a possible isomerisation of 1,3-DMB at higher TOS.

A stable resorcinol conversion was observed (for DMC:Resorcinol = 4) at all the contact times, although conversion decreases with increasing space velocity. 3-MP selectivity increases to a larger extent at higher space velocity, as evident from the mono- to di- O-methylation ratio became more than one at higher space velocity ($\geq 18\ h^{-1}$).

6.4.3 Reactivity of dihydroxybenzenes

The results in Figures 6.1-6.12 suggest that although the three DHB compounds are just isomers, a large reactivity difference exist among them. The variation in reactivity trends is attributed to difference in their acidity. The acidities of these three compounds are in the following increasing order catechol<hydroquinone<resorcinol. Since MgO and alkali metal ions promoted MgO are basic catalysts, most acidic resorcinol chemisorbs strongly and deactivates the active basic sites, which does not happen with other two isomers or occurs at

a lower level. This is supported from the highest carbon content observed in thermal analysis on spent catalyst after resorcinol methylation.

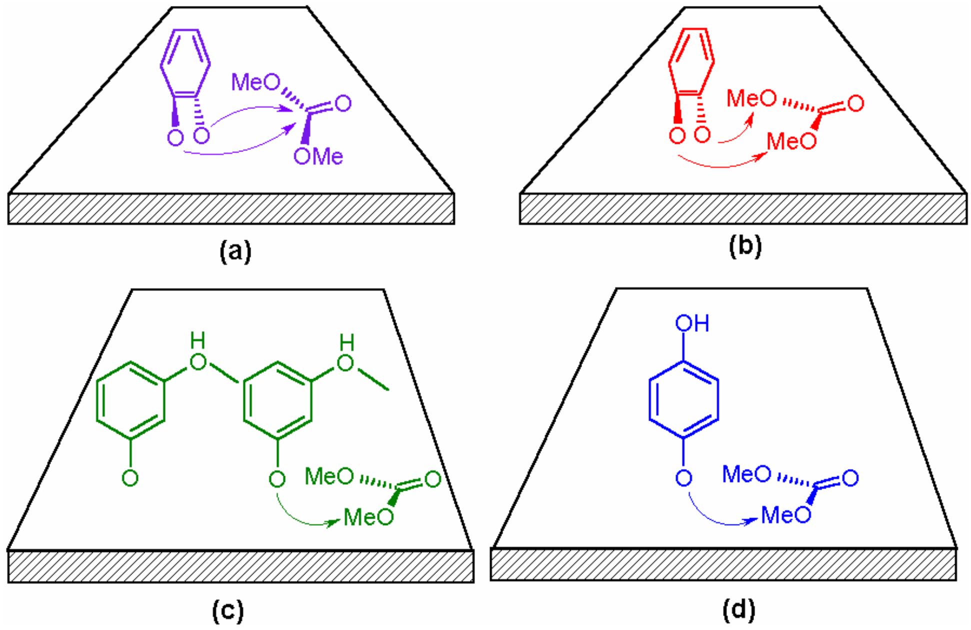

Figure 6.13: Pictorial representation of (a) PCC and (b) 1,2-DMB formation from catechol; (c) intermolecular interaction between resorcinol and (d) hydroquinone methylation.

The probability of the hydroxyl groups interaction towards catalysts surface drives the product selectivity. For instance, catechol has a very good chance of both the hydroxyl groups interacting on the catalysts surface as shows in the pictorial representation (Figure 6.13a-b) compared to resorcinol and hydroquinone. Thus the formation of PCC and 1,2-DMB are expected and indeed the same was fairly observed. PCC formation was through the addition of DMC to 1,2-hydroxyl groups of catechol (Figure 6.13a). In general, 1,2-DMB formation is likely through anyone of the following three possible ways. Direct O, O dimethylation of catechol, PCC ring opening followed by dimethylation and methylation of 2-MP. Temperature dependent studies on products selectivity shows that 1,2-DMB forms only at the expense of PCC. Hence 1,2-DMB formation through sequential methylation of 2-MP can be ruled out. An exception is a direct O,O-dimethylation of catechol to 1,2-DMB, especially when excess amount of DMC was available in the feed (Figure 6.13b).

In case of resorcinol and hydroquinone, only one of the hydroxyl groups interacts with the catalysts surface. Hence the interacting hydroxyl group was getting methylated and the selectivity for methoxyphenols (MPs) was quite high. However, the free hydroxyl group is likely to facilitate an intermolecular interaction between resorcinol molecules that lead to polyaromatic chain formation (Figure 6.13c). The spatial arrangement of hydroxyl groups in resorcinol and its acidity eases the condensation process. Thus polyaromatic chain formation was facile with resorcinol and it blocks the active basic sites that lead to catalysts deactivation with TOS. When feed with 4:1, DMC:Resorcinol was employed, apparently excess DMC prevents the intermolecular interaction of resorcinol molecules. Hence resorcinol condensation and poly aromatic chain formation was hindered. Thus a stable resorcinol conversion was observed with 4:1 feed composition. In hydroquinone (Figure 6.13d) the free hydroxyl group spatial arrangement is in such a way that it might condense with another gas phase molecule; however, a stable activity suggests that the above condensation is unlikely. Hence, no extensive polyaromatic chain formation with hydroquinone was observed, as it is evident from a thermal analysis and catalytic activity.

6.5. Conclusions

A comprehensive study on O-methylation of dihydroxybenzenes with DMC was carried out on MgO and alkali metal ions (Li, K and Cs) promoted MgO under vapor phase conditions. Pure MgO have O-methylation activity that declines rapidly with time on stream (TOS). Alkali metal ions promoted MgO show better activity than pure MgO with all of the DHB substrates. Among the catalyst systems screened, K-MgO shows the best mono-O-methylation activity with relatively high stability for all of the substrates. Reactivity and product selectivity were influenced by DHB acidity and their mode of interaction on the catalysts surface. Catechol interacts through 1,2 hydroxyl groups on the catalysts surface gave more secondary products like PCC and veratrole; however, possible indications are available to further maximize 2-MP selectivity by varying reaction conditions. Resorcinol and hydroquinone interactions leave another hydroxyl group free and this free hydroxyl group helps polyaromatic chain formation and blocks the active sites that lead to catalysts deactivation with TOS. Low temperature (< 610K) employed leads to high selectivity for methoxyphenols compared to high dimethoxybenzenes selectivity observed in the literature reports.

6.5 References

1. Y. Fu, T. Baba, Y. Ono, Appl. Catal. A: Gen. 166 (1998) 419.
2. Y. Fu, T. Baba, Y. Ono, Appl. Catal. A: Gen. 166 (1998) 425.
3. Y. Fu, T. Baba, Y. Ono, Appl. Catal. A: Gen. 176 (1998) 201.
4. Y. Fu, T. Baba, Y. Ono, Appl. Catal. A: Gen. 178 (1999) 219.
5. L. Calzolari, F. Cavani, T. Monti, Solid State Chem. Catal. 3 (2000) 533.
6. F. Cavani, T. Monti, Catalysis of Organic reactions 82 (2001) 123.
7. F. Cavani, T. Monti, D. Paoli, Stud. Surf. Sci. Catal. 130 (2000) 2633.
8. V. Vishwanathan, S. Ndou, L. Sikhwivhilu, N. Plint, K. Vijayaraghavan, N. J. Coville, Chem. Commun. (2001) 893.
9. M. B. Talawar, T. M. Jyothi, P. D. Sawant, T. Raja, B. S. Rao, Green Chem. 2 (2000) 266.
10. T. M. Jyothi, T. Raja, M. B. Talawar, B. S. Rao, Appl. Catal. A: Gen. 211 (2001) 41.
11. L. Kiwi-Minsker, S. Porchet, R. Doepper, A. Renken, Stud. Surf. Sci. Catal. 108 (1999) 149.
12. L. Kiwi-Minsker, G. Jenzer, L. Pliasova, A. Renken, Stud. Surf. Sci. Catal. 121 (1999) 159.
13. R. Bal, B. B. Tope, S. Sivasanker, J. Mol. Catal. A: Chem. 181 (2002) 161.
14. R. Bal, S. Mayadevi, S. Sivasanker, Organic Process Res. Development 7 (2003) 17.
15. X. Zhu, X. Li, M. Jia, G. Liu, W. Zhang, D. Jiang, Appl. Catal. A: Gen. 282 (2005) 155.
16. Z. Fu, Y. Y. D. Yin, Y. Xu, H. Liu, H. Liao, Q. Xu, F. Tan, J. Wang, J. Mol. Catal. A: Chem. 232 (2005) 69.

Chapter 7: Mechanism of MgO and promoted MgO catalysts deactivation

7.1 Introduction

One of the most critical problems experienced in many catalytic reactions is the catalyst deactivation with time on stream and any industrial process wants to avoid this as long as possible. This deactivation process affects not only the catalyst activity but also the product selectivity. After long lasting experiments, the catalyst activity decreases due to various reasons, such as build up of carbonaceous deposits or coke formation, change in oxidation state of the metal ions, sintering of the catalyst particles and catalyst undergoing chemical reactions or catalyst poisoning [1]. Significant importance is often given for spent catalyst characterization and a great number of techniques have been in practice to identify the reason for catalyst deactivation. Severe activity drop was observed with dihydroxybenzene (particularly resorcinol) O-methylation on MgO and alkali metal ions loaded MgO (Chapter 6). Spent catalysts were subjected to XRD, surface area measurements, ^{13}C MAS NMR, XPS and thermal analysis in order to identify the nature of carbonaceous deposits and the results are given in the present chapter and discussed in detail.

7.2 Results

7.2.1 XRD and surface area measurements

XRD (Figure 7.1) and surface area (Table 7.1) results from fresh and spent catalysts after reaction for 4h on time on stream are given. No new reflections were observed for spent catalysts, whereas alkali metal oxides reflections (Li_2O, K_2O and Cs_2O) disappeared after the reaction. Further, the broad features observed for spent catalysts (Figure 7.1b) compared to the sharp and intense for fresh samples (Figure 7.1a) indicate the sample crystallinity decreases and which is severe in the case of Cs-MgO. Table 7.1 shows a decline in the crystallite size for the spent catalyst (significant for MgO and Cs-MgO) compared to the fresh ones. Further, the maximum drop in crystallite size was observed for resorcinol methylation sample (MgO-Res).

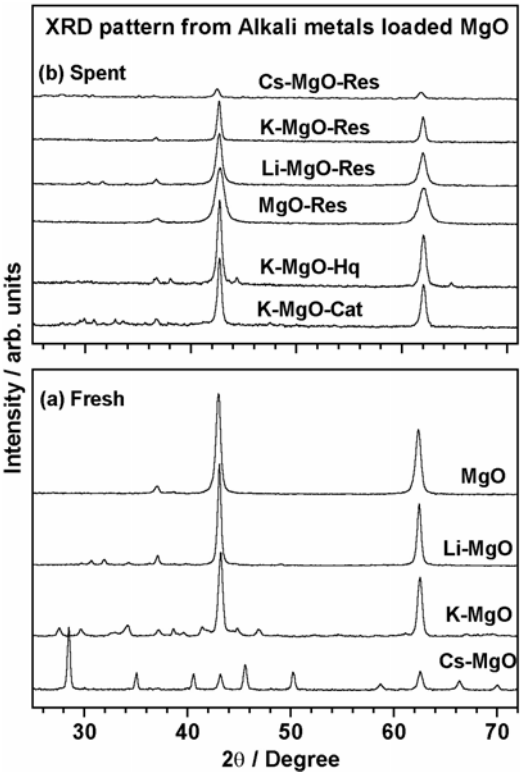

Figure 7.1: XRD pattern from MgO and alkali metal ions loaded MgO (a) fresh catalysts (calcined at 673 K for 2h) and (b) spent catalysts (after DHB methylation test for 4h TOS).

Almost same crystallite size was observed on K-MgO before and after O-methylation of catechol and hydroquinone and the size change after resorcinol methylation is not dramatic as in other cases. However, in all other cases, such as MgO, Li-MgO and Cs-MgO spent catalysts demonstrate a break up of crystallites up to a severe extent of doubling the number of crystallites as in MgO. It might be a reason that MgO show low activity with all of the DHB substrates, in contrast to K-MgO showing high activity and almost same crystallite size.

Surface area also decreases for spent catalysts indicating the presence of coke and/or reactants and products in adsorbed form on the catalysts surface. The extent of decrease in surface area of spent catalysts decreases with alkali metal ions loading. The percentage surface area drop are 65, 52, 63 and 15-36 for MgO, Li-MgO, Cs-MgO and K-

MgO, respectively. Thus the percentage fall is relatively low on spent K-MgO catalysts, which shows comparatively low carbonaceous deposition on this system for resorcinol methylation. On the other hand, catechol and hydroquinone methylation catalysts that hardly deactivates are showing 15 and 25% surface area drop, respectively.

Table 7.1: Physical and Textural properties of fresh and spent MgO and alkali metal ions loaded MgO catalysts.

Catalysts	Crystallite Size / nm Spent (Fresh)	S_{BET} / m^2/g Spent (Fresh)
MgO-Res	6.5 (11.8)	21 (60)
Li-MgO-Res	8.4 (12.6)	24 (49)
K-MgO-Res	10.6 (11.8)	18 (28)
Cs-MgO-Res	10.1 (19.3)	6 (16)
K-MgO-Cat	11 (11.8)	24 (28)
K-MgO-Hq	11.5 (11.8)	21 (28)

7.2.2 Thermal analysis

Figure 7.2 (a-c) shows TG-DTA profiles from K-MgO spent catalysts in air atmosphere after catechol, resorcinol and hydroquinone methylation for 1h at 583 K. It has been observed that the spent catalyst were completely black indicating a large extent of coke deposition. The initial high activity observed at TOS=1h, became one third during TOS ≥4h and indicating the activity loss is mainly due to carbon deposition that increases with TOS. Analysis of these long lasted spent catalysts provides no substantial new information other than high carbon content and hence spent catalysts after TOS=1h, which remains active, was chosen for thermal analysis. The initial small weight loss (<10%) at about 400 K observed on all of the spent catalysts is attributed to the loss of water. Large amount of carbon deposition is evident from the weight loss observed between 420 and 750 K in the TGA profiles (Figure

7.2 a-c). The total percentage weight loss observed at 1000 K is around 40, 60 and 50, with catechol, resorcinol and hydroquinone spent catalysts, respectively.

Derivative of the TG (DTG) weight loss (Figure 7.2 a-c) shows the peak maximum at which the weight losses were observed in TGA. In the case of catechol and resorcinol, the DTG shows two-stage weight loss occur at 575-645 K and 670-740 K, respectively, whereas one major weight loss at 640 K and a minor weight loss at 710 K were observed with hydroquinone. The carbon deposition on the catalyst is dependent on the type of reaction. NMR analysis of the spent catalyst revealed the presence of alkyl groups/chains, aromatic and polyaromatic carbons (Section 7.2.3). The weight loss observed may be due to adsorbed alkyl groups/chains and polyaromatic carbon compounds. The weight loss observed at 740 and 710 K in Figure 7.2b and c respectively, may be due to the presence of high boiling biphenolic compound. The presence of these compounds was indicated in the analysis of resorcinol methylation products by GC-MS. Figure 7.2d shows the DTA curves in which a positive microvolt (μV) heat flow at respective temperatures was observed due to carbon burning in air atmosphere. This shows the TG weight losses observed are exothermic in nature, as expected, that increases the system temperature with respect to the reference material.

Further, it is interesting to notice a weight loss occurring at 650-670 K in all the above three cases, hinting the similar nature of carbon deposit, which is likely to be polyaromatics. Adsorbed molecular components such as, reactants and products, and coke or graphite will get oxidized in air and hence it is difficult to account for the weight losses by carrying out thermal analysis only in air atmosphere. However, thermal analysis in N_2 atmosphere might reveal, to a limited extent, the nature of the desorbing components. Figure 7.2 (e, f and g (thick traces for weight loss and dash/dot traces for DTG) shows the TG results carried out in N_2 atmosphere for K-MgO spent catalysts with all three DHB reactants.

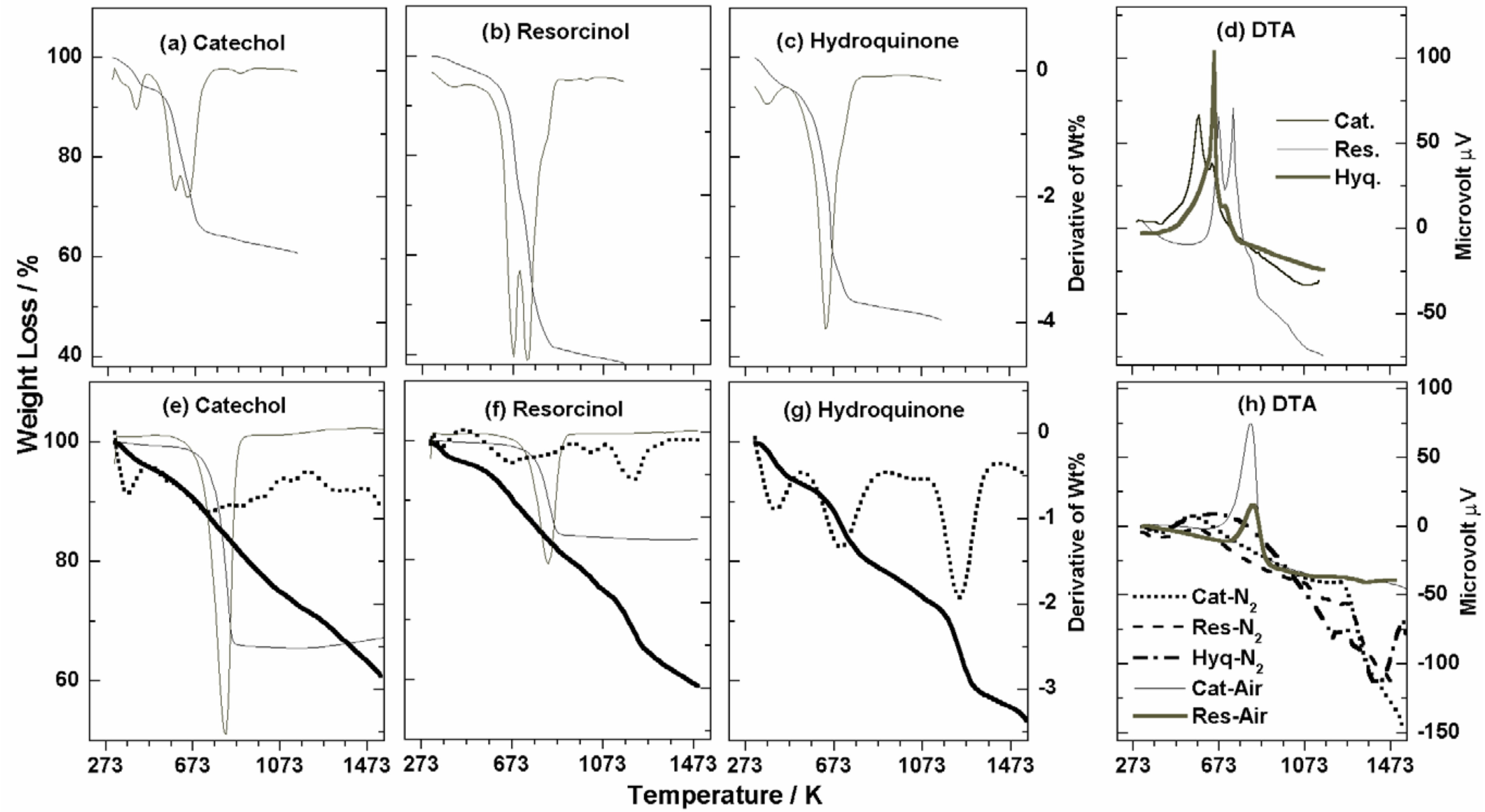

Figure 7.2: Thermal analysis on K-MgO spent catalyst for all three DHB methylation at 583 K and at a space velocity = 6 h^{-1} for 1 h TOS with 2:1, DMC:DHB feed mixture. TGA and derivative of TGA weight loss under air (a-c) and N_2 (e-g) atmosphere with corresponding DTA in (d) and (h), respectively. Subsequent TGA and derivative of TGA weight loss under air atmosphere, after N_2 atmosphere analysis of catechol (e) and resorcinol (f) and corresponding DTA in (h).

It is to be noted that weight loss at 1473 K for catechol, resorcinol and hydroquinone are approximately 40%, in contrast to higher weight loss due to complete burning at 1000 K in air atmosphere for resorcinol and hydroquinone. Two broad weight loss features were noted from all of the three spent catalysts from the DTG profiles at 500-800 K and 1100-1300 K. DTA curves (Figure 7.2h) show a negative microvolt heat flow and hence endothermic weight loss processes, unlike in air atmosphere. In the case of catechol these two weight losses are not very distinct, whereas resorcinol and hydroquinone shows very sharp and distinct features. The spent catalysts that are subjected to thermal analysis in N_2 atmosphere are subsequently subjected to thermal analysis in air atmosphere without removing from the thermal analyzer and the results (TG and DTG) for catechol and resorcinol spent catalysts are shown in Figure 7.2 e and f (thin traces), respectively. Exothermic DTA profiles for the same that show single sharp peak are given in Figure 7.2h. All the samples show a weight loss peak around 830 K, again indicating a similar nature of carbon, which is likely to be polyaromatics, since it cannot be oxidized/desorbed in nitrogen. However, a partial decomposition was a likely phenomenon that could have occurred while heating in nitrogen atmosphere up to 1473 K and hence a shift in the oxidation of decomposed polyaromatics in the subsequent heating in air [2,3].

7.2.3 ^{13}C CP-MAS NMR

Figure 7.3 shows ^{13}C CPMAS NMR results from spent K-MgO catalysts after catechol and resorcinol methylation reaction at 583 K for 1h. Peaks related to adsorbed reactants and/or products (112 ppm), carbons without protons but attached to heteroatom (152 ppm), alkyl groups/chains (20 ppm), $MgCO_3$ (170 ppm) and polyaromatics (125 ppm), were identified from the broad features. However, it is clear that the spectral feature is strongly dominated by aromatic carbon species above 105 ppm [4]. Strong peak at 125 ppm is attributed to polyaromatic carbon species due to polymerization of reactant/product molecule in different environment. This is the main carbon species that blocks the active sites. In the case of catechol, this strong peak looks very sharp and symmetrical; however, the main peak in resorcinol is very broad with shoulders at 142 and 150 ppm (indicated by arrow) is ascribed to other carbon species mentioned above.

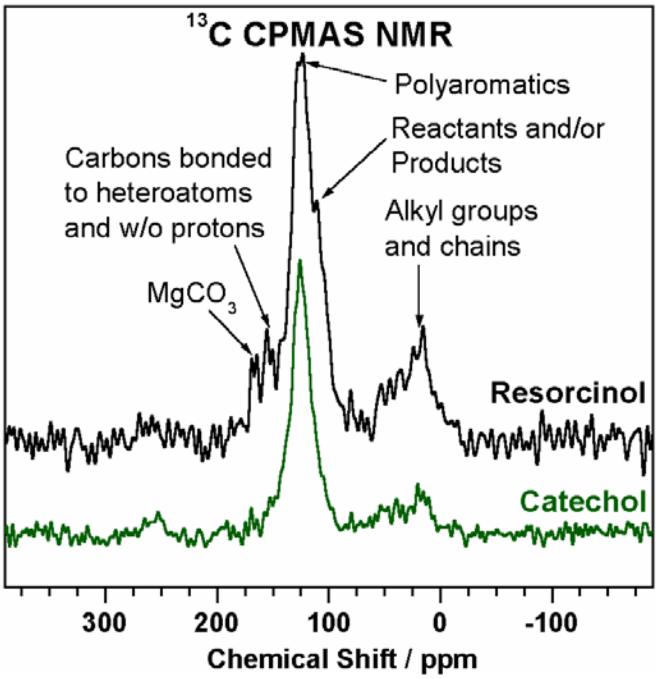

Figure 7.2: ^{13}C CPMAS NMR spectra from K(5)MgO spent catalyst for DHB methylation at 583 K and at a space velocity = 6 h^{-1} for TOS = 1h with 2:1, DMC:DHB feed mixture.

Alkyl carbon species was also observed at 20 ppm (indicated by arrow) on both the catalysts indicating the presence of methylated products or alkyl chains/groups on the catalysts. This alkyl feature is relatively broad and strong for resorcinol catalysts. It is to be pointed out here that the above low intensity alkyl feature supports the effective DMC utilization in catechol case than the resorcinol case. Carbonate carbon species, likely from $MgCO_3$ [5] was also observed at 168 ppm clearly in the case of resorcinol catalyst that is weak on catechol reaction catalyst. Indeed, more $MgCO_3$ is evident on resorcinol case from the relatively high weight loss around 1000 K than in the catechol case, which shows a marginal weight loss.

7.2.4 XPS Analysis

7.2.4.1 O 1s, Mg 2p, C 1s and K 2p core level analysis

Figure 7.4a shows O 1s spectra from spent and fresh K-MgO catalysts. The O 1s spectrum is very broad for fresh sample with a main peak centered at a binding energy (BE) 530.2 eV and a shoulder at 532.3 eV attributed to the hydroxyl groups from adsorbed moisture on the catalysts [6-8]. Spent K-MgO catalysts taken after methylation test for 1h TOS show a relatively sharp peak at 531 eV. A shift in BE around 1.8 eV was observed only on resorcinol (DMC:Res = 2:1 feed) for which the peak appeared at 532 eV. This clearly indicates an onset in change in surface characteristics towards deactivation on resorcinol exposed K-MgO (Chapter 6).

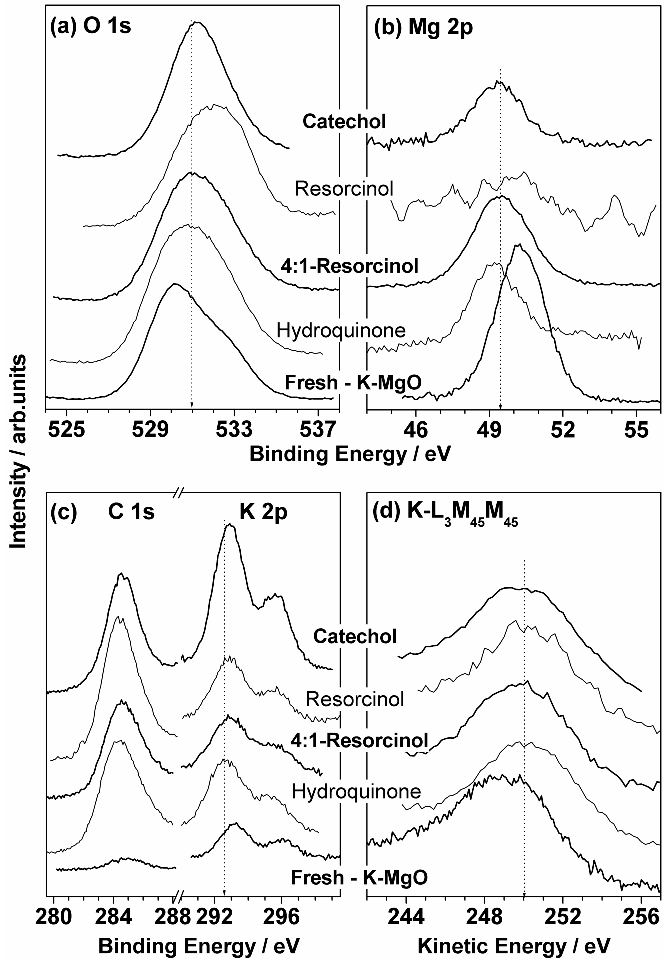

Figure 7.4: Photoemission spectra from K-MgO spent catalysts after O-methylation of DHB at 583 K and at a space velocity = 6 h^{-1} for 1h TOS with 2:1, DMC:DHB feed mixture. Fresh K-MgO XPS results are also given for comparison.

Figure 7.4b shows Mg 2p core level spectra from fresh and spent K-MgO catalysts. A sharp peak at 50.3 eV was observed for the fresh sample is evident for typical Mg^{2+}. Generally Mg 2p intensity was low on all the spent catalysts. Spent K-MgO samples exhibit Mg 2p peak at BE 49.4 eV. However, resorcinol methylation sample (DMC:Res = 2:1) hardly shows any Mg 2p intensity and it is attributed to the poor surface Mg^{2+} concentration.

Figure 7.4 (c and d) shows C 1s and K 2p and K-$L_3M_{45}M_{45}$ Auger transition from fresh and spent K-MgO catalysts. Fresh sample exhibits two peaks at 293.3 and 296 eV and they are attributed to K $2p_{3/2}$ and $2p_{1/2}$, respectively [9,10]. Spent catalysts also show similar features, however, at lower BE side at 292.8 and 295.5 eV. It is interesting to note a higher K 2p intensity on all the spent catalysts compared to fresh catalyst, hinting a dramatic surface modification and a change in the surface composition due to reaction. This difference between fresh and spent catalysts for K 2p level is also well reflected in Auger electron spectral results. K-$L_3M_{45}M_{45}$ level appeared at a kinetic energy of 249 eV for fresh catalysts, whereas for spent catalysts the peak centered at 250 eV. C 1s spectra from fresh and spent K-MgO (Figure 7.4d) show no significant difference. A sharp intense peak at 285 eV was observed for all of the spent catalysts indicating a large amount of carbon content on the catalysts surface, unlike fresh K-MgO. Any C 1s feature from fresh catalyst is mainly due to the presence of adventitious carbon whereas for spent catalysts they are attributed to adsorbed reactants and/or products including coke.

7.2.4.2 Surface composition

Table 7.2 shows the surface atomic ratio of fresh and spent K-MgO catalysts. It is evident from Mg/C ratio and also K/Mg ratio that surface Mg concentration decreases during reaction. Very low Mg/C was observed for K-MgO after reaction with 2:1, DMC:Resorcinol. However, reaction with 4:1, DMC:Resoricnol feed shows higher amount of surface Mg which is evident from very low K/Mg (0.017) and very high Mg/C (4.769) ratio. Surface K concentration is high for spent catalysts compared to the fresh ones, except for 4:1, DMC:Resorcinol reaction sample as evident from K/Mg ratio. Comparable K/C ratio for all the spent except catechol reaction sample, which is having very high K/C ratio shows the surface, is enriched with K.

Table 7.2: Surface Atomic Ratio of fresh and spent K-MgO catalysts.

Atomic Ratio	Fresh Catalyst	Spent Catalyst[a]			
		Catechol	2:1, DMC:Res.	4:1, DMC:Res.	Hydroquinone
K/ Mg	0.024	2.565	2.153	0.017	0.147
K/C	-	0.478	0.055	0.078	0.086
Mg/C	-	0.186	0.025	4.690	0.582
(K+Mg)/C	-	0.664	0.080	4.768	0.668

[a] K-MgO catalyst was subjected with all reactants at optimum conditions (space velocity = 6 h^{-1}; RT = 583 K; TOS = 1h). 2:1 ratio of DMC:DHB was employed for all cases and 4:1 ratio as employed additionally with resorcinol.

(K+Mg)/C ratio shows a very high carbon content on 2:1, DMC:Resorcinol spent catalyst, whereas 4:1, DMC:Resorcinol spent catalyst shows a very low carbon content indicating a drastic change in surface composition, depending on DMC amount used in the reaction. Catechol and hydroquinone methylation samples show comparable (K+Mg)/C ratio.

7.3 Discussion

7.3.1 XRD and surface area

A decrease in the crystallite size for spent MgO and alkali metal ions loaded MgO indicates the catalyst particle disintegration due to carbonaceous deposits due to reaction conditions. The decrease in sample crystallinity is also evident from the peak broadening for spent catalyst, especially for MgO and Cs-MgO. Similarly, resorcinol methylation condition was highly destructive and indicating a large amount of carbonaceous deposits, unlike on the other two isomers. Surface area measurement for spent catalysts supports the XRD observations. Deactivation encountered for all the catalysts except K-MgO and with resorcinol methylation condition (DMC:Res=4) are mainly due to carbon deposition.

7.3.2 Thermal analysis, ^{13}C NMR and XPS

45-60% weight loss observed with the spent catalysts in thermal analysis under air atmosphere indicates a heavy carbon deposition during DHB methylation. The nature of one of the deposited carbon species is found to be similar in all the three cases. Carbon species that burn in air at 640-670 K is attributed to the polyaromatic chains that bind very strongly to the active sites on all the three systems. However, thermal analysis in N_2 atmosphere revealed the presence of adsorbed reactants and/or products along with this polyaromatics is evident from the low temperature (below 1000 K) weight loss peak. The minor weight loss observed at 580 K in air atmosphere and the broad weight loss observed at 500-850 K in N_2 atmosphere in catechol case is likely due to molecular species (reactants and products). The minor weight loss and optimum reaction temperature, 583 K supports the nature of the above carbon species to be from adsorbed molecular components. Similar observations could be seen in hydroquinone case, except for the molecular species being observed at high temperature in air (725 K) and a broad weight loss in N_2 at 570-850 K. A large weight loss in N_2 atmosphere between 573-1000 K for resorcinol case hints the molecular desorption as in the above cases. Above observation and high temperature required for the second weight loss peak in resorcinol (in air) suggests the strong chemisorption of molecular components.

Further, a partial decomposition of polyaromatics to hydrogen deficient polyaromatics or graphitic carbon during thermal analysis in N_2 atmosphere is evident from the successive weight loss at 850 K in the subsequent TG in air atmosphere analysis of the same sample. It is evident that resorcinol is the most acidic substrate followed by hydroquinone and catechol and hence the polyaromatic chains found in the case of resorcinol is most likely to be of high molecular mass, whereas in the case of hydroquinone and catechol, comparatively low molecular weight polyaromatic chains are expected. The extent of weight loss (resorcinol (63%) >hydroquinone (50%) >catechol (40%)) observed on the three systems in air atmosphere (Figure 7.2 a-d) clearly supports the above conclusions as well as the activity trend observed. The condensation or polymerization of these acidic substrates is boosted by the basic active sites of the catalysts. Further, the spatial arrangement of the resorcinol molecule on the catalysts surface also possibly enhances the condensation process through intermolecular interaction.

Solid state ^{13}C CPMAS NMR of the spent catalysts exhibits chemical shifts characteristic of different carbon atoms. Aliphatic carbons are ascribed to the methyl groups and/or aliphatic chains from the adsorbed products on the catalysts surface. The chemical shifts value and the peak broadening observed in the aromatic region revealed the presence of polyaromatics, apart from reactants and products. This peak broadening is more for resorcinol than catechol indicating a heavier and larger amount of polyaromatics and adsorbed molecular species in the case of resorcinol. Chemical shifts relating to carbonate carbon from $MgCO_3$ is also observed indicating the interaction between MgO and CO_2 or DMC directly.

XPS results reflect the changes on the catalyst surface due to reaction through changes in binding energy and surface atomic composition. O 1s core level from spent catalysts observed at around 531 eV. The basic oxy anions O^{2-} on the surface are having electronic interaction with the DHB protons and hence a shift in the binding energy of O 1s core level from 530.2 eV (for fresh sample) is observed. Resorcinol having most acidic proton that interacts very strongly and hence a large shift in O 1s binding energy is observed. Increasing O 1s binding energy from 530.2 eV indicates the basicity of the surface decreases during methylation and the extent is large in the case of resorcinol. Hence the descending basicity led to the deactivation with TOS during resorcinol methylation.

Decreasing Mg 2p spectral intensity from spent catalyst indicates the surface Mg^{2+} species got buried under the deposited carbon species from reactants, products and polyaromatics residues. No Mg 2p core level emission observed in the case of resorcinol (DMC:Resorcinol = 2) reveals the deposition of heavy polyaromatics species and/or coke sediments on the surface and hence a burial of Mg into the subsurface or bulk. Absence of surface Mg concentration after transient state led to catalyst deactivation as evident from activity studies. Mg 2p from spent samples appeared at lower binding energy than fresh sample with a difference of 0.9 eV. It is likely that a dissociative adsorption of DHB as hydroxy phenolate anion and proton on the catalyst surface and the former makes the Mg sites electron rich. Another possibility is a partial loss in kinetic energy of photoemitted electron from Mg since it is buried in the subsurface.

K 2p observed at lower binding energy than K 2p of fresh sample is reflected also in the $L_3M_{45}M_{45}$ Auger transition, which appears at higher kinetic energy. This shift in the binding and kinetic energies is likely due to an interaction of hydroxy phenolate anion with K^+ ions. Sharp and intense C 1s spectral features reflect the presence of large amount of carbon on the spent catalyst surface.

The decrease in surface concentration of Mg, as evident from the surface atomic composition results, indicates the strong chemisorption of reactants and/or products or carbon deposits due to reaction. Very low surface Mg on resorcinol reaction catalyst is due to an increase in the carbon content, whereas with excess DMC in the feed carbon deposition is found to be less. This is due to the fact that excess DMC in the feed hinders the effective intermolecular interaction of resorcinol molecules that avoids condensation and comparatively low carbon content. Large K content on spent catalysts surface compared to fresh K-MgO indicating a large surface segregation of K due to reaction at above 583 K.

7.4 Conclusions

High amount of carbon deposits as evident from thermal analysis data throws light on the reasons for the catalyst deactivation. XRD and surface area measurements indicate the destructive reaction condition that affects the crystallinity of the catalyst samples due to carbon deposition and particularly on MgO and Cs-MgO. ^{13}C NMR reveals the presence of heavier polyaromatics and surface carbonates on spent catalysts. The surface basicity decreases during DHB interaction as evident from XPS studies and the large extent of basicity loss led to faster deactivation in the case of resorcinol methylation.

7.5 References

1. G. Ertl, H. Knozinger, J. Weitkamp, Handbook of Heterogeneous Catalysis, Vol 2, Wileyv VCH, Weinheim, 1997, p. 626.
2. X. Zhu, X. Li, M. Jia, G. Liu, W. Zhang, D. Jiang, Appl. Catal. A: Gen. 282 (2005) 155.
3. Z. Fu, Y. Y. D. Yin, Y. Xu, H. Liu, H. Liao, Q. Xu, F. Tan, J. Wang, J. Mol. Catal. A: Chem. 232 (2005) 69.
4. The Aldrich Library of ^{13}C and ^{1}H FT-NMR Spectra, 1st Edn, Vol. 2, 1993.
5. H. W. Papenguth, R. J. Kirkpatrick, B. Montez, P. A. Sandberg, Amer. Mineralogist, 74 (1989) 1152.
6. C. S. Gopinath, S. Subramanian, M. Paranthaman, A. M. Herman, Phys. Rev. B 48 (1993) 15999.
7. C. S. Gopinath, S. Subramanian, P. S. Prabhu, M. S. R. Rao, G. V. S. Rao, Physica C, 218 (1993) 117.
8. V. L.J. Joly, P. A. Joy, S. K. Date, C. S. Gopinath, Phys. Rev. B 65 (2002) 184416.
9. M. Muhler, R. Shlogl, G. Ertl, J. Catal. 138 (1992) 413.
10. Miyakoshi, A. Ueno, M. Ichikawa, Appl. Catal. A: Gen. 219 (2001) 249.

Chapter 8: Summary and conclusions

This chapter briefly summarizes the present thesis work and describes the conclusions and possible implications drawn based on the work.

Chapter 1 presents a general introduction to alkylation and heteroatom alkylation of aromatic compounds through environmentally benign heterogeneous catalytic route. The importance of aniline N-methylation and dihydroxybenzene (DHB) O-methylation were discussed. Catalysts attempted until now for these N- and O-methylation were briefly given from the literature survey. The use of metal oxides (alkali, alkaline and transition metal oxides), mixed metal oxides, and alkali metal ions promoted MgO as catalytic materials were highlighted. Introduction to spinel type materials especially ferrospinels and their catalytic applications were also given. The catalytic properties of metal oxides and the need to derive the structure-activity relationship using various physicochemical and spectroscopic characterization methods were highlighted. Finally the objectives of the present thesis work and thesis outline were given.

Chapter 2 describes the experimental procedures involved in the synthesis of catalytic materials. Cu,Zn-ferrospinel ($Cu_{1-x}Zn_xFe_2O_4$), aniline N-methylation catalyst was prepared by coprecipitation technique; whereas alkali metal ions loaded MgO for DHB O-methylation catalyst was prepared by incipient wet impregnation method using commercial MgO. Theory and experimental procedures involved in various physicochemical and spectroscopic characterization techniques such as, XRD, SEM, Surface area, FTIR, temperature programmed studies, TG-DTA, XPS and ^{13}C NMR were discussed.

XRD confirmed the formation of spinel, $Cu_{1-x}Zn_xFe_2O_4$ from the as synthesized samples after calcination at 773 K. The metal ions distribution in tetrahedral and octahedral environment is evident from the metal-oxygen bond stretching vibration observed in DRIFTS. Surface area measurements including BET adsorption-desorption results show they are nonporous materials; however, a small amount of mesoporosity is observed as evident from the type IV isotherm. Lewis acidity dominance on the surface of these ferrospinel catalysts is evident from the temperature dependent pyridine adsorption FTIR studies. Further, NH_3 TPD studies revealed the strength of Lewis acidic sites found by pyridine FTIR are weak to moderate in nature.

XRD of DHB O-methylation catalysts shows the MgO periclase phase remains unaffected with alkali metal ions loading. An increase in the crystallite size observed for alkali metal ions loaded MgO was due to MgO particles fusion during impregnation process. A decrease in surface area for promoted MgO is due to the alkali metal oxides dissolution on the surface of the MgO. This is well reflected in the N_2 adsorption-desorption isotherm as the alkali metal oxides filled the pores that lead to a decrease in the micropore volume compared to pure MgO. The fine particle size of pure and promoted MgO ranging between 50-100 nm is evident from the scanning electron micrographs.

Chapter 3 presents vapor phase experimental procedure and the systematic studies on vapor phase selective mono N-methylation of aniline to N-methylaniline. Cu^{2+} containing ferrites are found to be the potential catalysts. Further studies on Cu-Zn mixed ferrite exhibit a stable activity for longer period. Aniline methylation on $Cu_{1-x}Zn_xFe_2O_4$ over a wide range of temperatures and catalyst composition with methanol to aniline molar ratio of 3 was tested. Although all the catalyst compositions produce NMA selectively at 573 K, only $x = 0.5$ shows maximum aniline conversion under optimum reaction conditions. All of the Cu-containing compositions show high initial activity; however, the same decreases with increasing time on stream, except on $x = 0.5$. $ZnFe_2O_4$ shows hardly any catalytic activity hinting the direct role of Zn and Fe is negligible and Cu^{2+} seems to be the active species for aniline methylation. Detailed catalytic activity studies show that Cu^{2+} is largely responsible for methylation and Zn^{2+} enhances the stability of the system.

Further, the potential catalyst $Cu_{0.5}Zn_{0.5}Fe_2O_4$ was employed for N-monomethylation of substituted anilines (*o*-, *m*- and *p*-toluidines, 2,6-xylidine, p-anisidine and p-aminoacetophenone) at optimum reaction conditions that were adopted for aniline methylation. Temperature dependent studies show that maximum conversion was obtained at 573 K and the same decreases above and below 573 K due to different reasons. Selectivity for mono-N-methylated products remains more than 95%, which decreases with increasing temperature. Only traces of N, N-dimethylated and C-methylated products were observed. Electronic effects due to ring substituents do not play a significant role in the reactivity of the aniline substrates. However, steric factor plays a significant role and the same is clear from the results of o-toluidine and 2,6-xylidine.

Chapter 4 describes the importance of *in situ* studies, mainly FTIR spectroscopy, in the field of catalysis. Temperature dependent *in situ* FTIR study on adsorbed reactants and possible products of aniline N-methylation on $Cu_{1-x}Zn_xFe_2O_4$ were described. Adsorption of methanol alone on $Cu_{1-x}Zn_xFe_2O_4$ indicates a dissociative chemisorption of methanol. At high temperature it leads to systematic oxidation through formaldehyde, dioxymethylene and formate species to reformate (CO, CO_2, H_2) products. However, in the presence of aniline with methanol, the former dominates the surface and dictates the course of the methylation reaction to a large extent.

Aniline adsorbed molecularly on $Cu_{1-x}Zn_xFe_2O_4$ through N-atom on the acid-base pair site. However, aniline chemisorbed very strongly after N-H bond scission above 373 K with phenyl ring perpendicular to the plane of the catalyst surface. Phenyl ring of aniline and NMA also interacts in a very similar manner and the out of plane C-H bending vibrations are observed supporting this point. It is found that methylation of aniline is initiated by the protonation of methanol with the aid of a Lewis acid-base pair. The protonation of methanol occurs on the oxides by accepting protons released from the adsorbed aniline and to form the

N-methylated products. Thus the active center for the methylation is an acid-base pair site. It was also found that NMA formation from the reaction mixture at 473 K on the catalyst surface and its desorption above 473 K indicates a desorption limited kinetics. Stable methyl species was observed only on $ZnFe_2O_4$ above 473 K hints that, in general, Zn might be acting as methyl species source towards methylation. High catalytic activity observed on x = 0.5 is apparently due to well-separated Cu^{2+} sites by Zn and hints Zn acts as a spacer as well as source for methyl species.

Chapter 5 presents the results and discussion mainly from the photoemission studies on $Cu_{1-x}Zn_xFe_2O_4$ to address the changes in activity with catalyst composition and a structure-activity correlation. XRD from fresh and spent samples and TPR results from fresh samples were also given as supporting evidence. A significant reduction of Cu^{2+} to Cu was observed on spent catalysts for $x \leq 0.25$. The above total reduction was fully suppressed on spent catalysts with x = 0.5 and 0.75; however, a partial reduction of Cu^{2+} to Cu^{+} and Fe^{3+} to Fe^{2+} observed to occur. The valence band showed a significant change in BE of 3d bands of Cu and Fe on spent catalysts. Redistribution of cations on the spinel surface during reaction conditions is also evident from the surface composition analysis. Above redistribution of metal ions on the surface determines the course of the reaction as well as the stability of the catalysts. Presence of an almost equal amount of Cu and Zn on the surface is necessary for a longer TOS methylation activity on these spinel systems, in which Cu^{2+} is the active species for methylation and Zn^{2+} acts as an “active” spacer as well as stabilizer to decrease the extent of Cu^{2+} reduction and Cu agglomeration on the surface. It is the complete heterogeneity of the surface metal ions composition that helps for the stable catalytic activity and retention of the structural integrity of the catalyst. It is to be mentioned here that the highly heterogeneous distribution of all the metal ions on x = 0.5 composition prevents the Cu agglomeration. Indeed, Cu-ZnO, and $Cu-ZnO-Al_2O_3$ catalysts are known to be stable for very long period for reactions like atmospheric pressure methanol synthesis. Cu agglomeration was identified as a main deactivating step. It might be possible that such a heterogeneous distribution could be a reaction for high stability, which can prevent Cu agglomeration. Further, complete reduction to Cu metal takes place above 573 K on x = 0.5 composition reiterates the robustness of Cu against reduction in such a heterogeneous environments. This factor may be utilized effectively for reactions that occur below 573 K on Cu,Zn based catalysts.

Chapter 6 presents a comprehensive study on O-methylation of DHB with dimethylcarbonate (DMC), was carried out on MgO and alkali metal ions (Li, K and Cs) loaded MgO at vapor phase conditions. Pure MgO shows high O-methylation activity; however, that declines rapidly with time on stream (TOS). Alkali metal ions loaded MgO show better activity than pure MgO for all of the DHB substrates. Selectivity for O-methylated products increases with increasing basicity of alkali metals. Thus Cs promoted MgO (Cs-MgO) shows maximum O-methylation selectivity. Among the catalyst systems screened, K-MgO shows the best mono O-methylation activity with relatively high stability. Reactivity and products selectivity were influenced by substrates acidity and their mode of interaction on the catalysts surface. Catechol interacts through 1,2 hydroxyl groups on the catalysts surface gives more secondary products like PCC and veratrole; however, possible indications are available to further maximize 2-MP selectivity by varying reaction conditions. Resorcinol and hydroquinone interactions leave one hydroxyl group free in the space and this free hydroxyl group facilitates the formation of polyaromatics (especially in the case of resorcinol), which blocks the active sites that lead to catalysts deactivation with TOS. Low temperature (< 610K) employed leads to high selectivity for methoxyphenols compared to high dimethoxybenzenes selectivity observed in the literature reports.

A comparison of reaction results of all the three DHB, in general, suggests a systematic decrease in secondary products formation when two OH groups are as far as in hydroquinone. This helps in achieving high selectivity of 4-MP even under adverse condition such as high contact times. When the OH groups are closer, as the case in catechol, the secondary products formation seems inevitable. In the intermediate case of resorcinol both the above trend is observed depending on the reaction conditions.

Chapter 7 deals with detailed characterization studies on alkali metal ions loaded MgO before and after DHB methylation. Large amount of carbonaceous deposits observed on spent catalysts (particularly in the case of resorcinol), as evident from the thermal analysis indicates the catalyst deactivation due to coke deposition. Employing more DMC during resorcinol leads to better reactivity and the same reflects in the high K-content on the surface of spent catalysts through XPS analysis. Similar changes were observed on other systems also. ^{13}C NMR and thermal analysis revealed the presence of heavier polyaromatics and surface carbonates on spent catalysts apart from molecular reactants/products. The surface basicity decreases during DHB interaction as evident from the XPS studies and the large extent of basicity loss led to faster deactivation in the case of resorcinol methylation. Potassium ions promoted MgO stabilizes the crystallinity to a large extent than any other alkali metal ions, in spite of the harsh reaction conditions, could be a main reason for the high and stable activity associated with K-MgO.

List of publications

1. **M. Vijayaraj** and C.S. Gopinath, *Spectroscopic witness from reactants to product: FTIR studies on selective mono-N-methylation of aniline on* $Cu_{1-x}Zn_xFe_2O_4$, Journal of Catalysis *–Research Note* 226 (2004) 230.
2. T.Mathew, **M. Vijayaraj**, S.Pai, B.B.Tope, S.G.Hegde, B.S.Rao and C.S. Gopinath, *A mechanistic approach to phenol methylation on* $Cu_{1-x}Co_xFe_2O_4$*: FTIR study,* Journal of Catalysis 227 (2004*)* 175.
3. T.Mathew, S.Shylesh, B.M.Devassy, **M. Vijayaraj**, C.V.V.Satyanarayana, B.S.Rao and C.S. Gopinath, *Selective production of orthoalkyl phenols on* $Cu_{0.5}Co_{0.5}Fe_2O_4$*: A study on catalysis and characterization aspects*, Applied Catalysis A - General 273 (2004) 35.
4. S. Velu, K. Suzuki, **M. Vijayaraj**, S. Barman and C.S. Gopinath, *In situ XPS investigations of* $Cu_{1-x}Ni_xZnAl$ *mixed metal oxide catalysts used in the oxidative steam reforming of bio-ethanol,* Applied Catalysis B – Environmental 55 (2005) 287.
5. **M. Vijayaraj**, B. Murugan, S. Umbarkar, S.G. Hegde and C.S. Gopinath, *An insight into the mechanism of selective mono-N-methylation of aniline on* $Cu_{1-x}Zn_xFe_2O_4$*: A DRIFTS Study,* Journal of Molecular Catalysis A - Chemical 231 (2005) 169.
6. **M. Vijayaraj**, C. S. Gopinath, *On the "active spacer and stabilizer" role of Zn in* $Cu_{1-x}Zn_xFe_2O_4$ *towards selective N-methylaniline from aniline: XPS and catalysis study,* Journal of Catalysis, 241 (2006) 83.
7. **M. Vijayaraj**, C. S. Gopinath, *Selective production of methoxyphenols from dihydroxybenzenes on alkali metal ions promoted MgO,* Journal Catalysis (Submitted) 2006.

-------------xxxxxxxxxx-------------xxxxxxxxx-------------